Muons in the CRESST Dark Matter Experiment

Dissertation

der Mathematisch-Naturwissenschaftlichen Fakultät
der Eberhard Karls Universität Tübingen
zur Erlangung des Grades eines
Doktors der Naturwissenschaften
(Dr. rer. nat.)

vorgelegt von
Klemens Rottler
aus Geisenfeld

Tübingen
2014

Tag der mündlichen Qualifikation:	28.04.2014
Dekan:	Prof. Dr. Wolfgang Rosenstiel
1. Berichterstatter:	Prof. Dr. Josef Jochum
2. Berichterstatter:	Prof. Dr. Peter Grabmayr

Contents

Abstract

The search for Dark Matter has been one of the hottest areas in astroparticle physics for years, all the more since also the Large Hadron Collider started to test theoretical models for dark matter. WIMPs (Weakly Interacting Massive Particles) are the most prominent candidates for cold dark matter particles, mostly in combination with supersymmetric extensions of the Standard Model of particle physics. In experiments to directly detect WIMPs the main problem is, that the rate of WIMPs scattering on nuclei in the detector is expected to be very small with just a few signals per kg and year. Therefore one of the most important issues in the setup and operation of an experiment is the identification, reduction and control of spurious background signals.

It was shown already [1–3] that the currently achievable sensitivity for an experiment is limited by muons and muon induced particles. For this reason, it is of particular importance to identify muons in the experiment. In underground laboratories the muon flux in experiments is greatly reduced compared to experimental sites at or near the Earth surface. Nevertheless, current low background experiments suffer even from the small muon fluxes in these laboratories of the order of $1\,\mathrm{m}^{-2}\,\mathrm{h}^{-1}$ or lower. It is therefore mandatory to understand the muon flux in the experiments and be able to actively veto signals which originate from muons.

This issue is the motivation for this work, which covers the topic for the CRESST II experiment. An active muon veto system surrounding the dark matter experiment has been installed and operated during several dark matter search runs. The recorded data is analyzed in several ways. First, the performance of the muon veto system is examined with respect to the long-term stability. In this part the focus is on the overall aspects of the data without regarding muon signals. Then, data selection cuts are developed with the aim to define the characteristics of muon signals. The resulting muon safe sample is analyzed and the plausibility of the resulting muon flux at the CRESST experiment is tested against previous selection methods and the expectation from cosmic rays. Finally, coincident signals between the muon signals and events in the detector modules of CRESST are investigated. With the selection of muons determined in this work, a clear and almost background free coincidence signal can be extracted from the data, while for a veto safe selection no coincidences between the muon candidates and the detector modules could be identified above the random coincident level. In this way backtesting of the muon selection is conducted, confirming the data cuts.

Zusammenfassung

Die Suche nach Dunkler Materie ist eines der aktuellsten Gebiete der Astro-Teilchenphysik, was insbesondere seit dem Beginn der Messungen am Large Hadron Collider noch verstärkt der Fall ist, da theoretische Modellannahmen experimentell aus einer rein teilchenphysikalischen Richtung überprüft werden können. Galaktische WIMPs (Weakly Interacting Massive Particles) stellen dabei die bedeutendsten Kandidaten dar, die meist mit supersymmetrischen Theorien verbunden sind. In Experimenten zum direkten Nachweis von WIMPs erweist sich als Problem, dass aufgrund des geringen Wechselwirkungsquerschnitts die erwartete Streurate von WIMPs an Kernen im Detektor mit nur wenigen Ereignissen pro kg und Jahr extrem niedrig erwartet wird. Hieraus lässt sich schon ableiten, dass eine der wichtigsten Aufgaben beim Aufbau und Betrieb eines Experiments die Identifizierung, Reduzierung und Kontrolle von störenden Untergrundereignissen ist.

In mehreren Arbeiten [1–3] wurde bereits gezeigt, dass die derzeit erreichbare Sensitivität insbesondere durch kosmische Myonen und myoneninduzierte Teilchen limitiert ist. Obwohl in Untergrundlaboren der Fluss kosmischer Myonen gegenüber der Erdoberfläche um etwa 10^6 reduziert ist, stellt auch ein typischer Fluss von $1\,\mathrm{m}^{-2}\,\mathrm{h}^{-1}$ oder weniger noch ein Problem für Experimente mit sehr niedrigen Ereignisraten dar. Aus diesem Grund ist es von großer Bedeutung, Myonen im Experiment zu identifizieren und koinzidente Signale in den Detektormodulen herauszufiltern.

Diese Aufgabenstellung ist die Motivation für diese Arbeit verbunden mit der Anwendung im CRESST-II Experiment. Ein aktives Myonvetosystem wurde in das bestehende Experiment integriert und während mehrerer Messperioden betrieben. Der Hauptteil der Arbeit befasst sich mit der Analyse der Daten dieses Vetosystems des CRESST-II Experiments, wobei zuerst auf verschiedene Faktoren eingegangen wird, die den stabilen Betrieb dieses Vetosystems betreffen, und Parameter aufgezeigt werden, die der Kontrolle und Diagnose dienen. Danach wird das Hauptaugenmerk auf die sichere Identifizierung von Myonen im Vetosystem gelegt, verbunden mit der Bestimmung und Plausibilisierung der Ereignisraten im Vergleich zur Erwartung wie auch zu bisherigen Methoden. Abschließend werden der Einfluss der klar identifizierten Myonen auf die Detektormodule in CRESST analysiert und koinzidente Ereignisse untersucht. Mit den in dieser Arbeit sicher bestimmten Myonen konnte ein klares, fast untergrundfreies Koinzidenzsignal gefunden werden, im Gegensatz zu einer veto-sicheren Methode, mit der keine eindeutigen Koinzidenzen festgestellt wurden. Dadurch konnte die Auswahl an Myonen auch im Rückvergleich verifiziert werden.

1

The case for Dark Matter

In this chapter, a short overview of the early Universe and the cosmology will be given, which is needed to understand the motivation of our experimental observations.

After that, the Concordance Model (ΛCDM) will be shortly discussed in more detail as from there the theoretical need for dark matter arises. Then, having this background, the experimental evidence and indications for the actual existence of Dark Energy and Dark Matter will be presented, focusing on the latter. Concluding this chapter will be an overview of currently running direct and indirect search experiments, considering also relevant former and upcoming experiments.

1.1 Cosmology

Since the currently most favored dark matter candidates are believed to be non-relativistic heavy particles created early in the history of the Universe, it is necessary to give an explanation of their origin. This in turn necessitates a short overview of the cosmology of our Universe in its early stages.

As Kolb & Turner [4] nicely start their book, the currently accepted understanding of the Universe relies on the Friedman-Lemaître-Robertson-Walker cosmological model (FLRW cosmology), where the Universe evolved from a so-called hot big bang. The assumptions are relatively basic: homogeneity and isotropy in space, also known as the cosmological principle, which states that there is no preferred position in the Universe at any point and by any observer at any time, if viewed on a sufficiently large scale. This leads to a rather simple metric, the Friedman-Lemaître-Robertson-Walker (FLRW) metric[1]

$$ds^2 = dt^2 - R^2(t)\left(\frac{dr^2}{1-kr^2} + r^2 d\theta^2 + r^2 \sin^2\theta d\phi^2\right) \tag{1.1}$$

in comoving coordinates, which simplifies Einstein's General Relativity field equations with the cosmic scale factor $R(t)$. The constant k determines the Universe's curvature. Einstein's equations, which also contain the famous cosmological constant Λ, are as in [4]

$$R_{\mu\nu} - \frac{1}{2}\mathcal{R}g_{\mu\nu} \equiv G_{\mu\nu} = 8\pi G T_{\mu\nu} + \Lambda g_{\mu\nu} \tag{1.2}$$

with the Ricci scalar $\mathcal{R}$, the Einstein tensor $G_{\mu\nu}$ and $T_{\mu\nu}$ as the total stress-energy or energy-momentum tensor. Solving these equations explicitely describes the time dependence of the scale factor $R(t)$ and therefore the dynamics of the Universe. $T_{\mu\nu}$ must be diagonal to fulfill the symmetries set by the metric, and assuming isotropy in space requires the spatial components to be equal. The energy density $\rho(t)$ and pressure $p(t)$ can be described by a perfect fluid, for which the tensor $T_{\mu\nu}$ is

$$T_{\mu\nu} = \mathrm{diag}(\rho, -\mathbf{p}) = \mathrm{diag}(\rho, -p, -p, -p). \tag{1.3}$$

[1] also often called FRW or RW metric.

As ρ is a density, we easily can come to some important observations by using energy-momentum conservation $\Delta_\mu T^{\mu\nu} = 0$, which leads to the first law of thermodynamics

$$d(\rho R^3) = -p d(R^3). \tag{1.4}$$

If one assumes a simple equation of state,

$$w = \frac{p}{\rho}, \tag{1.5}$$

with the dimensionless and time-independent proportionality constant w, the energy density ρ behaves as

$$\rho \propto R^{-3(1+w)}, \tag{1.6}$$

which leads to several interesting examples:

$$p = \frac{1}{3}\rho \quad \longrightarrow \quad \rho \propto R^{-4} \qquad \text{radiation} \tag{1.7a}$$

$$p = 0 \quad \longrightarrow \quad \rho \propto R^{-3} \qquad \text{matter} \tag{1.7b}$$

$$p = -\rho \quad \longrightarrow \quad \rho \propto \text{constant} \qquad \text{vacuum energy} \tag{1.7c}$$

From the Einstein equations (eq. 1.2), the dynamics of the evolution of the scale factor R follow. The equation for the speed

$$\frac{\dot{R}^2}{R^2} + \frac{k}{R^2} = \frac{8\pi G}{3}\rho \tag{1.8}$$

originates from the $\mu = \nu = 0$ component and is the so-called first Friedman equation. The equations for the acceleration

$$2\frac{\ddot{R}}{R} + \frac{\dot{r}^2}{R^2} + \frac{k}{R^2} = -8\pi G\rho, \tag{1.9}$$

result from the $\mu = i, \nu = i$ components of the Einstein equation. Subtraction of these two equations eliminates the speed $\dot{R}$ and provides an equation for the accelation parameter $\ddot{R}$, the second Friedman equation

$$\frac{\ddot{R}}{R} = -\frac{4\pi G}{3}(\rho + 3p) \tag{1.10}$$

Some remarks about these equations are in order. Since $R > 0$, it follows that for $(\rho + 3p) > 0$ the acceleration $\ddot{R}$ is always negative. In this case, there is a singularity in the limit $R = 0$, which is associated with the Big Bang and defines the time zero. Usually the Hubble parameter

$$H \equiv \frac{\dot{R}}{R} \tag{1.11}$$

is introduced at this point. It is a time-dependent parameter, which incorporates the expansion rate of the universe. H_0 commonly denominates the present value of the parameter and is called the *Hubble constant* and is expressed as $H_0 = 100h\,\mathrm{km\,s^{-1}Mpc^{-1}}$, using the dimensionless number $h \approx 0.7$ (see also table 1.2). By using the Hubble parameter and defining the normalized parameters

$$\rho_c \equiv \frac{3H^2}{8\pi G} \tag{1.12}$$

$$\Omega \equiv \frac{\rho}{\rho_c}, \tag{1.13}$$

where ρ_c is the critical density and Ω the density normalized to the critical density, we can rewrite the Friedman equations slightly different as

$$\frac{k}{H^2R^2} = \frac{\rho}{\frac{3H^2}{8\pi G}} - 1 = \Omega - 1. \tag{1.14}$$

Due to the fact that both H^2 and R^2 are non-negative, this equation contains some important implications for the geometry of the Universe. As listed also in table 1.1, the curvature k gives information about the future evolution of the Universe, which is open for $\Omega < 1$, i.e. an energy density less than the critical energy density ρ_c and $k = -1$, closed for $\Omega > 1$, corresponding to a positive curvature $k = 1$, or flat for $k = 0$ and an energy density equalling the critical density, $\Omega = \rho/\rho_c = 1$. It should be noted that these consequences are important now and in the future of the Universe, but have not been as dominant at early times, when the curvature term was negligible. With the described geometry the boundaries

k	Ω	Universe
$+1$	> 1	closed
0	$= 1$	flat
-1	< 1	open

Table 1.1: Geometry of the Universe.

for observations of the most natural idea of a flat Euclidean universe with $\Omega = 1$ are set. If experiments could show that all detected matter accounts for $\Omega = 1$, there is no need for new physics.

1.2 Energy content and Cosmic Microwave Background

In the last section it was mentioned that the standard model of particle physics (SM) would be sufficient if the condition $\Omega = 1$ can be fulfilled with the visible matter. Therefore two issues need to be answered: the parameter Ω needs to be determined, as well as the question how much matter we can actually detect. This section gives an overview of the current cosmological parameter values and an impression how they are attained. First, it should always be kept in mind, that H and therefore also ρ_c are not constants (see eq. 1.12, but constantly change as the Universe expands. At present the relative changes are small, but were important in the early stages of the Universe.

The sum of all contributions to the overall energy density in the Universe was and is a matter of a great number of experiments and calculations. Some of the most noticeable experiments and results in this field come from increasingly detailed observations of the Cosmic Microwave Background (CMB) radiation. The CMB blackbody radiation itself was predicted by several authors and discovered famously and accidentally by Penzias and Wilson in 1964/5 [5], when they could not identify the source of an irreducible isotropic background with a temperature of 2.7 K in their radio antenna receiver. The discovery was the major breakthrough for the acceptance of the cosmological Big Bang models. It gives insights to very early times in the evolution of the Universe, since the CMB in Big Bang cosmological models originates from the surface of last scattering, i.e. when photons and electrons cease to be in thermal equilibrium resulting in the recombination of atoms about 380 000 years after the Big Bang.

Later experiments determined that the CMB represents almost perfect black body radiation, as for example measured by the COBE satellite[2] in 1990. Soon afterwards detailed investigations of variations in the CMB were undertaken, and two experiments gained major success, the Wilkinson Microwave Anisotropy Probe (WMAP) and the Planck satellite mission. As the name of the former indicates, the focus was to measure anisotropies in the CMB, which give leads to the physics processes in the early cosmology.

Figure 1.1 shows the results from the CMB measurements from Planck, where the left panel displays the all-sky measurements of fluctuations in radiation after subtraction of the dipole, which results from the motion of the Earth relative to the CMB. With the increased sensitivity of the WMAP and Planck satellite missions temperature differences of the order of μK could be resolved (see fig. 1.1b), which indicate anisotropies originating either from the decoupling era or interactions of the CMB in the path to the observer. The all-sky picture in fig. 1.1a displays the residual temperature fluctuations at a scale of μK after

[2] Cosmic Background Explorer (COBE).

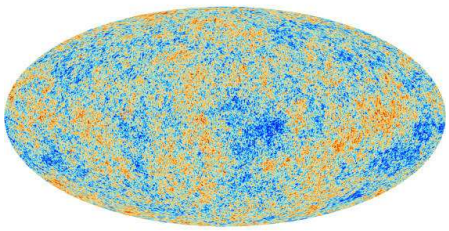

(a) The CMB full sky as observed by Planck. Pictured are the variations of the background radiation in different frequency bands after subtraction of the dominant dipole and foreground. The temperature differences indicated by the colors are on the order of μK. Image credit: ESA/NASA.

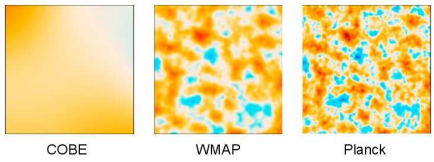

(b) Improvement in the $\Delta T/T$ resolution from COBE to WMAP and Planck. Edited picture, original credit: ESA/NASA.

Figure 1.1: Cosmic Microwave Background anisotropies.

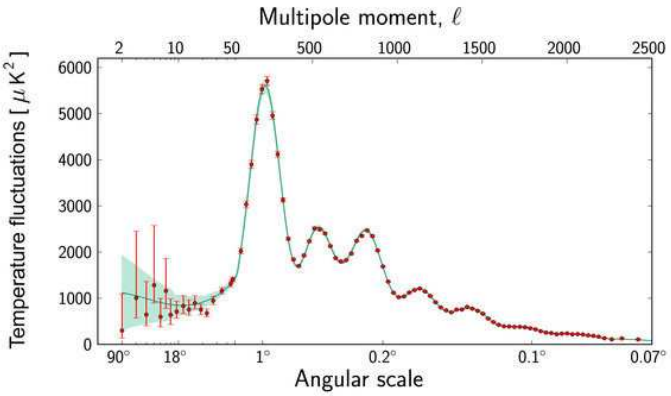

Figure 1.2: Power spectrum of the CMB. Image credit: ESA/NASA.

subtracting foreground. Planck achieves an angular resolution of up to about 1/12 degree, about 2.5 times better than WMAP.

Several important conclusions can be drawn from the peak structure of the power spectrum of the CMB radiation, because the peaks can be related to acoustic oscillations in the medium before the decoupling. Fig. 1.2 illustrates the measured multipole moment ℓ, which is the equivalent of the angular scale of variations, meaning that the lowest multipole peaks indicate the largest structures. The position of the first and most prominent peak indicates the curvature of the Universe, while the amplitudes of the second and third peak determine the baryon and dark matter density.

At least since the publication of the results of SN Ia redshift surveys confirming the expansion of the universe[3] [8,9], the Concordance Model (ΛCDM) is the generally accepted standard model of cosmology with the current cosmological parameters as listed in table 1.2, which still show some small tensions between the WMAP and the Planck results.

1.3 Thermal relics

Massive particles leave the thermal equilibrium in the expanding Universe and freeze out at a certain temperature T, therefore a density higher than the equilibrium density remains.

[3]The 2011 Nobel Prize in Physics was awarded to S. Perlmutter from the Supernova Cosmology Project, and B. Schmidt and A. Riess from the High-Z Supernova Search Team for "the discovery of the accelerating expansion of the Universe through observations of distant supernovae", quoting from the Nobel citation.

Contributions to the energy content in the Universe		
total	Ω	1.00 ± 0.02
Matter	$\Omega_M h^2$	0.1423 ± 0.0029
Dark Matter	$\Omega_{DM} h^2$	0.1196 ± 0.0031
Baryons	$\Omega_B h^2$	0.02207 ± 0.00033
Neutrinos (from [6])	Ω_ν	$0.0009 < \Omega_\nu < 0.048$
Dark Energy (Cosmological constant)	Ω_Λ	0.686 ± 0.020

Table 1.2: Energy content in the universe. The numbers are given as fractions of the critical density ρ_c and are the Planck 68% confidence limit results quoted from [7]. Note that the PDG parameter values [6] vary slightly. The present day Hubble parameter is $H_0 = (67.4 \pm 1.4)\,\mathrm{km\ s^{-1}Mpc^{-1}}$ and $h = \frac{H_0}{100 km/s/Mpc}$.

If the thermally averaged annihilation rate $\langle \sigma_{ann} v \rangle$ is high, then a smaller number density is expected to survive, and vice versa (fig. 1.3), resulting in a relic density of

$$\Omega_x h^2 = \frac{3 \cdot 10^{-27} cm^3/s}{\langle \sigma_{ann} v \rangle}, \tag{1.15}$$

for a particle species x. For dark matter with $\Omega_\chi h^2 \approx 0.12$ this leads to $\sigma \sim \alpha^2 / M_{EW}^2$, where M_{EW} is the electroweak mass scale, which presents a nice coincidence between particle physics and cosmology.

If a particle is relativistic at the time of its freeze-out, it is called a *hot* relic. The most prominent example of this kind is the neutrino, which also provides a relic cosmic neutrino background at a current day temperature of about 1.95 K. Other thermal relic particles can

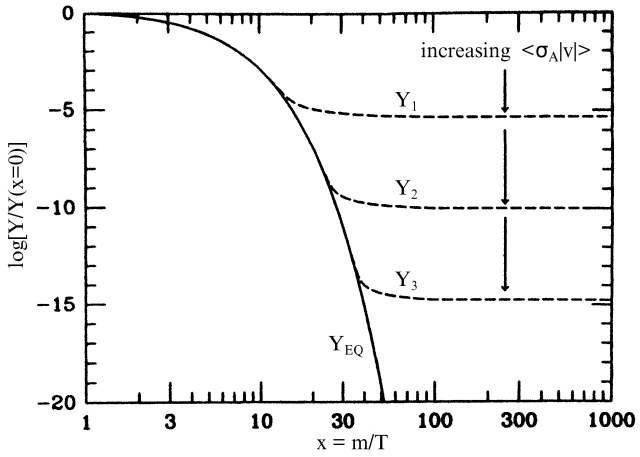

Figure 1.3: The freeze-out of massive particles. The continuous line corresponds to the thermal equilibrium number density Y_{EQ}, and the dashed lines are the actual abundances. With increasing annihilation cross section the remaining number density becomes smaller. Figure adapted from [4].

be the hypothetical supersymmetric partners of Standard Model particles, which provide a range of particles that have number densities and interaction strengths which are needed to fulfill the requirements for dark matter from cosmology. These particles have large rest masses of $\mathcal{O}(100)\,\mathrm{GeV}$, and therefore have a small momentum at their freeze-out, thus they are *cold* relic particles and can constitute cold dark matter.

1.4 Observational Evidence for Dark Matter

First indications for the existence of more than the visible matter in the universe –more precisely a higher energy density, which interacts gravitationally– were given by the observations of Oort (1932) and Zwicky (1933). Oort [10] observed stars moving around the galactic disk in the Milky Way, and concluded that the visible mass would not create a strong enough force to keep these stars on their trajectories. He concluded that the invisible mass is about more than the visible mass[4], and that it is 'more strongly concentrated to the galactic plane'.

Fritz Zwicky, on the other hand, looked outside our own galaxy, and observed the velocity distribution of nebulae in the Coma cluster [11,12], and determined their average mass. The result was much higher than the mass derived from the average luminosity of nebulae, requiring a luminosity-mass conversion factor[5] γ of about 500, which he compared to 3 for the close-by Kapteyn stellar system.

Although the hint, if not strong evidence, for matter in the galactic environment, which is not directly accessible with the standard astronomical tools of optical, infrared and radio telescopes, exists for about 80 years now, the interest began to increase again as late as the 1970s [13,14] with detailed studies of galactic rotation curve of the Andromeda Nebula. These observations deal with gravitational effects in or around visible systems at the scale of galaxies or galaxy clusters. Since Oort's and Zwicky's observations delivered a first clear impression that there may be more matter in the Universe than what can be seen in the optical spectrum, other hints and evidences of dark matter in different astrophysical environments and scales have been found. This section will give an overview of those indications. Although most of the dark matter is expected to be cold, a few remarks about hot dark matter are included here for completeness.

Hot and Warm Dark Matter

The concept of Hot and Warm Dark Matter is inferred from non-luminous matter, which contributes to the dark matter content, but consists of relativistic or non-virialized particles. As relativistic particles suppress structure formation on small scales, structure observations can produce limits on the amount of hot dark matter. Most prominently neutrinos belong into this category, as they were relativistic also at the time of their freeze-out from thermal equilibrium due to their tiny rest mass. Neutrinos are the only particle species, for which upper and lower boundaries on Ω_ν can be specified (see table 1.2).

From WMAP & Planck measurements combined with high multipole ℓ surveys the currently best limits on the sum of the neutrino masses can be deducted. The sum of the neutrino masses for all flavors is given by

$$\sum m_\nu = 0.66 \text{ eV} \qquad (95\%)$$

When including additional experimental and theoretical considerations such as lensing results and baryonic acoustic oscillations (BAO), this limit can be lowered to

$$\sum m_\nu = 0.23 \text{ eV} \qquad (95\%).$$

This value should be considered with caution however, as it depends on the Hubble parameter and Ω_Λ, which from CMB alone is highly model dependent [7].

Constraints on hot dark matter are also given by the CAST experiment, which partially closes the window of allowed parameters [15] of axion mass $m_a \approx 0.5...1.2\,\text{eV}$ and interaction strength $g_{a\gamma} \approx (2.5...4) \cdot 10^{-10}\,\text{GeV}^{-1}$. Cold dark matter axions would typically have a smaller mass in the meV or μeV range.

[4] Oort notes that the visible mass fraction could be increased significantly by taking into account five more magnitudes for the stars.

[5] Zwicky's denomination is used here.

Galactic Dark Matter

The "classical" cold dark matter, which is commonly cited in popular literature, is located in and around galaxies. It is also the only form of (cold) dark matter accessible for direct detection. Since it was discovered that spiral galaxies are rotating, there have been many measurements of rotation velocities. With increasing distance r from the galactic centers, the measured rotation velocities v in these axisymmetric system should drop according to Newton's law:

$$\frac{v^2}{r} = \frac{GM}{r^2}, \tag{1.16}$$

where M denotes the mass within the radius r. This leads to

$$v = \sqrt{\frac{GM}{r}} \propto 1/\sqrt{r} \tag{1.17}$$

However, measurements have shown repeatedly that even for very large galactic radii beyond the main region of visible stars the circular velocities of stars remain almost constant. If one considers only the matter from the visible stars with the mass-luminosity relation, then the integrated mass of the galaxy would not suffice to keep these distant stars on a trajectory around the galactic center. This indicates that there is an additional gravitational potential, which is usually associated with dark matter. Using equation 1.17, one can switch the argument and estimate the mass needed for the measured velocities at a given radius for a spherical symmetric system as

$$M = \frac{v^2 r}{G} \tag{1.18}$$

From observations of stars positioned off the galactic plane one can deduct that the dark

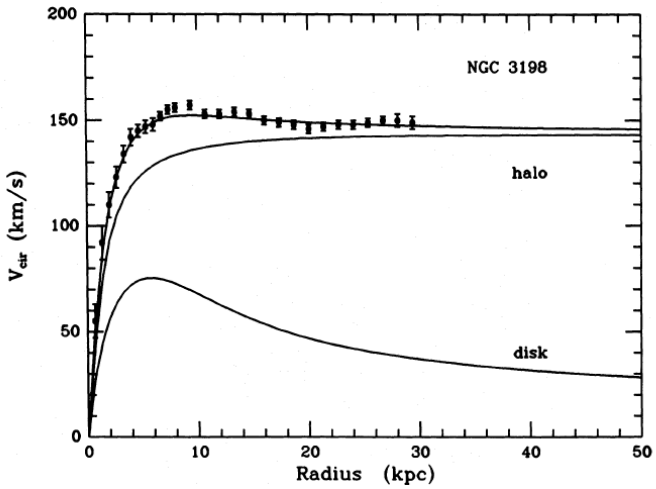

Figure 1.4: Galaxy rotation curve example: the rotational velocity v of stars in a galaxy rises initially with the concentration of most stars near the galactic center. With increasing distance the number of visible stars decreases, and according to Kepler's law v should drop with $\propto 1/\sqrt{r}$. However, the measured velocities remain almost constant, indicating a large unseen mass component. Picture taken from [16]. The solid lines indicate models for the galactic disk and the dark halo used to fit the rotation curve.

matter is not confined to the galactic disc, and a spherical distribution is more likely. There are several density profiles commonly used for modelling spiral galaxies and their dark haloes, with the most popular being the Navarro-Frenk-White (NFW) profile [17]

$$\rho(r) = \frac{\rho_0}{\frac{r}{r_s}(1+\frac{r}{r_s})^2} \tag{1.19}$$

which has been obtained by N-body simulations. The characteristic or scale radius r_s is related to a virial radius r_{200}, which requires that within this radius the mean overdensity

is $200\rho_c$, via a dimensionless concentration parameter c, $r_s = r_{200}/c$. This representation is simplified for the Milky Way, but in general covers a wide mass range of galaxies with similar profile shapes.

A short excursion is included at this point: averaged over the whole universe the energy density for $\Omega = 1$ and $\rho_c = \frac{3H^2}{8\pi G}$ is slightly less than $5\,\mathrm{keV/cm^3}$, of which about $1.1\,\mathrm{keV/cm^3}$ are due to dark matter. In the Milky Way, the dark matter energy density can be estimated from the movement of off-plane stars, and is around $0.3\,\mathrm{GeV/cm^3}$, or about 3 WIMPs per liter, assuming a WIMP mass of 100 GeV. Thus the energy content due to dark matter in our galaxy is more than five orders of magnitude larger than the average.

Dark Matter in Clusters of Galaxies

The "bullet cluster" at a distance of 3.7 billion light years was formed in a collision of two large clusters of galaxies. Its popular name derives from the pictures of hot X-ray emitting gas measurements of the Chandra telescope, which show a bullet-shaped gas cloud passing through the gas cloud of another cluster, heating up the surrounding matter in the process [18]. The mass distribution of the whole system, however, was inferred by optical

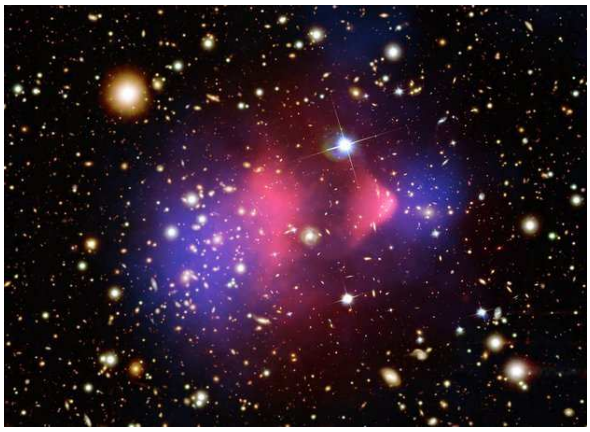

Figure 1.5: Composite image of the galaxy cluster 1E0657-56 (bullet cluster). In yellow/white the optical image from the Hubble Space Telescope is shown, in pink the x-ray picture taken by the Chandra X-Ray Observatory with an exposure of 500ks, and in blue color the distribution of the gravitational potential from microlensing. The x-ray picture shows the visible matter from colliding gas clouds in the interacting galaxies. Clearly the center of gravity from microlensing is shifted from the visible mass. Picture copyright: X-ray: NASA/CXC/CfA/M.Markevitch, Optical and lensing map: NASA/STScI, Magellan/U.Arizona/D.Clowe, Lensing map: ESO WFI.

observations by the Hubble Space Telescope together with the study of microlensing effects. Using these techniques, it could be shown that the main mass was not concentrated where the hot gas emits X-rays, but that mass centers have more separation than can be seen in the X-ray pictures, which means that non-visible matter moved faster through the collision than visible matter. This is the effect of slowdown (drag), which acts only on normal matter like the hot gas clouds, but does not affect dark matter.

Often this observation of the separation of matter distributions is regarded as the first proof for the existence of dark matter, which, due to the popular name, is often also referred to as "smoking gun". Popular alternative theories like Milgrom's Modified Newtonian Dynamics (MOND) theory [19] do not predict such effects [18, 20]. There exist many more theoretical models and suggested particles. Listing all of them is beyond the scope of this chapter, but the reader is invited to several publications which treat the topic in more detail, e.g. [6, 21–25].

1.5 Dark Matter Particle Candidates

Up to now the nature of dark matter was not discussed, but only the required energy densities averaged e.g. on the scale of galaxies were given. Thus it could be feasible that heavy compact objects consisting of ordinary matter, such as brown dwarfs or MACHOs (Massive Compact Halo Objects), in general objects which do not produce enough electromagnetic emissions, could also be considered as Dark Matter candidates. For several years MACHOs were considered as an important ingredient to the solution of the Dark Matter problem, but dedicated searches did not find enough such objects. Due to the fact that such objects could not account for the missing mass by themselves, they are not discussed here in detail.

Particle dark matter is the logical continuation of cosmology, and there are many theories which predict particles which can be suitable for dark matter. In particular, supersymmetric theories would be an interesting extension of the standard model, adding a superpartner to each existing standard model particle with 'mirrored' properties.

Supersymmetric dark matter

Supersymmetric (SUSY) extensions to the Standard Model of particle physics (SM) introduce a symmetry between fermions and bosons. Fermions acquire as superpartners the sfermions with spin 0, while bosons add spin-$\frac{1}{2}$ or $\frac{3}{2}$ superpartners, e.g. the photino and the gravitino, respectively. In an unbroken supersymmetry the (super)partners would have the same mass. From particle physics experiments this symmetry is obviously broken, as the lowest present bounds on the mass of superparticles are in the region of 100 GeV.

However, there are models to spontaneously break supersymmetry and create this mass imbalance. The Minimal Supersymmetric Standard Model (MSSM)[6] introduces the so-called R-parity

$$R = (-1)^{(3B+L+2s)},$$

where B is the baryon number, L the lepton number and s the spin, which is required to explain the stability of the proton. Standard model particles in this framework have R-parity 1, while their supersymmetric partners have $R = -1$. Assuming that R-parity is conserved, the lightest supersymmetric particle (LSP) is stable. This particle then is an at most weakly interacting massive particle with a mass $\mathcal{O}(100)$GeV and therefore a natural candidate for particle dark matter.

According to SUSY theories, a likely candidate for the LSP is a superposition of the spin-$\frac{1}{2}$ superparticles of the exchange bosons, which are electrically neutral. The resulting state is commonly called the *neutralino* χ or χ_1^0

$$\chi = N_1\tilde{\gamma} + N_2\tilde{Z}^0 + N_3\tilde{H}_1^0 + N_4\tilde{H}_2^0, \tag{1.20}$$

which is the superposition of photino $\tilde{\gamma}$, zino $\tilde{Z}^0$ and the Higgsinos $\tilde{H}_1^0$, $\tilde{H}_2^0$, the superpartners of photon, Z^0 and the neutral scalar Higgs particles, respectively [26]. The coefficients N_i are normalized to unity: $\sum_{i=1}^{4} |N_i|^2 = 1$, but the composition is unknown and depends on the SUSY model. Neutralinos with a larger N_1 and N_2 contributions are called gaugino-type, which usually arise in low-mass models, while a larger N_3 and N_4 corresponds to higgsino-type particles, creating heavier neutralinos. If the neutralino is a mixed gaugino/higgsino state, it is expected to have a significant scalar coupling [21].

Constraining the parameter space to cosmologically interesting models, which can provide $\Omega_m \approx 0.27$, the neutralino should not be heavier than about a few TeV. In the case that the gravitino $\tilde{g}$ would constitute the LSP, the interaction occurs only via gravitation, and not at the weak scale. In these scenarios it is almost impossible to detect the LSP in the forseeable future.

Axions

Axions represent a class of non-thermal dark matter particles. They result from the strong CP problem and are hypothetical light bosons, but nevertheless produced with a low mo-

[6] SUSY generally has about 120 degrees of freedom mainly due to the large number of helicity states for quarks. In MSSM models this number can be reduced to as little as five free parameters.

mentum. Therefore they can be categorized as a cold dark matter component depending on the axion mass. In the mass range between about 10^{-6} and 10^{-3} eV, the axion could contribute a large part to Ω_M [26].

Solar axions are typically not considered as cold dark matter, but the proof of their existence via a detection would be interesting nevertheless. The sun is the strongest and closest source of axions, where they are produced by the Primakoff effect via scattering photons in the strong electromagnetic field of a nucleus Ze.

$$\gamma + Ze \leftrightarrow Ze + A \tag{1.21}$$

There are astrophysical limits on the creation of axions in stars, which result from the fuel burning cycles, as axions would constitute a way of energy loss from a star [27].

1.6 Direct searches – detection method and experiment types

Most direct dark matter searches try to detect recoil signals created by WIMPs scattering on the nuclei of the detector target material. The signature of WIMPs created by such processes is discussed here, followed by a list of different experiments

1.6.1 Expected detection rates and energy spectra

In a detector, the total interaction rate R per unit mass can be described as [28]

$$R = \frac{N_0}{A}\Phi\sigma(v). \tag{1.22}$$

Here $\Phi = nv = \frac{\rho_\chi}{m_\chi}v$ is the flux of WIMPs χ, which is determined by the particle's mass m_χ and mass density ρ_χ as well as the WIMP velocity v with respect to the target nucleus, and σ is the WIMP-nucleon cross section. Cold dark matter particles are expected to have a velocity distribution mainly below the galactic escape velocity[7] of about 650 km/s and a maximum around 220-250 km/s. This justifies that all scattering processes are handled in the non-relativistic limit.

The recoil energy deposited by a WIMP of mass m_χ on a nucleus N with mass m_N is given kinematically by

$$E_{rec} = \frac{m_\chi^2 m_N}{(m_\chi + m_N)^2}v^2(1 - \cos\Theta), \tag{1.23}$$

which can be rewritten with the reduced mass of the WIMP-nucleus system, $\mu_{\chi N} = \frac{m_\chi m_N}{m_\chi + m_N}$, to

$$E_{rec} = \frac{\mu_{\chi N}^2}{m_N}v^2(1 - \cos\Theta) \tag{1.24}$$

With the reduced mass it becomes obvious that the maximum recoil energy can be achieved if the target nucleus and the WIMP have the same mass, so $\mu_{\chi N} = m_\chi/2 = m_N/2$, and the WIMP's full momentum is transferred to the nucleus for $\Theta = \pi$. Using these assumptions, one can estimate the expected maximum recoil energies approximated with $v = v_\chi \approx 10^{-3}c$

$$E_{rec} = \frac{1}{2}\frac{\mu_{\chi N}^2}{m_N}v^2 \approx \frac{1}{2}\cdot 10^{-6} m_\chi = 50\left(\frac{m_\chi}{100\ \mathrm{GeV}}\right)\mathrm{keV} \tag{1.25}$$

This number for a typical expected WIMP mass illustrates the challenges for direct dark matter detection, as at most recoil energies of $\mathcal{O}(10)\,\mathrm{keV}$ are expected. For example, a WIMP with a mass of 100 GeV scattering on tungsten with $M_N \approx 184\,\mathrm{GeV}$, which is used in the CRESST experiment, creates a maximum recoil energy of about 38 keV.

[7] New measurements suggest that this value might be too high and the escape velocity be at (550 ± 100) km/s, maybe below 600 km/s. While this affects the largest possible recoil energies and is a substantial uncertainty, only the tail of the velocity distribution and therefore a small fraction of the WIMPs is concerned.

In practical units, used to get an impression what can be expected in an experiment the total signal rate in a detector can finally expressed by [28]

$$R_0 = 0.054 \left[\frac{100}{A}\right] \left[\frac{\rho_\chi}{0.4\,\mathrm{GeV\ cm^{-3}}}\right] \left[\frac{v_0}{230\,\mathrm{km/s}}\right] \left[\frac{100\,\mathrm{GeV}}{M_\chi}\right] \left[\frac{\sigma_0}{pb}\right] \mathrm{kg^{-1}d^{-1}} \tag{1.26}$$

neglecting the finite escape velocity. The dark matter density applied here still has a relatively large range of allowed values and can easily vary by a factor of two. Under these simplifications a realistic WIMP-nucleus scattering rate in a given detector can be extracted from eq.1.26, and an estimate can be given to which degree background must be suppressed. A typical WIMP with a mass of 50 GeV would thus produce on average one recoil signal per day over the whole spectrum in 20 kg of tungsten target material for a WIMP-nucleus cross section of one picobarn.

Recoil energy spectrum

In general not only the total expected count rate of WIMPs on the target as in eq. 1.26 is important, but especially the differential energy spectrum of the recoiling nuclei, which is expected to be a featureless exponential distribution in the simplest case [28]

$$\frac{dR}{dE_{rec}} = \frac{R_0}{rE_0} e^{-E_{rec}/rE_0}, \tag{1.27}$$

where

$$r = \frac{4m_\chi m_N}{(m_\chi + m_N)^2} = 4\frac{\mu}{m_\chi m_N}$$

is introduced as a convenient dimensionless kinematic factor. E_{rec} and E_0 are the recoil energy and the most probable incident energy of the WIMP with mass m_χ.

In reality the differential spectrum is more complicated, as several factors play a role: the WIMP velocity distribution, the relative velocity of the Earth within the solar system and the galaxy, the nuclear structure (form factor) of the target material, possible spin-dependent interaction, and also issues like detector efficiencies and thresholds need to be taken into account.

Following the steps in [28] the total event rate of eq. 1.22 is used again, and the velocity dependent factors have to be calculated. The basic event rate per unit mass is

$$dR = \frac{N_0}{A}\sigma v dn, \tag{1.28}$$

where $N_0 = 6.022 \cdot 10^{23}$/mol is the Avogadro number, A the atomic number of the target. The differential dark matter particle density dn is given by

$$dn = \frac{n_0}{k} f(\vec{v}, \vec{v_E}) d^3v, \tag{1.29}$$

where

$$f(\vec{v}, \vec{v_E}) = e^{(\vec{v}-\vec{v_E})^2/v_0^2}$$

in the simplest models for a virialized halo is a Maxwellian velocity distribution, and which includes a normalization constant k such that the mean dark matter number density is

$$\int_0^{v_{esc}} dn = n_0 = \frac{\rho_\chi}{m_\chi},$$

so the volume integral for k is

$$k = \int_0^{2\pi} d\Phi \int_{-1}^{1} d(cos\Theta) \int_0^{v_{esc}} f(\vec{v}, \vec{v_E}) v^2 dv, \tag{1.30}$$

which simplifies for $v_{esc} = \infty$ to

$$k = k_0 = (\pi v_0^2)^{3/2},$$

and for a more realistic cutoff at the finite galactic escape velocity $v_{esc} \approx 650\,\mathrm{km/s}$, k_0 is modified by a term resulting from the error function,

$$k = k_1 = k_0 \left(\mathrm{erf}\left[\frac{v_{esc}}{v_0}\right] - \frac{2\pi}{\sqrt{\pi}} \frac{v_{esc}}{v_0} e^{-\frac{v_{esc}^2}{v_0^2}} \right). \tag{1.31}$$

In reality k_1 differs only marginally from k_0 for the velocities involved. While the escape velocity determines the maximum recoil energy, the lowest velocity of a WIMP particle required to induce a recoil energy E_{min} is

$$v_{min} = \sqrt{\frac{2E_{min}}{m_N}}.$$

The differential recoil rate can then be written as

$$\frac{dR}{dE_{rec}} = \frac{\rho_\chi}{m_\chi m_N} \int_{v_{min}}^{v_{esc}} \frac{d\sigma}{dE_{rec}} v f(\vec{v}) d^3v. \tag{1.32}$$

All nuclear physics is included in the cross section σ, which depends on E_{rec} and v via the momentum transfer $q = \sqrt{2m_N E_{rec}}$. The WIMP-nucleus cross section term is usually separated into the spin-independent (SI) and spin-dependent (SD) parts

$$\frac{d\sigma}{dE_{rec}} = \frac{d\sigma_{SI}}{dE_{rec}} + \frac{d\sigma_{SD}}{dE_{rec}}. \tag{1.33}$$

The SD contribution is only relevant for the WIMP coupling to the net spin of the target nucleus, which is most cases is small and therefore neglected. For the SI part, on the other hand, the similar WIMP-nucleon coupling to neutrons and protons in the models is used, which results for low momentum transfer qr_n in an A^2 scaling of the coupling strength due to coherent interaction, and can be expressed with E_{rec}^{max} from eq. 1.24 as [22]

$$\frac{d\sigma_{SI}}{dE_{rec}} = \frac{\sigma_0}{E_{rec}^{max}} F^2(q) \tag{1.34}$$

with σ_0 as the total cross section for point-like WIMP-nucleus interactions. Introduced here is also the form factor $F(q)$ of the target nucleus, which contains the loss of coherence at higher momentum transfer. $F(q)$ is often described with the Helm form factor [29], where the nucleus is a sphere with constant charge density[8] and a decreasing Gaussian skin term s near the sphere's surface. The Fourier transform of the density function is a Bessel function of the first order, $j_1(qr_n)$ for the momentum transfer q,

$$F(q) = \frac{3j_1(qr_n)}{(qr_n)} e^{-(qs)^2/2}, \tag{1.35}$$

where r_n is the effective nuclear radius and h/q is comparable to the nuclear radius. The Bessel function is responsible for the shape of the recoil spectra, which show typical dips at the diffraction minima, which for heavy nuclei like tungsten limits the accessible recoil energy range for heavy WIMPs to $\lesssim 40\,\mathrm{keV}$. Choosing a different form factor slightly shifts the minima in the recoil energy spectra. Finally, the differential energy spectrum with these factors can be written in the form

$$\frac{dR}{dE_{rec}} = \frac{1}{2\mu_{\chi N}^2} \frac{\rho_\chi}{m_\chi} \sigma_0 F^2(q) \int_{v_{min}}^{v_{esc}} \frac{f(\vec{v})}{v} d^3v. \tag{1.36}$$

While in eq. 1.34 the total cross section σ_0 is used, for comparisons between experimental results which use different nuclei in general the cross section is normalized to the target-independent WIMP-nucleon cross section $\sigma_{\chi N} = \frac{(1+m_\chi/m_N)^2}{(1+m_\chi/m_p)^2} \frac{\sigma_0}{A^2}$, where m_p is the proton mass.

[8] Here the assumption is made that charge distribution and mass distribution are analog.

1.6.2 Scattering experiments

A number of scattering experiments are listed in this section, containing the main experiments in the field, which are active or already concluded, but with still important or controversial results. In this section only the working principles are described, while in section 1.8 the most important results are recapitulated.

Solid state scintillation experiments

One of the first large scale direct dark matter search experiments was the DAMA/NaI experiment, which employed an array of several large sodium iodine crystals in a low background environment, each read out by a photomultiplier. Special emphasis was placed on the selection of all materials, because with this setup only the trace signal of the deposited energies can be recorded, but no second readout channel was available to distinguish between different classes of recoil events.

The primary goal of the DAMA experiment in this original setup was to search for a modulation in the low energy region of the measured spectrum. Since the solar system moves with a constant speed relative to the galactiv halo, the Earth's motion around the sun creates an annual modulation of the expected number of recoil signals of WIMPs scattering on a dark matter detector. In the absence of all known annual variating parameters, this is considered as a 'smoking gun' observable. After almost continuous operation for seven years, the experiment was upgraded to the DAMA/LIBRA setup with a larger total detector mass of about 250 kg.

Cryogenic phonon/ionization and phonon/light experiments

These types of experiments are based on the ideas of [30, 31] and subsequent papers, which were the initial ideas for direct dark matter detection. Some examples are given here very briefly.

Phonon/ionization The CDMS (Cryogenic Dark Matter Search) and EDELWEISS experiments both run cylindrical Germanium crystals, while CDMS in addition also has Silicon detectors. Both experiments use two readout channels with slightly different methods. CDMS uses phonon collectors to acquire the heat signal, which are read out by four transition edge sensors, operating at temperatures around 40 mK. As a second channel, the CDMS (i)ZIP detectors[9] are equipped with electrodes to acquire the ionization signal created in an interaction. The EDELWEISS collaboration also measures the heat and ionization signals, but use NTD detectors to read out the heat signals.

Both collaborations use highly structured phonon collectors to get a position sensitivity and thus be able to reject surface events. Surface events only create signals in the outer electrode, while bulk events create signals on both faces of the crystal.

Phonon/light A different approach is used by the CRESST collaboration, which similarly to CDMS uses TES detectors at even lower temperatures for the readout. The heat signal is read out by phonon collectors, while the light signal is collected in a physically separate detector consisting of a thin Silicon disc, also read out by a TES. Details on the CRESST experiment will be provided in chapter 2.

Liquid noble gas experiments

Liquid noble gas detectors operating with Xenon or Argon currently have the largest operating detectors in the direct dark matter search field. Most of those detectors are built as a time projection chamber with a liquid and gaseous phase and make use of two distinct signals, which enables a discrimination between nuclear and electron recoils.

Particles interacting with the liquid noble gas create a prompt scintillation signal S1, which is fast and can be immediately detected by photomultiplier arrays. The recoil in the liquid also produces a secondary signal S2 from electrons, which are accelerated in a strong

[9] (interleaved) Z-sensitive ionization and phonon-mediated detectors.

electric field and produce electroluminescence when entering the gaseous phase above the liquid surface. This S2 signal is delayed with respect to S1, and by using highly sensitive photomultiplier arrays, a good positional reconstruction of the original signal is possible, which can be used to define a fiducial volume. The ratio of S2/S1 can then be used to discern recoil signals from electrons and nuclei. Although the discrimination between the two populations is not as clear as in several cryogenic solid state experiments, with statistical methods and neutron calibration good results can be expected.

It is a major advantage of the scintillation properties of the liquid noble gas detectors that the detector effectively shields itself against external radioactivity, which dominantly produces signals in the outer region of the detector. However, in such detectors, special care has to be taken to avoid trace contamination with ^{85}Kr and ^{37}Ar, which both are isotopes with a beta decay and can thus create a low energy background signal within the detector volume.

Other experimental techniques

Other ideas for WIMP scattering experiments include for example bubble chambers and drift chambers. The COUPP collaboration operates a 60 l bubble chamber at SNOLAB with a superheated heavy liquid, CF_3I, looking for the formation of bubbles created by a nuclear recoil. An advantage of this technique is that the detector is insensitive to beta and gamma radiation. However, a serious disadvantage is that an event-by-event energy information and signal discrimination between decay products in the liquid and WIMP recoils is not available. Thus the sensitivity is strongly dependent on the radiopurity of the liquid used for the detector.

The DRIFT collaboration uses low pressure (negative) ion time projection chambers recording the tracks of interacting particles, therefore providing directional sensitivity for WIMPs by design. The WIMP velocity vector for a detector located in the northern hemisphere [32] oscillates with respect to the drift chamber from pointing towards the center of the Earth to pointing south, assuming an essentially stationary dark matter halo. Thus with such a method, a WIMP signal could be positively identified using this signature in combination with the daily and annual rate modulation.

1.6.3 Axion search experiments

The axion search is grouped into the direct search, because axions are directly converted into photons in the search experiments. Due to the expected small mass of axions in the range of meV or even μeV up to about 1 eV direct detection is very challenging.

CAST The CAST (Cern Axion Solar Telescope)[10] operates a LHC-type magnet at CERN, which can be aligned towards the sun. In the strong magnetic field of the magnet of up to $9.5\,T$, solar axions can be converted into x-ray photons via the Primakoff effect. The resulting photons are then detected with highly sensitive CCD and MicroMegas detectors. The experiment is able to observe the sun for 1.5 hours each during sunrise and sunset due to restrictions in the aligning of the magnet, while the rest of the day can be used for background measurements.

Microwave cavity experiments Microwave cavity experiments such as ADMX (Axion Dark Matter Experiment)[11] aim to detect the axion conversion into microwave photons indirectly. The resonance frequency spectrum of a tunable microwave cavity with a strong magnetic field of about 8 Tesla is scanned and the noise level is measured with SQUIDs. When a conversion of an axion into a microwave photon occurs, the noise changes and a signal appears at the axion mass corresponding to the current resonance frequency. The scanning of the resonance frequency range is done in steps of 125 Hz, each of which requires about half an hour of data taking. With the commissioning of a dilution refrigerator to cool the cavity, the noise level could be reduced and therefore the frequency scanning speed

[10] see the experiment's homepage at `http://cern.ch/CAST`.
[11] see the experiment's homepage at `http://www.phys.washington.edu/groups/admx/home.html`.

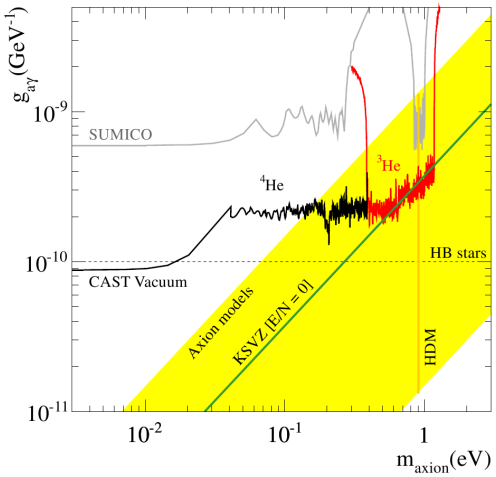

Figure 1.6: Limits on the axion interaction cross section $g_{a\gamma}$ for the mass range meV up to eV from the CAST experiment and astrophysical bounds from [15].

increased by a factor of about 400. ADMX focuses in contrast to CAST on the cosmologically interesting axion mass region in the μeV region and currently has excluded [33] axions as dark matter for $m_a = 1.9 \ldots 3.53\,\mu$eV.

Polarized light An initially positive result in axion searches was claimed in the PVLAS experiment (Polarizzazione del Vuoto con LASer). This experiment uses a polarized laser beam passing repeatedly through a strong magnetic field by reflecting between two mirrors, thus increasing the light path. If an axion interacts in the magnetic field with a photon of the beam, the polarization is reduced and the vacuum becomes birefringent. In [34] the PVLAS collaboration reported a rotation of the polarization, which could be interpreted as a hint for a axion-type light, neutral spin 0 particle.

The result spurred some interest in axion research, and experiments were suggested to test the result (see next paragraph). However, two years later, revised measurements were published by the collaboration without the rotation signature [35, 36].

Light shining through walls experiments After the PVLAS result, the search for axion-like particles (ALP) received renewed interest, and so-called "light shining through walls" experiments were suggested [37] and conducted [38] to test the result. The method employs the regeneration of photons from a strong coherent light source, either a laser or synchrotron xrays from a free-electron laser, within a magnetic field behind an intransparent layer ("wall"). The effect can only occur if the photon is transformed into an axion-like particle via the Primakoff effect, and then regenerated similarly. Shortly after the new PVLAS results were published, the original results indicating a rotation of the polarization were also ruled out by [38].

Cryogenic axion experiments The momentum transfer of a particle with a mass of ~eV or less is tiny and realistically not detectable. However, also cryogenic dark matter experiments could make use of the inverse Primakoff effect. The axion from the sun then transforms in the electric field of the target crystal into x-rays, which are in the keV energy range. This commonly is at the lower end of accessible energies for cryogenic dark matter experiments, because the background usually increases exponentially at small recoild energies, and the signal would be expected in the electron and not the recoil region. Nevertheless, if the background can be suppressed or is well understood at electron recoil energies of $\mathcal{O}(1)$ keV, an observation channel for axions opens up, and for example day/night signal rate differences could be tested similar to the CAST experiment.

1.7 Indirect searches

Indirect dark matter searches utilize the proposed Majorana nature of WIMPs. It is expected that WIMPs are caught (e.g. via a scattering process) and subsequently trapped in regions with high gravitational potential, where they can accumulate over time. Moving towards lower gravitational potential and increasing in density leads to WIMP-dense regions, where two WIMPs can annihilate into different pairs of particles (e.g. $\mu^+\mu^-$, $\tau^+\tau^-$, $b\bar{b}$, W^+W^-), which in turn decay into $\nu\bar{\nu}$ or gamma final states. Experiments then search for the signature of high energy neutrinos or high energy gamma rays from these regions with high mass density. One example for such a region is the sun, which provides the closest notable mass aggregation, others would be large galaxy clusters like Coma or Virgo, but also large galaxies like Andromeda, which could boost the signal by large factors with respect to their environment.

The annihilation rate Γ_A can be expressed with the velocity averaged annihilation cross section $\langle\sigma_A v\rangle$ as [22]

$$\Gamma_A \sim \langle\sigma_A v\rangle\, n_\chi^2, \tag{1.37}$$

where the difficulty for the detection becomes obvious, because Γ_A is proportional to the square of the dark matter number density n_χ. On the other hand, it may be easier to distinguish a signal from background when scanning higher mass density regions. For the scenario of annihilation into neutrinos, the expected flux is given by

$$\frac{d\phi_\nu}{dE} = \frac{\langle\sigma_A v\rangle}{4\pi \cdot 2m_\chi^2} \frac{dN_\nu}{dE} \times J(\Delta\Omega), \tag{1.38}$$

where dN_ν/dE is the corresponding differential muon neutrino yield per annihilation, m_χ is the mass of the WIMP, and $J(\Delta\Omega)$ is the integral over the square of the dark matter density in the line of sight from the observer towards the source of the annihilation.

In indirect dark matter search, there are several satellite experiments, which search for gamma ray excesses above known backgrounds. The first group to report an excess was using the high energy data from the EGRET satellite [39]. However, it is not clear if the detectors are fully understood at these energies. More recently, also other satellites found hints for an excess signal, for example the PAMELA [40,41] and the Fermi [42] experiments. PAMELA reported an excess of positrons, but not antiprotons, as would be expected from dark matter annihilation. Fermi-LAT (Large Area Telescope) reported a small, not very significant statistical evidence ($1.6\,\sigma$ global) of a line in the gamma radiation spectrum of the center of the Milky way at an energy of $\sim 130 - 135\,\mathrm{GeV}$ [43]. The largest Earth based

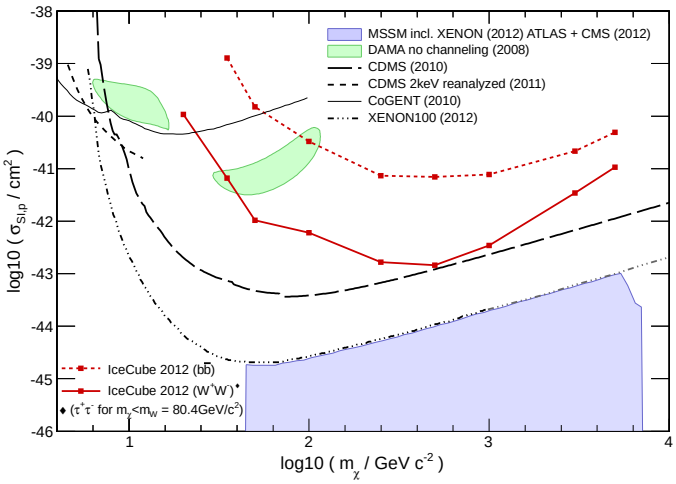

Figure 1.7: Dark Matter interaction limits from IceCube [44].

detector, the IceCube telescope at the South Pole, has its focus on the detection of very high energy neutrinos from cosmic rays. It has a high detection threshold, but can search

for dark matter decay signals with energies above ∼50 GeV. In fig. 1.7 the exclusion limits of IceCube are for shown for different dark matter annihilation channels.

1.8 Overview of hints and evidences in direct searches

After mentioning in the previous section some hints of dark matter in indirect searches, we return to the direct search experiments, were one group already for years and recently several more groups reported hints and evidences of excess signals. The respective detection methods were discussed in section 1.6.2.

DAMA

The first direct dark matter search experiment to report a signal, which as of now is still not fully understood, is the DAMA experiment (**DA**rk **MA**tter[12]), now extended to the DAMA/LIBRA experiment. It was in its first version an array of nine large and very radiopure NaI(Tl) crystals, each with a weight of 9.7kg, read out by photomultipliers. The detector array was housed in a copper box and surrounded by a multi-layer passive shielding against gamma radiation and neutrons. During its run over seven annual cycles the collaboration recorded the signals in the detector array and reported an annual modulation and a signal region as early as 1997/1998. The earlies signal was claimed after an effective exposure of less than two months of data taking in the time frame of one summer and winter period [45], and improving later on [46,47] to a significance of $3-4\,\sigma$ for the oscillation hypothesis. Since then, the modulation signal strengthened with increasing statistics to $6.3\,\sigma$ at the conclusion of the DAMA/NaI experiment, which was subsequently upgraded to DAMA/LIBRA (**L**arge sodium **I**odide **B**ulk for **RA**re processes) with a total detector mass of ~ 250 kg. This setup had new electronics, DAQ, and also a new material selection and radiopurification. It started taking data in 2002 and was upgraded in 2008 and 2010. Together with the previous experiment it has a cumulative exposure of 1.17 ton·years in 13 annual cycles. The modulation signal is indicated in the most recent publications [48,49] to exist with a significance of $8.9\,\sigma$, citing a residual rate (modulation amplitude) of 0.0116 ± 0.0013 counts/(kg·d·keV) in their $2-6$ keV energy range. Recently the final results of DAMA/LIBRA were published [50] with one additional annual cycle, slightly improving these numbers with a significance $9.3\,\sigma$ and a residual rate of 0.0112 ± 0.0012 counts/(kg·d·keV). Also the phase and period are in very good agreement with the expectation from a WIMP signal.

Though the collaboration includes a long and detailed list of many possible contributions to background signals, no background could be identified, which can explain the annual modulation signal. The DAMA and DAMA/LIBRA collaborations both consider the measured modulation as independent of astrophysical and cosmological models, as e.g. used in section 1.6. The reason for the remark that the DAMA result is not yet fully understood is the following. Several other experiments with different techniques have reached sensitivities for Dark Matter cross sections on nucleons, which are orders of magnitude below what one would expect from the DAMA modulation. None of these experiments can detect the expected number of signals. Even when considering that the Dark Matter exclusion plots are strongly model dependent, the experiments would have to see a much larger number of signals in their data.

Other signals and indications

CoGeNT

The CoGeNT collaboration reported an irreducible excess of events at low energies [51] for a two-month measurement as well as an annual modulation signal [52], the latter with a significance of $2.8\,\sigma$ over a measuring period of slightly more than one year with a single 440g p-type point contact Germanium detector with an estimated fiducial volume of 330g. The detector has only one readout channel, but with pulse shape analysis, the collaboration

[12] DAMA collaboration, `http://people.roma2.infn.it/~dama/web/home.html`.

distinguishes surface events from signals deeper in the crystal due to different signal rise times.

Preliminary results indicate that the "rates look flatter", when the second year of data is also included [53], indicating that the significance of the excess did at the least not increase.

CDMS II

The CDMS collaboration re-analyzed older data with a stronger focus on the low energy regime in the Si detectors, which are more sensitive to light WIMPs. In the re-analyzed data set of 56 kg·days, corresponding to an exposure of 10 kg·days of Si, in the first CDMS II five tower run [54] no signal in the $7-100\,\mathrm{keV}$ recoil energy range was detected after cuts.

In the blind analysis of 140.2 kg·days of recent Si only data, 3 events survive all cuts with a signal to noise significance of $> 4.5\,\sigma$ for both detector channels (ionization and charge). For the final data set a background of only $0.41^{+0.20}_{-0.08}(stat.)^{+0.28}_{-0.24}(syst.)$ events would be expected, corresponding to a probability of about 5% that all three events result from known background sources [55]. A likelihood test of (known) background only against WIMP+background hypotheses reduces the probability to slightly less than 0.2%, if the event energies are taken into account.

CRESST II

In the completed Run32 of the CRESST-II experiment, 67 nuclear recoil events were found in the accepted recoil energy region with a corresponding light signal in the oxygen band, where signals from scattering neutrons or WIMPs would be expected. Of these 67 signals, only about half can be explained by known background [56]. Compared to other experiments, this excess signal is quite large, so it may be due to an unknown class of background signals[13]. If one were to explain the excess within a WIMP framework, a likelihood analysis reveals a preferred region of rather light WIMPs, assuming the standard halo parameters, with a rather high significance. In the preparations for the current Run33, several steps have been taken to improve upon the result and test if the excess signal in fact originates from a previously unidentified background source.

Summary of all observations in direct searches

The number of experiments recently reporting very small excesses of signals above the known background is astonishing. For years only the modulation signal claim of the DAMA collaboration, both DAMA/NaI and its successor DAMA/LIBRA, existed in the experimental direct dark matter searches.

Other existing experiments conducted significant upgrades in technique and detector mass (CDMS, EDELWEISS, CRESST), and were complemented by new experiments with solid state (CoGeNT) and increasingly liquid noble gas detectors (XENON10, XENON100, also with its upgrade to 1t, LUX, WARP, and several more). The increasing sensitivity created the situation that more than one experiment found a small number of signals, which could not be explained by the known background sources. However, since the signals are sparse and just at the edge of the experiments' sensitivity, and also most of the detectors have not been taking data for several annual cycles, none of the new results can be considered as clear and concise evidence for dark matter detection.

In particular it should be mentioned that –at first glance– several experimental results, with and without excess signals, contradict each other. With the low statistical significance of the excess signals there is enough room for the results to change with upcoming measurements. A current problem is that the interpretation of the excess signals seen by these experiments in terms of dark matter still needs to also be aligned with the DAMA experiment, whose annual modulation signal is independent of a specific WIMP model.

The recently presented first results from the LUX experiment [57] improved the sensitivity on the WIMP-nucleon cross section by about a factor of three compared to the previously lowest value. More important, however, is the fact that the LUX experiment did not find any

[13] no other experiment uses oxygen as detector material, but other light nuclei such as Si are used, so a WIMP signal of that magnitude would likely have been detected.

excess signals for either low-mass ($< 10\,\mathrm{GeV}$) or intermediate mass ($\mathcal{O}(50)\,\mathrm{GeV}$) WIMPs. Exemplary for the high sensitivity of LUX is that for a WIMP in the favored CDMS-II Si region [55] at m_χ~8.6 GeV and $\sigma_{\chi-N} = 1.9{\cdot}10^{-41}\mathrm{cm}^2$, LUX would expect a clear signal with a population of more than 1500 events [58] in the low energy part of the spectrum below an S1 signal[14] of about 10 photoelectrons with the exposure LUX collected so far. Due to the low background in the fiducial volume and the very small energy threshold for nuclear recoil signals, LUX puts severe constraints on all existing signal (favored) regions and indications for Dark Matter detection, including DAMA. Low mass WIMPs in the region $6 - 10\,\mathrm{GeV}$ favored by several experiments can be considered excluded by LUX in the 'standard' WIMP framework.

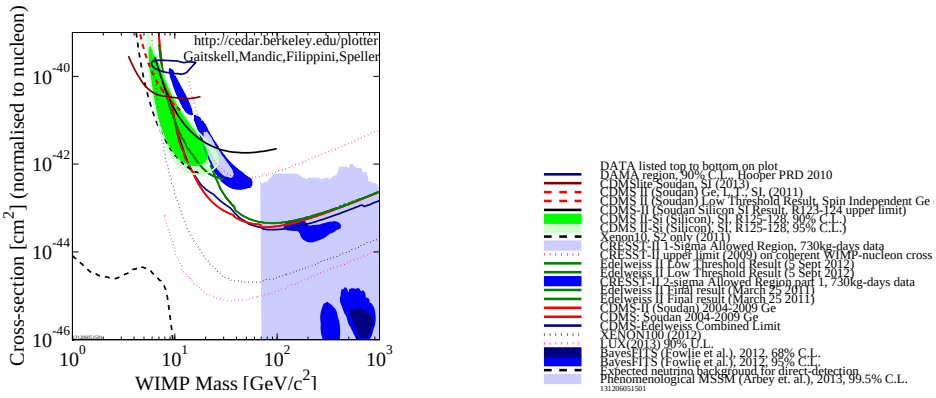

Figure 1.8: Limits on the spin-independent WIMP-nucleon interaction cross section from [59]. Values above the lines are excluded at 90% C.L. given standard halo assumptions.

1.9 Cosmic rays and muons

A short overview of the origin, main components and spectra of cosmic rays and their flux in underground experiments is given here for the aspects needed to understand the importance of a muon veto in underground and low background experiments such as CRESST, as muons are the main cosmic ray component influencing such experiments. For a detailed discussion the reader is referred to textbooks, e.g. [60].

1.9.1 Origin and sources of cosmic rays

Solar cosmic rays

The closest and most visible source is the sun, and solar cosmic rays mostly consist of particles in eruptions on the solar surface and in the solar wind. The composition of the outer shells of the sun is dominated by electrons and ionized hydrogen, i.e. protons, with additional contributions from helium nuclei. While the temperature on the solar surface is only about 6000 K, the temperatures of the solar wind and in coronal eruptions are much higher and easily reach more than $10^6\,\mathrm{K}$ at a much lower density. The energies of the particles in the eruptions and the wind are relatively low in the region of several tens of keV with particle speeds of about 500 km/s in average. Therefore it takes several days for solar cosmic rays to reach the Earth and most particles produce hard X-ray radiation and are stopped in the Earth's atmosphere[15].

Due to the proximity of the sun, solar cosmic rays have a rather large flux in the Earth's atmosphere but can reach the surface mostly at the magnetic poles. This produces the

[14] S1 is the prompt scintillation and S2 the electroluminescence signal.

[15] It should be noted, however, that also protons with energies of several tens of MeV can be produced in solar flares or corona ejections. Because in flares the flux (intensity) can increase by several orders of magnitude, this can result in a serious radiation contamination for astronauts or damage to satellites.

polar lights (aurora) via collisions with atmospheric atoms. The solar wind interacts with the magnetic field of the Earth and creates a so-called magnetic tail in direction away from the sun, which reaches well beyond the Moon's orbit.

Galactic cosmic rays

Cosmic rays of extra-solar origin have a much harder spectrum than the solar wind or flares. The composition is dominated by protons, which make for almost 90% of all cosmic rays, followed by helium nuclei, which contribute $\sim 12\%$. Electrons and heavier nuclei account for about 1% each. At the low energy part of the spectrum, below about 1 GeV, charged particles will not be able to reach the Earth because of the solar wind with its magnetic field. The origin of galactic cosmic rays are assumed to be for example from supernova remnants, quasars and also from the direction of the center of the Milky Way. Of these sources, cosmic rays from supernovae reach the highest energies of up to about 10^{15} eV, but the average energy is much lower at about 1 GeV. This means that most particles can still be stopped in the atmosphere, but causing more hadronic showers because of the higher incident energies.

Extragalactic cosmic rays

Extragalactic cosmic rays strike the Earth's atmosphere nearly uniformly, because the sources are distributed approximately isotropically on large scales in the visible universe. This has been confirmed but for the highest energies, where the Pierre Auger Observatory may have found that the cosmic rays are correlated with active galactic nuclei (AGN), as the 27 highest energy events showed [61, 62]. Those signals have been reconstructed for primary particle energies of up to several 10^{20} eV [61], which actually is a macroscopically measurable energy: a single particle with an energy of $3 \cdot 10^{20}$ eV has about the energy of a tennis ball moving at ~ 160 km/h. At this level, the cosmic ray flux is much less than one event per square kilometer and year.

GZK cutoff Between the AGASA[16] and the HiRes[17] experiments a discussion set in regarding the Greisen-Zatsepin-Kuzmin (GZK) cutoff at the highest energies accessible to the experiments. The GZK limit is suggested as a theoretical upper limit for cosmic ray energies detectable on the Earth. This limit originates from the idea that for extremely high energies cosmic ray protons lose energy by scattering on the 2.7 keV CMB photons via an excitation of a Δ resonance and the subsequent decay, emitting a pion.

$$p + \gamma_{CMB} \rightarrow \Delta^+ \rightarrow \begin{cases} p + \pi^0, \\ n + \pi^+ \end{cases}$$

This process is possible if the CMB photon is blue-shifted in the rest frame of the proton to an energy of at least the pion rest mass. The result of this process is a mean free path, also called the GZK horizon, of about 50 Mpc for ultra high energy cosmic rays (UHECR). Consequently, there should be a sharp decline in the flux of observable proton-like cosmic rays with energies above the GZK limit of $\sim 5 \cdot 10^{19}$ eV. The Pierre Auger experiment clearly supports the HiRes findings [63, 64] and supports the GZK cutoff above about $4 \cdot 10^{20}$ eV [61, 62], which is in contrast to Agasa [65].

Energy spectrum

Figure 1.9 shows the differential energy spectrum of cosmic rays, which can be approximated to a very good degree over many orders of magnitude by a power law

$$\frac{dN}{dE} \propto E^{-n},$$

with an index $n = 2.7$ for $E < 10^{16}$ eV. In the energy region above the knee at $10^{16}...10^{18}$ eV the curve is slightly steeper, so the spectrum is harder with an index of $n = 3$. The origin of

[16] Akeno Giant Air Shower Array operated by the University of Tokyo.
[17] High Resolution Fly's Eye Experiment operated by the University of Utah.

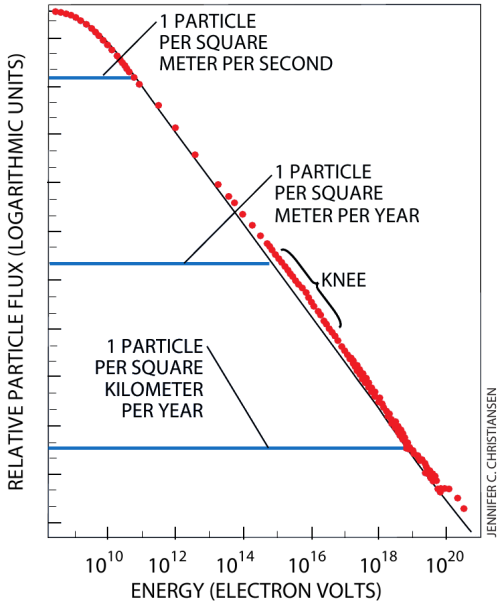

Figure 1.9: Cosmic ray energy spectrum. The flux shows two distinctive changes of the slope, the so-called knee at $\sim 3 \cdot 10^{15}$ eV and the ankle $\sim 3 \cdot 10^{18}$ eV. The origin of both features is still subject of research. Picture adapted and modified from [66], original author S.P. Swordy.

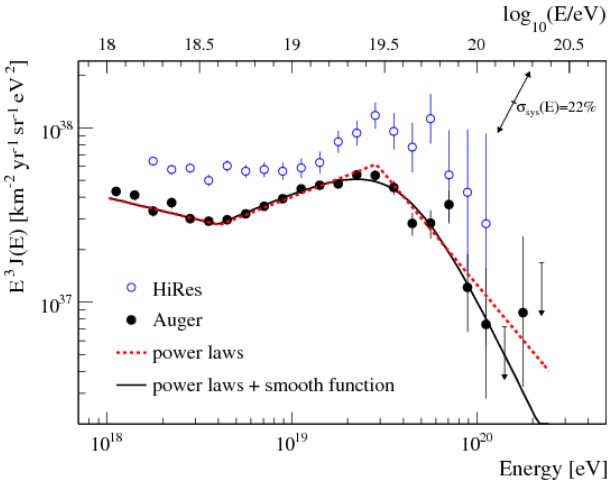

Figure 1.10: Highest energy part of the cosmic ray spectrum with data from the Auger and HiRes experiments. The results seem to confirm the GZK cutoff above $5 \cdot 10^{19}$ eV. Picture from [62].

ultrahigh energy cosmic rays is not known yet. Apart from astrophysical sources theoretical models present a wide range of particle candidates, which can produce such cosmic rays via their decay.

1.9.2 Cosmic ray components

In the previous section it has been mentioned that the composition of galactic and extragalactic cosmic rays is dominated by protons, which make for almost 90% of all cosmic rays, followed by helium nuclei, contributing $\sim 12\%$. Electrons and heavier nuclei account for about 1% each. The protons and heavier nuclei interact in the atmosphere and create secondary particles, which, depending on their energy, can also reach the Earth surface. In

the interstellar space, the particle density[18] is very low with only about $10^{-23}\,\mathrm{g/cm^3}$, or about one proton per $\mathrm{cm^3}$ [67] whereas the atmosphere even at high altitudes is about 20 orders of magnitude denser ($\sim 10^{-3}$ g/cm^3). This creates an enormous stopping power for the cosmic ray particles. Thus the hadrons remaining at surface can also be shielded rather well due to the large interaction cross sections of the particles. Already an overburden of about ten meters of water reduces the flux of the hadronic component by about 50%. The neutrino is of course also a component which penetrates the atmosphere and the Earth, but will not be considered here.

1.9.3 Muon interactions and propagation

Of all cosmic ray components and secondary particles produced in the atmosphere, muons are the most dangerous for low background experiments. As mentioned above, it is rather easy to reduce the hadronic component to negligible levels. Neutrinos from cosmic rays, on the other hand, cannot be shielded and are, with the energies provided by cosmic rays, an object of studies for other large scale experiments like IceCube. Muons remain as the only type of particle with the necessary interaction strength and lifetime to be able to penetrate even large depths. The danger is that in addition they can create tertiary particles, especially neutrons, which typically constitute a background species in dark matter or other low background experiments, which is the most difficult to identify.

Muons are produced in the atmosphere predominantly, where high energy protons collide with nuclei and produce for the main part charged and neutral pions and kaons, where pions dominate due to their smaller mass. Because of the pion rest masses $m_{\pi^\pm} = 139.57\,\mathrm{MeV}$ and $m_{\pi^0} = 134.98\,\mathrm{MeV}$, they mainly decay into muons and electrons, respectively, plus a neutrino. The main decay channels are for charged pions

$$\pi^+ \rightarrow \mu^+ + \nu_\mu \tag{1.39}$$

$$\pi^- \rightarrow \mu^- + \bar{\nu}_\mu \tag{1.40}$$

and for the neutral pion

$$\pi^0 \rightarrow 2\gamma, \tag{1.41}$$

where the lepton numbers have to be conserved. The charged pion decay also has a small contribution of $\sim 1.2{\cdot}10^{-4}$ with a decay into $e^- + \bar{\nu}_e$ and $e^+ + \nu_e$, which is helicity-suppressed due to the much smaller electron mass, as well as a rare decay into $\pi^0 + e^- + \bar{\nu}_e$ or $\pi^0 + e^+ + \nu_e$. For the neutral pion, the second most decay channel with about 1% probability is the Dalitz decay into a gamma and a electron/positron pair. As can be seen, muons are only produced in the charged pion decay due to charge and energy conservation. Since the generating particles have very high kinetic energy, usually orders of magnitude larger than the rest mass of pions and muons, and are massive, in contrast to photons or neutrinos, the muons travel with a preferred direction in the c.m.s.[19]. The mean lifetime of a muon is known to be about $2.2\mu s$. Because of the relativistic velocities, this is enough for cosmic ray muons particles that a flux of about $100 - 200\,m^{-2}s^{-1}$ remains at sea level [6]. Only for initial muon energies $< 10\,\mathrm{GeV}$ the decay becomes important. These energies are not relevant for muons in the LNGS underground site.

Surface muon flux For energies where muon decay is negligible, the differential energy spectrum of muons at the Earth surface can be approximately given by [6, 60]

$$\frac{dN_\mu}{dE_\mu} \simeq \frac{N_0 E_\mu}{1 - Z_{NN}} \times \left(A_{\pi\mu} \frac{1}{1 + B_{\pi\mu} \cos\theta\, E_\mu/\epsilon_\pi} + 0.635 A_{K\mu} \frac{1}{1 + B_{K\mu} \cos\theta\, E_\mu/\epsilon_K} \right), \tag{1.42}$$

[18] This number is just a guidance. The density can vary by several orders of magnitude depending on the type of interstellar medium.

[19] center of mass system.

where constants $A_{\pi\mu}, B_{\pi\mu}, A_{K\mu}$ and $B_{K\mu}$ include the spectrum weighted moments of the particles and the rapidities and velocities (r, γ)

$$A_{\pi\mu} \equiv Z_{N\pi} \frac{1 - r_\pi^{(\gamma+1)}}{(1 - r_\pi)(\gamma + 1)} \tag{1.43}$$

and

$$B_{\pi\mu} \equiv \left(\frac{\gamma + 2}{\gamma + 1}\right) \frac{1 - r_\pi^{(\gamma+1)}}{1 - r_\pi^{(\gamma+2)}} \cdot \frac{\Lambda_\pi - \Lambda_N}{\Lambda_\pi \ln(\Lambda_\pi / \Lambda_N)}. \tag{1.44}$$

Equations 1.43 and 1.44 are similarly valid for kaons by replacing π with K. With eq. 1.43 it is possible to include the zenith angle dependence and therefore create a profile of the overburden.
Using numerical and extrapolated [60] values for the parameters in eq. 1.43 yields

$$\frac{dN_\mu}{dE_\mu} \approx 0.14 \frac{E_\mu^{-2.7}}{cm\ s\ sr\ GeV} \left(\frac{1}{1 + \frac{1.1 E_\mu \cos\theta}{115 GeV}} + \frac{0.054}{1 + \frac{1.1 E_\mu \cos\theta}{850 GeV}} \right) \tag{1.45}$$

For muon momenta $> 10\,\mathrm{GeV/c}$, this numerical approximation is in very good agreement with measurements of the muon flux, below the expression in eq. 1.45 overestimates the flux, because muon decay becomes important. This simple parametrization of the surface muon flux is used e.g. by the large underground experiments MACRO, LVD and Borexino for their depth-intensity relation calculation [68–71].

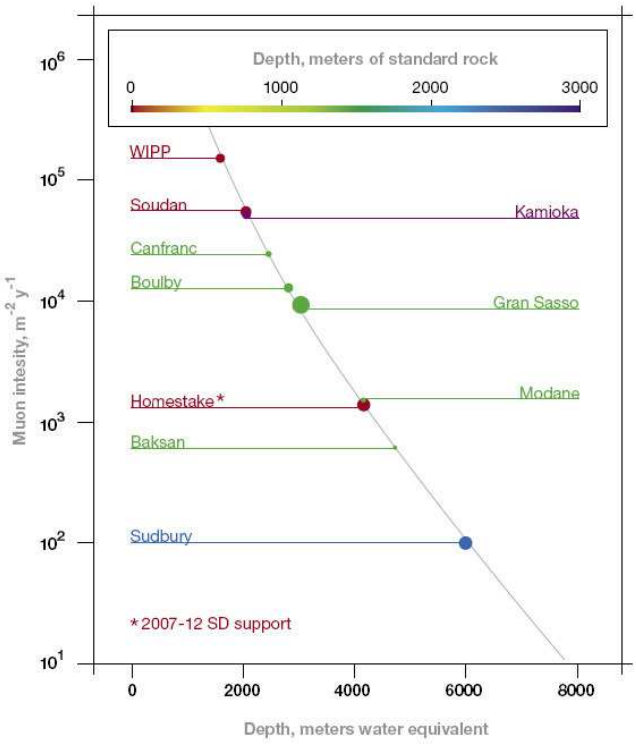

Figure 1.11: Muon flux in the major underground laboratories in the world. The LNGS has an average rock overburden of about 1400m, which translates to 3800 m.w.e. at an average rock density of $2.7\,\mathrm{g\,cm^{-3}}$. The resulting muon flux is approximately 1 muon per square meter and hour. Picture credit: NSF [72].

Muon propagation in matter By travelling through matter, muons lose energy by radiative processes like e^+e^- production, photonuclear interactions and bremsstrahlung as

well as by ionizing the material. The total energy loss can be expressed by a stopping power function [6, 73, 74]

$$-\frac{dE_\mu}{dx} = a + bE_\mu \tag{1.46}$$

where x is the traversed path length in matter, a the ionization energy loss, and b the combined energy loss by the three radiative processes. The parameter $\epsilon \equiv a/b$ defines the critical energy above which discrete radiative processes outweigh the continuous ionization losses. Both a and b are sensitive to the traversed materials [60]. Integrating eq. 1.46 provides the mean energy E_μ of a muon at slant depth X, neglecting the energy dependence of a and b

$$E_\mu = (E_{\mu,ini} + \epsilon)e^{bX} - \epsilon, \tag{1.47}$$

where $E_{\mu,ini}$ is the initial muon energy. Setting the residual energy $E_\mu = 0$, the equation can also be used to get the minimum initial energy required for a muon to reach the depth X from the surface

$$E_{ini}^{min} = \epsilon(e^{X/b} - 1), \tag{1.48}$$

The critical energy ϵ mentioned in eq. 1.46 for muons in standard rock is about 500 GeV. Above this value discrete radiative energy losses become important. For the LNGS rock overburden, this is smaller than the minimum energy a muon initially needs to reach the laboratory, which is ≈ 1.3 TeV. At the LNGS, the mean muon energy is with about 270 GeV [75], much larger than the ≈ 4 GeV at the surface or sea level.

Thus muons can deposit energy by both ionization and radiative processes, i.e. also tertiary particle creation is possible over a wide energy and mass range. The ionization energy loss for muons with $E_\mu > 10$ GeV in rock per distance travelled can be approximated numerically to an accuracy better than 5 % [60, 76] by

$$\frac{dE}{dx} \approx -\left(1.9 + 0.08 \ln \frac{E_\mu}{\mu}\right) \quad \text{in MeV/cm}, \tag{1.49}$$

where E is given in MeV. For practical purposes, e.g. in plastic scintillators, when only the ionization is of interest, this is often approximated as $2\,\mathrm{MeV/(g{\cdot}cm^{-2})}$. The MACRO collaboration measured a value of 1.8 MeV/cm with an error of 2 % for the scintillator oil used in the experiment [77]. Neglecting discrete processes, eq. 1.49 gives a good indication of the energy deposited in a detector by muons. Typically the deposited energy from continuous ionization in detectors of moderate thickness is described by a Landau distribution. This is an asymmetric probability distribution with a long tail towards higher energies, equalling a low chance of a very high energy deposition, and a rather narrow peak around the most probable energy loss, see fig. 1.12.

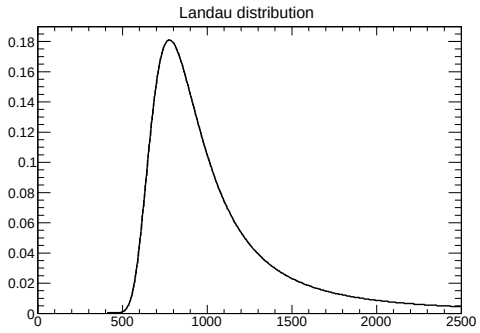

Figure 1.12: Illustration of a Landau distribution function for the energy loss of muons in detectors. In the given example the distribution has a width parameter of 100 and a most probable value of 800 in arbitrary units.

Finally, the intensity of the muon flux decreases exponentially with depth. Neglecting fluctuacions as in eq. 1.47, the muon spectrum at depth X can be expressed as

$$\frac{dN_\mu(X)}{dE_\mu} = \frac{dN_\mu}{dE_{\mu,ini}} \frac{dE_{\mu,ini}}{dE_\mu} = \frac{dN_\mu}{dE_{\mu,ini}} e^{bX}. \tag{1.50}$$

This differential energy spectrum, integrated over the angles and modified by the exponential term due to the slant depth, results in an underground muon flux as pictured in fig. 1.11. In conclusion it is highly important to reduce the flux of muons as much as possible. In the LNGS, with a rock overburden of about 1400 m, corresponding to about 3800 m.w.e.[20], the muon flux is reduced by about a factor of 10^6 with respect to sea level.

Neutron flux in underground labs

The importance of muon identification for low background experiments is emphasized with regard to the aforementioned particle generation by high energy muons. Here again neutrons are mentioned, e.g. from spallation processes. To give an indication, in fig. 1.13 the limitations for dark matter and neutrino experiments by cosmic ray induced neutrons are given.

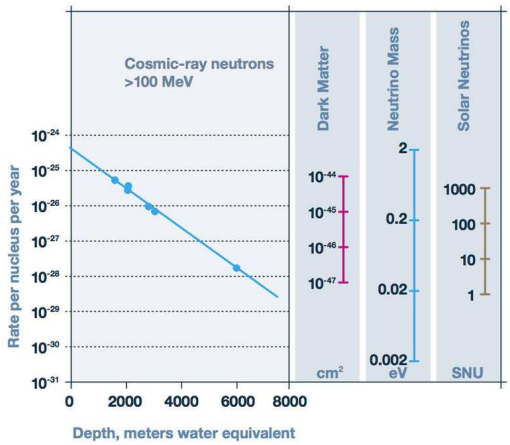

Figure 1.13: Cosmic ray induced neutron flux for different depths of shielding. Indicated are particle interactions and masses, which are limited by this neutron flux. Picture credit: Tommy Phelps, ORNL [78].

[20] m.w.e. = meters of water equivalent. This is the equivalent to the also frequently used 'slab thickness' in units of hg·cm^{-2}. For comparison: the atmosphere's thickness is 1030 hg·cm^{-2} [60]. This means that the energy loss of muons in the atmosphere is 2 GeV.

2

The CRESST experiment

An overview of the experimental site at the LNGS is given here followed by a more detailed description of the CRESST experiment, its setup, and the detectors and their working principle.

2.1 LNGS

Situated below the Gran Sasso massif roughly between Rome and the Adriatic coast near the city of L'Aquila, the Gran Sasso National Laboratory (Laboratori Nazionali del Gran Sasso, LNGS) of the INFN[21] is the largest underground laboratory in the world with an area of about 17 000 m^2 and a volume of 180 000 m^3 of available experimental space [79]. With its own exit in the highway tunnel, there is safe and easy access even for heavy trucks, which is a major advantage compared to the underground laboratories in deep mines, e.g. Boulby or Soudan.

The LNGS consist of three main halls with sizes of about 100 m length, 20 m width and 18 m height each, which contain most of the ~ 20 experiments. Several smaller experiments are located in side tunnels or the connecting areas between the main halls. The main research topics of the experiments are neutrino physics (double beta decay, solar neutrinos, long baseline neutrino experiments), nuclear astrophysics, cosmic ray physics and direct dark matter search experiments. On average, the laboratories have a rock overburden of about 1400m from the Gran Sasso massif, effectively eliminating the hadronic component from the composition of cosmic rays and reducing the flux of atmospheric muons by a factor of about 10^6 compared to sea level [71].

2.2 CRESST site and setup

In this chapter, the CRESST experiment (**C**ryogenic **R**are **E**vent **S**earch with **S**uperconducting **T**hermometers)[22] is presented and the experiment site, setup and working principles are explained in an overview. More detailed descriptions concerning both phases of the experiment are available in several collaboration publications (e.g. [80,81]) and theses (see [82–88] and others).

CRESST has conducted a number of runs since its original commission, which were proof-of-principle experiments with various setups, in two different locations in the Gran Sasso underground laboratory, and in addition operates a test setup between Hall B and C.

[21] Istituto Nazionale di Fisica Nucleare.
[22] additional information is available at the experiment's website, `http://www.cresst.de`.

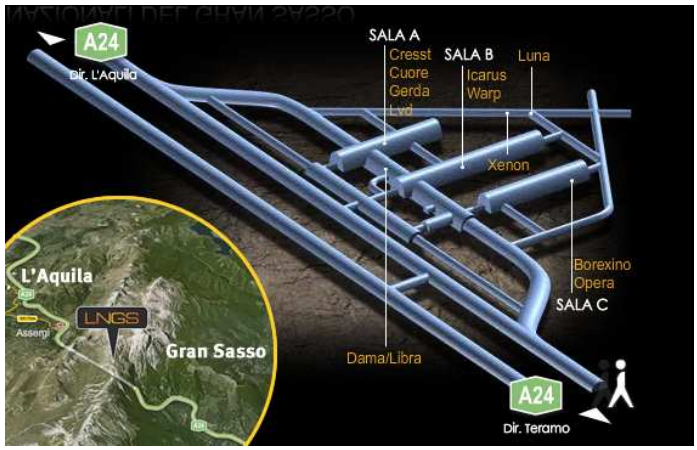

Figure 2.1: LNGS laboratory sketch with indicated locations of the large experiments. Picture credit: LNGS.

2.2.1 General setup

The whole experiment is installed within a building (see fig. 2.4) consisting of three floors of which the lowest one contains the cryostat cold finger with the experiment chamber (see fig. 2.5) in a clean room environment preserved by several filter stages. This low background part is encased in a Faraday cage extending over the ground and first floors.

In the intermediate floor, the DAQ system is installed, and access to the cryostat is possible inside the Faraday cage, whereas the cryostat gas handling is mostly accessible from outside the Faraday cage. The second (top) floor contains a clean room for handling detector modules and provides a small storage and office environment, where the data is stored temporarily before distribution within the collaboration.

2.2.2 CRESST-I

The origin of the CRESST experiment goes back to studies of calorimetric particle detection with superconducting phase transition thermometers, also called *TES*, Transition Edge Sensor [89]. The first installment of CRESST, which aimed at the detection of dark matter particles, only had passive lead and copper layers shielding against gamma radiation from natural decays occuring in the environment. These layers were structured such that the closer the layer is to the detectors, the cleaner the material is. Thus on the outside there is standard boliden lead, encasing an inner structure of high purity copper. Even inside the cryostat with its copper thermal radiation shields for the various temperature stage, the gamma shielding is complemented by additional low radioactivity lead. The whole Pb/Cu shield is enclosed in a gas-tight box ("radon box"), which is continuously flushed with pure N_2 gas evaporated from liquid nitrogen. This standard process used in low radioactivity environments reduces the accumulating contamination on the surfaces with radon gas from the uranium and thorium decay chains.

In the final setup of CRESST-I [80], cubic sapphire crystals with a mass of 262 g and a size of $4.0 \times 4.0 \times 4.1\,\mathrm{cm}^3$ were used as calorimeters, read out by a tungsten superconducting phase transition thermometer. This experiment was able to achieve a very low threshold for recoil signals of less than 600 eV for one detector, above which the trigger efficiency was 100%. With an exposure of 1.5 kg·days a limit on the WIMP-nucleon cross section could be set over a wide mass range, which was due to the light nuclei in sapphire (Al_2O_3) until recently still the best available at WIMP masses of less than 10 GeV/c^2.

2.2.3 CRESST-II

After the relocation of the whole experiment from Hall B to Hall A in the LNGS (see fig. 2.1), the first prototypes of background discriminating detector modules with $CaWO_4$ absorber

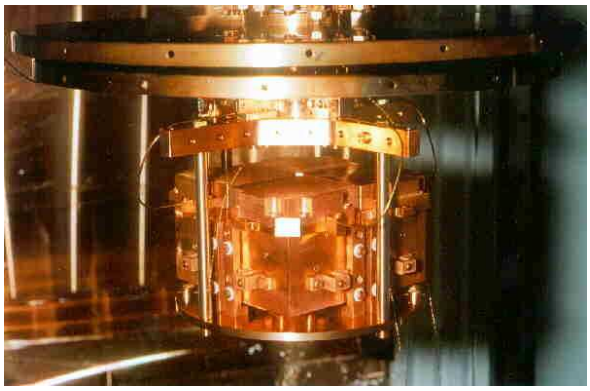

Figure 2.2: Detector holder with four cubic sapphire detectors for a total of ~ 1 kg mass in the first phase of CRESST.

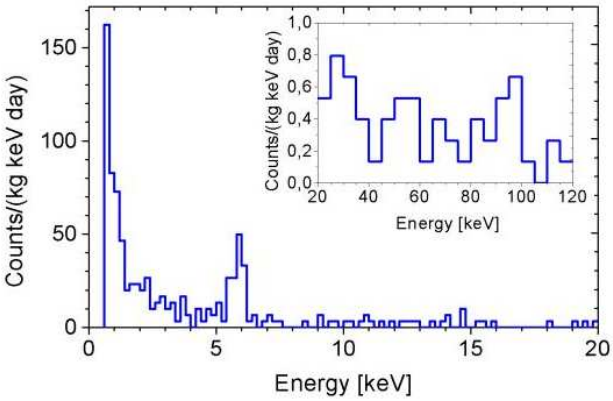

Figure 2.3: CRESST-I energy spectrum of a 1.5 kg.d measurement [80]. Note the low energy scale and threshold. The insert shows the energy spectrum above 20 keV.

crystals have been tested in a low background environment in 2004, yielding promising dark matter results [90] and measuring extremely rare decay processes [91]. This was soon followed by extensive upgrades of the experiment in terms of shielding, electronics and detector capacity.

Shielding

As in most low background experiments, the detector chamber is surrounded by an onion-like shielding structure. In CRESST, this shielding against neutrons, cosmic rays and gamma radioactivity is a combination of active and passive shielding.

Passive Shielding Since the proof-of-principle Run28 resulted in a irreducible background in the nuclear recoil region, and simulations showed [1] that neutrons could be expected in the sensitivity region reached by the measurements, the experiment received an upgrade with a layer of neutron moderating polyethylen. Due to spatial restrictions the neutron moderator had to be installed in several steps on the outside of the Pb/Cu shield with the goal to have at least 45 cm polyethylen (PE) for each line of sight onto the cold box. For this, planks of PE were screwed together to massive blocks surrounding the previously existing Pb/Cu shielding, as shown in Fig. 2.5.

As the Pb/Cu shield was already installed on movable platforms, which can be opened for easy access to the cryostat cold finger, a similar design has been applied for the PE. Three of the massive walls of PE can be retracted, while only one is fixed. For the cryostat feed-through, the shield was put together from 16 single blocks around the cold finger (see

Figure 2.4: View of the CRESST experiment in Hall A at LNGS. The three-story building houses the a clean room environment on the ground level, access to the cryostat and electronics at the middle level and office space on the top. The Faraday cage is decoupled from the exterior structure and spans the lower two floors.

Fig. 2.6). The pillars, on which the cryostat is held with air dampers, are also filled up with PE in the form of pellets.

Active shielding: muon veto After the construction of the neutron moderator, an active muon veto detector system was added between the polyethylen and the Pb/Cu shield. This detector system consists of 20 large plastic scintillator panels, each read out by one photomultiplier, which are mounted on the inside of each block ('wall') of polyethylen, as well as below and above the radon box, see fig. 2.6. With these panels, a solid angle coverage of more than 98% is achieved.

Since the muon veto is the major topic of this work, the next chapter contains some technical information of the material and photomultipliers and details about preliminary testing and the construction on site in the LNGS. The data recorded with this veto detector are the main focus of this work (see chapters 4, 5 and 6).

2.2.4 Detectors

Cryogenic detectors

The working principle of the detectors in both phases of CRESST is based on cryogenic calorimeters consisting of absorbers and highly sensitive read-out sensors. This combination offers the possibility to choose between different absorber materials.

The read-out sensors used in CRESST are superconducting transition edge sensors, which measure the change ΔT of the temperature induced by an energy transfer ΔE to an absorber crystal. Using the heat capacity C of the absorber, the basic approximation is given by

$$\Delta T = \frac{\Delta E}{C}. \tag{2.1}$$

In this simplified picture, the temperature change is proportional to the energy deposited into the absorber. It is clear from eq. 2.1 that a small heat capacity is needed to achieve a large temperature change for a given energy deposition in a crystal.

In cryogenic experiments, the operating temperature depending on the target material used in various experiments is in the millikelvin region at about 10–100 mK, which is orders of magnitude lower than the Debye temperature of the relevant target materials. Since at low

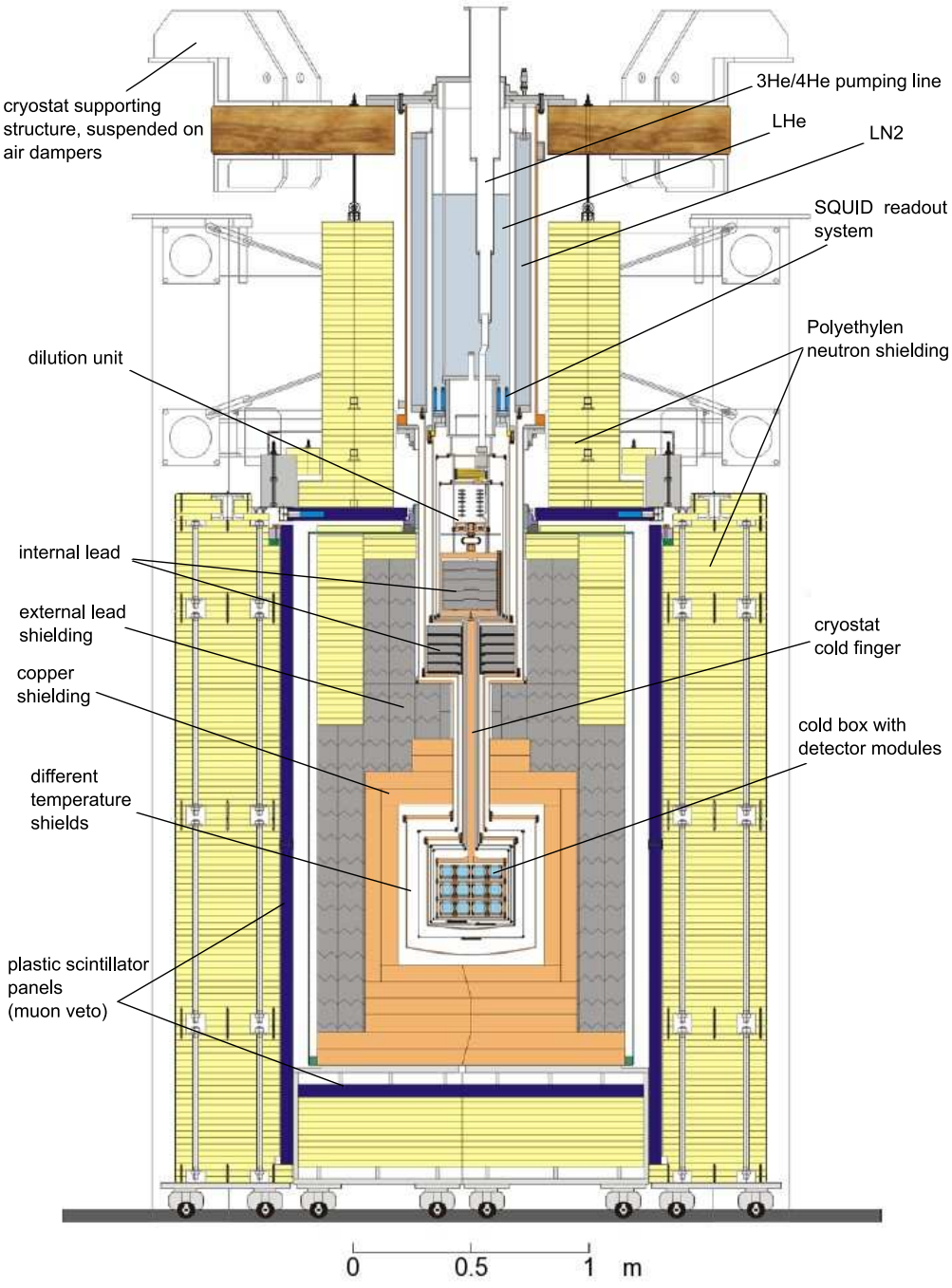

Figure 2.5: Setup of the CRESST experiment. The whole construction is located within a Faraday cage to reduce electromagnetic interference. Indicated with labels are the different layers of active and passive shielding.

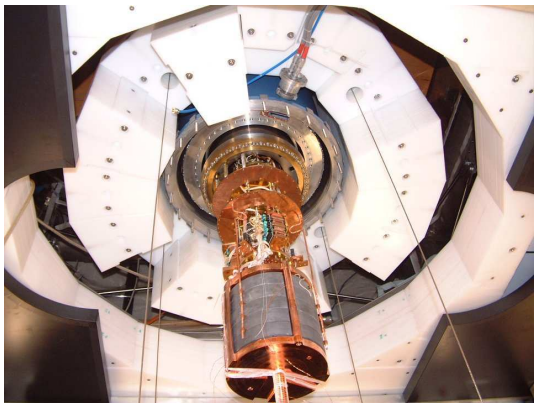

Figure 2.6: Polyethylen (white), (ceiling) veto panels with cut-out (black) and cryostat cold finger with internal lead viewed from the floor. The detector space ('cold box') below the internal lead is not visible in this picture.

temperatures the heat capacity $C \sim T^3$, eq. 2.1 immediately demonstrates the importance of operating the sensors at cryogenic temperatures.

Signal generation and readout principle

Incident particles colliding with a nucleus in the detector transfer momentum and therefore create phonons in the crystal lattice. These phonons propagate through the crystal and are absorbed by the aluminum phonon collectors, which are operated in their superconducting phase. The phonons break up the Cooper pairs and the resulting quasiparticles are transferred to the TES thermometer. The small temperature change through the energy (heat) from the quasiparticles drives the thermometer from the superconducting to the normal conducting phase, hence the name "transition edge sensor". This implies a drastic change in the resistance of the TES, and thus a change in the current through the sensor. The induced magnetic field change can in turn be measured by an extremely sensitive SQUID circuit (fig. 2.7). Details on the model for the signals can be found in [92] and [93].

Since the thin film detectors of different target crystals generally do not have the same transition temperature, the base temperature of the cryostat needs to be stabilized at a lower temperature than the single channels. The CRESST cryostat achieves a base temperature of about 7 mK, which is sufficiently low to operate the tungsten thermometers. For the

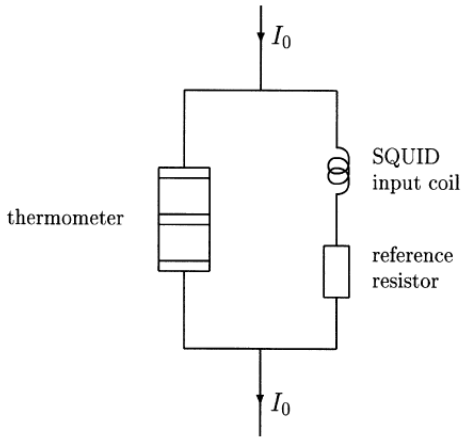

Figure 2.7: Readout scheme of a detector. Both light and phonon detectors are equipped with a TES, which is read out by a SQUID. I_0 is the bias current through the SQUID.

CRESST-II setup a new SQUID readout system was developed by the Oxford group capable

of handling up to 66 channels [84, 94] for a total of 33 standard detector modules.

Detector modules

After the final energy spectrum of CRESST-I with sapphire detectors showed a large background at small recoil energies, phase II of the experiment started with newly developed detector modules. These consist of an absorber crystal, which produces scintillation light in addition to the recoil signal, and a separate light detector made of a thin disc of either silicon or silicon-on-sapphire. Operating at very low temperatures, both detector channels are read out by superconducting thermometers.

There are several reasons for the switch to a completely new type of detector. As mentioned, phase I of the experiment suffered from a steeply increasing number background signals at low energies, which could not be discriminated. After the upgrade of the experiment, a new target material was investigated. The main crystal of choice, calcium tungstate[23] ($CaWO_4$), also produces scintillation light. In a proof-of-principle experiment [95] a strong discrimination between so-called electron recoils and nuclear recoils could be shown. In this first demonstration with a small crystal already a rejection factor of 99.7 % for recoil energies larger than 15 keV could be achieved. Since the sensitivity for WIMPs is larger at small recoil energies due to the exponential spectrum (see section 1.6), a discrimination threshold as low as possible is desired. Therefore the collection of all produced light is highly important, since only about $1-2\%$ of the deposited energy is converted into scintillation light. In the currently used detector modules, the discrimination power between electron and nuclear recoils is strongly dependent on the quality of the light detector. The light collection efficiency in a module is increased by inserting the absorber crystal in a housing covered by a highly reflecting foil. Only a few parts in the module, such as the holding clamps, could not be covered with the reflective foil.

Another reason for using new detector modules is that with a multi-target crystal it may be possible to discriminate between neutron-like and WIMP-like nuclear recoils, depending on the WIMP mass. $CaWO_4$ presents a unique possibility as it covers a wide range in A, from 16 to 184. The modularity of the new detectors also offers the chance to explore other absorber target materials. Starting with Run32, also other materials were included in the background runs. For Run32, several $ZnWO_4$ crystals were added, but finally not used for the dark matter results.

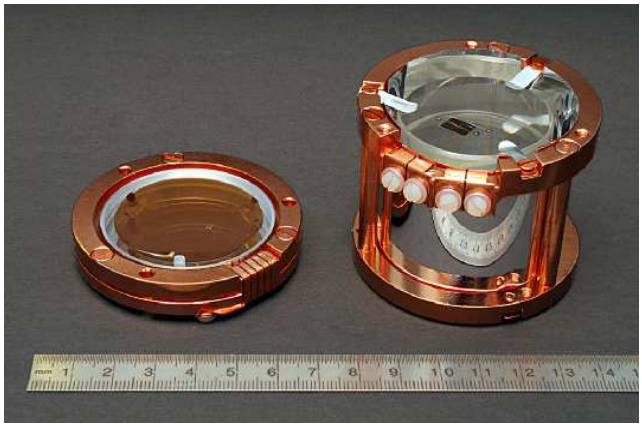

Figure 2.8: CRESST II detector module. Left: copper holder with Si disc, which is held in place with clamps. The TES is the bright spot, slightly off-center. Right: copper holder with reflecting foil. The cylindrical $CaWO_4$ absorber can be seen held by clamps. The rectangle on the top surface is the Al phonon collector with the TES.

[23] The naturally occuring crystals are known as scheelite.

New detector concepts for Run33

Different classes of background signals could be identified in several CRESST background runs with the phonon/light modules. Some background may have been introduced with the detector holding clamps, which had been not been covered with scintillating or reflecting material. This can lead to fake nuclear recoil signals, because the corresponding light signal is missed. Other background populations emerged in the long data taking of Run32, with signals in the nuclear recoil range. Since WIMPs are expected to primarily interact with the nuclei in the target crystals, background signals of this kind needs to be avoided.

As a result of these background populations, in the recently started Run33 some new concepts are investigated. Specifically two modifications are noteworthy: one detector module is modified such that there are no clamps directly on the absorber, but the $CaWO_4$ crystal is held in place by small sticks also made of $CaWO_4$. An advantage is that the material of clamps and target is the same, which avoids possible phonon loss and also stress on the target crystal due to e.g. different cooling constants. The second new type of detector is more concerned with improving the light detector. In this module, the $CaWO_4$ target crystal is inserted in Si beaker, which is functioning as a fully covering light detector. This insures that the whole absorber area is covered with a light sensitive surface and there is no dark area. The Si beaker again is read out by a TES.

Additionally, new $CaWO_4$ crystals produced by the TU Munich group in the CRESST collaboration show a much better radiopurity compared to crystals bought from other sources. Probably the controlled environment parameters using inert gas in the Czochralski process contribute to the lower activity levels.

3

Muon veto detector

This chapter is mainly concerned with the description of the muon veto detector as well as the definition of the trigger and event structure. This is important for an understanding of the notation used in the subsequent chapters. The three Runs 30, 31 and 32 of CRESST are taken into account.

3.1 Veto detector construction and properties

Design and detector supplier

Since the CRESST-II experimental setup utilized the already existing infrastructure from the CRESST-I experiment, the veto design inherited some limitations. An active muon veto on the outside of a neutron moderating shield would be desirable, which would allow the tagging of cosmic ray shower induced neutrons, but spacial requirements did not permit this. A plastic scintillator type veto was designed at the Max Planck Institute for Physics in Munich. The panels used for the CRESST muon veto consist of three different shapes (table 3.1) according to the constraints at the experimental site. For the veto the BC-408

panel type	width	length	cut-out radius
ceiling	800	1616	295
floor	715	1430	
side	770	1350	

Table 3.1: Plastic scintillator panel sizes in [mm]. All panels have a light tight cover.

plastic scintillator from Bicron (Saint-Gobain Crystals) was selected, which is described by the manufacturer as the best general purpose material suited for large area applications. It has a large attenuation length of 210 cm and a light output at the level of 64% of anthracene, according to the data sheet[24] in fig. A.2. While the BC-404 scintillator has a higher light output and a lower maximum emission wavelength, the light attenuation lenght is much shorter than for the BC-408, which is a disadvantage for the large sized panels used in CRESST. The wavelength of maximum emission of BC-408 is at 425 nm (see fig. 3.1a), which is in very good agreement with the ET9900B photomultiplier's maximum quantum efficiency (fig. 3.1b).
In the initially delivered photomultiplier electronics a condensator was missing, which is essential for the electric safety of the photomultiplier. This problem was subsequently solved by Bicron personnel for all but the ceiling panels, for which a different solution with an

[24]The corresponding data sheet is included in Appendix A.1 for the reader's convenience, and additional information can be found on the manufacturer's webpage [96].

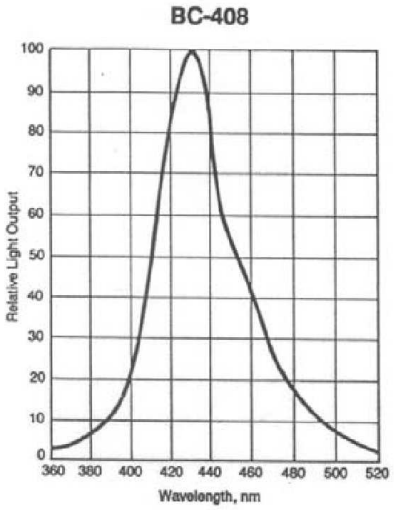

(a) BC-408 emission spectrum taken from the Saint-Gobain data sheet [96], with a maximum light output slightly above 430 nm (data sheet: 425 nm).

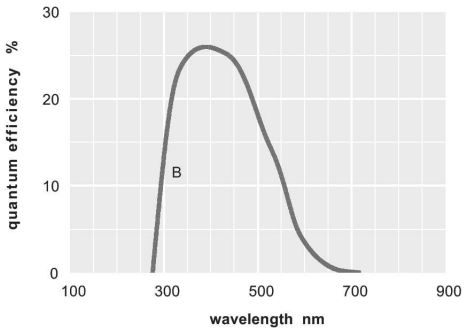

(b) Typical quantum efficiency for a ET9900B photomultiplier, picture taken and modified from the data sheet [97]. The broad sensitivity range easily covers the peaked light output spectrum of the scintillator.

Figure 3.1: Scintillator and PMT response. The data sheets are listed in App. A.1.

external adapter holding an additional resistor was developed due to spatial restrictions. For all practical purposes in CRESST, calibration measurements and background data taking, the signals produced in the scintillator and the photomultiplier are very fast compared to the time window for recording data and even more so with respect to the signals from the massive cryogenic detectors. Therefore the scintillator rise and decay times of 0.9 and 2.1 ns, respectively, are not relevant in the discussion. These times are also much faster than the signal rise time of 15 ns in the ET9900B photomultiplier. The latter would only be an issue, if in further developments the signal traces were to be recorded with a fast (flash)ADC. In the current setup, however, only the integrated charge, i.e. the signal pulse height, of the photomultiplier is recorded.

Installation at the LNGS

The on-site mounting of the muon veto detector system at the Gran Sasso laboratories within the existing CRESST experiment setup was done after the conclusion of Run28 and after the upgrade of the experiment with the polyethylen neutron shield. The blocks of polyethylen were designed in a way to hold most parts of the scintillator panels, see e.g. fig. 3.3.

Initial settings

The initial setting of the muon veto system was designed to have a high acceptance and a low threshold for detecting signals. Due to the fact that photomultipliers typically have a high dark count rate in the $\mathcal{O}(10^3\,\mathrm{s}^{-1})$ or even $\mathcal{O}(10^6\,\mathrm{s}^{-1})$ range, depending on their high voltage setting, a filter for these signals and other "noise-like" signals is needed in a low-background, low count rate experiment like CRESST. Even though the ET9900B photomultiplier integrated into the scintillator material has a nominal dark count rate of only $300\,\mathrm{s}^{-1}$ at 800 V, and is operated at voltages > 900 V in the experiment, this rather low dark count rate would be unnecessarily high for the data acquisition in CRESST and would also introduce an abnormally large dead time if used in coincidence with the detector modules. In practice, this issue is solved by implementing electronically a readout suppression: each single photomultiplier signal is required to surpass a fixed pulse height threshold to be read

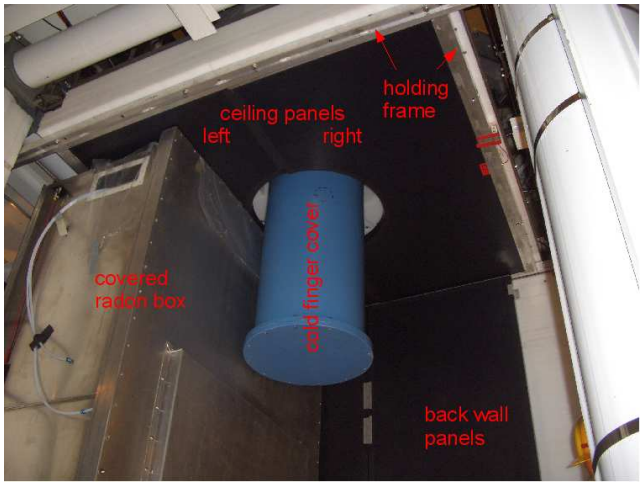

Figure 3.2: Open radon box with several veto scintillator panels in the background, mounted on the polyethylen neutron moderator. The lead/copper shielding is covered during work on the cryostat to avoid any contamination. The picture was taken between two runs, and the blue cylinder is only a cover which ends above the actual position of the cold chamber. The white pillar on the right is also filled with polyethylen.

out. This is from here on called the *panel trigger*, as this method defines signals in each single panel.

Because the scintillator panels used in CRESST have a rather large area, there is a high chance that they collect events from radioactive background from the surrounding material. This is mainly the steel structure of the radon box and lead inside this box, which has intrinsic trace contaminations from Uranium and Thorium and their respective daughter nuclei in the decay chains. This background typically consists of Compton scattering from gamma rays in the low MeV range. Most of this background can also be reduced by a suitable selection of the panel trigger level. This is independent of the veto trigger itself, which in most cases[25] is only active for the (integrated) combined sum signal of all photomultipliers. For this sum signal, there is no additional restriction or suppression on the readout as for single panels.

3.2 Test and calibration of veto system

Characterization and test of detector panels

A series of initial tests and measurements of the plastic scintillator panels were done involving several steps. Some of these tests and the panel characterization were performed in the laboratories at the University of Tübingen. Most notably, a dedicated experimental setup was developed in the thesis by D. Nicolodi [99], which allowed for automatic grid scans of scintillator panel area. For the technical details regarding the test setup, the reader is kindly referred to the cited thesis. A calibration with muons as well as radioactive sources was possible with measurements at Earth surface a due to the large flux of cosmic muons. These scans were used to produce signal response maps for each of the panel types with a grid size of $10 \times 10\,\mathrm{cm}^2$, using different gamma sources and cosmic muons. The measurements were conducted at a height of about 470 meters above sea level with an overburden of a few m.w.e., only slightly reducing the muon flux. In [99] two high energy gamma sources were used, namely ^{228}Th, which supplies the 2.614 MeV gamma energy from the ^{208}Tl decay, and ^{60}Co, which offers 1.17 MeV and 1.33 MeV gamma energies. For the decay gamma energies of both sources the Compton process is the most probable interaction type in plastic scintillator material, with the Compton edges at 2.38 MeV, 0.96 MeV and 1.12 MeV,

[25] The exceptions are noted in the following sections.

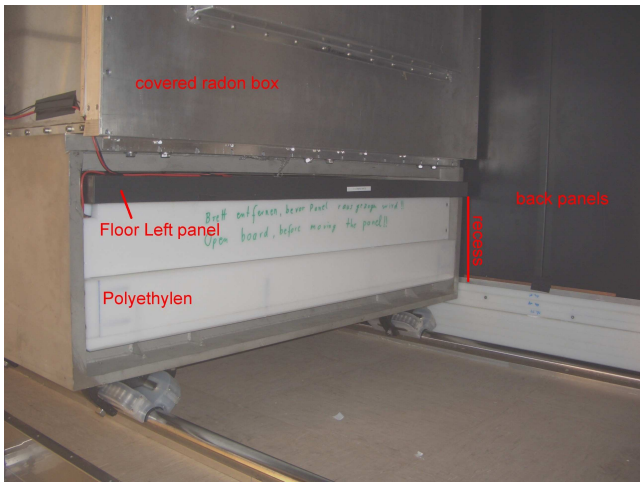

Figure 3.3: Floor panel outside the radon box, directly below the lead/copper shielding. In the backdrop one of the side walls of the veto is visible. Here the recess of the floor panels with respect to the lower edge of the side panels can be seen. This leaves open the possibility for additional signals from muons passing only one panel.

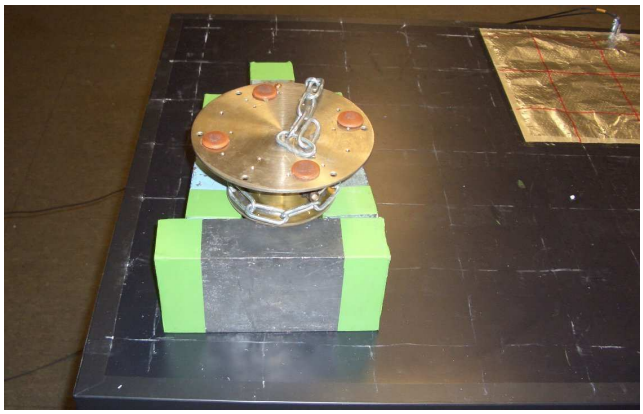

Figure 3.4: Simple setting of panel 10x10 cm^2 grid scan with a lead-shielded collimated gamma source. Later an automatic source positioning system was used [99].

respectively. Because the energy resolution of the plastic scintillator and the photomultipliers is rather low ($\sim$20-30%), the two lines in the ^{60}Co spectrum cannot be distinguished. But since the line intensities are almost the same, one can use the mean energy of 1.25 MeV for further considerations. For this energy, the most probable momentum transfer of the gamma particle at backscattering under an angle of π and thus the maximum electron energy can be determined to

$$\begin{aligned} E'_e &= E_\gamma \left(1 - \frac{1}{1 + E_\gamma/(m_e c^2)(1 - cos\Theta)}\right) \\ &= E_\gamma \left(1 - \frac{1}{1 + 2E_\gamma/(m_e c^2)}\right) \\ &= 2\frac{E_\gamma^2}{m_e c^2 + 2E_\gamma} \end{aligned} \tag{3.1}$$

which defines the Compton edge at 1.04 MeV for the given mean gamma energy. For linear signal amplification this leads to the conclusion that the pulse height of a 1 MeV gamma ray would be at about 10% of the peak position of a muon signal. This results from

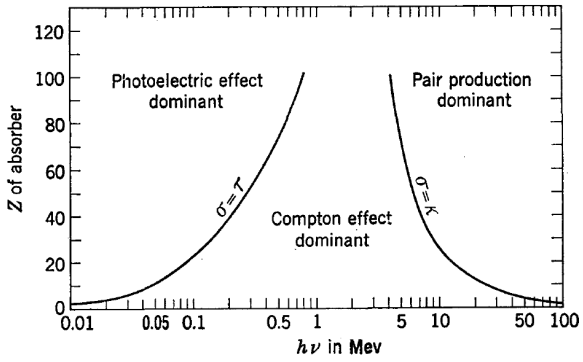

Figure 3.5: Energy regimes for gamma rays, where either the photoelectric, Compton scattering or the pair production process dominates. At the solid lines the effects are equal. In plastic scintillator consisting of low-Z material (C/H ≈ 1) the Compton effect is dominant for all relevant photon energies. Picture from [100].

assuming that the mean deposited energy of muons in plastic scintillator of 1.9 MeV/cm in combination with the muons passing a thickness of 5 cm material creates signals with energies of ∼10 MeV.

Grid scan results

The results from the grid scan show some interesting results. At first glance fig 3.6 and fig. 3.7 agree rather well. Especially close to the photomultiplier position a higher light yield is expected. In the simulation results in figure 3.7 the pulse heights on average vary by a slightly greater degree compared to the measurements with calibration sources. The grid scan measurements show only a few points where the sample differs by more than 10% from the average, and also the pixels close to the photomultipliers are enhanced less than in the simulation, which may be due to direct hits on the phototube in the simulation. According to the data sheet [96] the mean free path for a typical photon is 210 cm, considerably longer than the maximum possible path in any of the used panels, neglecting the photomultiplier's diameter.

panel type	max. path
ceiling	114 cm
floor	101 cm
side	140 cm

Table 3.2: Longest light path to the PMT without reflections for the all panel types.

Surface level calibration with cosmic ray muons

High statistics calibration measurements with muons at surface level[26] were conducted on the outside at the Max-Planck-Institut für Physik in Munich, where the muon flux is at a level of about $100 - 200\,\mathrm{m^{-2}s^{-1}}$. For these measurements the electronics subsequently employed in the CRESST setup was used and also tested. During the measurements, for a horizontal panel configuration, the standard setting of shifting the maximum of the Landau distribution in pulse height to about channel 2000 of 4096 was introduced by varying the high voltage for the photomultiplier. Being at the center of the DAQ range, this provides an easy identification of muons in measurements without large overburden. Because the overall high voltage supply delivers only one common voltage level, in the final DAQ setup the voltage for each photomultiplier was adjusted by a potentiometer to its preset level.

[26] The muon flux depends on the altitude; a more accurate flux of $180 \pm 20\,\mathrm{m^{-2}s^{-1}}$ can be found in [101] from measurements at Pyhäsalmi (Finland).

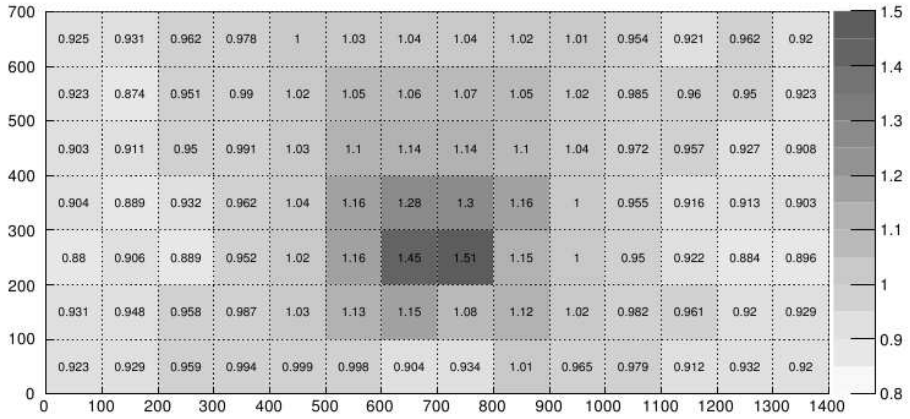

Figure 3.6: Measured grid scan results for one panel from [99]. The axes represent the length/width coordinates in cm, while the greyscale color coded grid entries denote the pulse height response relative to the panel average. Only close to the photomultiplier, which is located at the (700,0) position in the figure, the values differ significantly from the average.

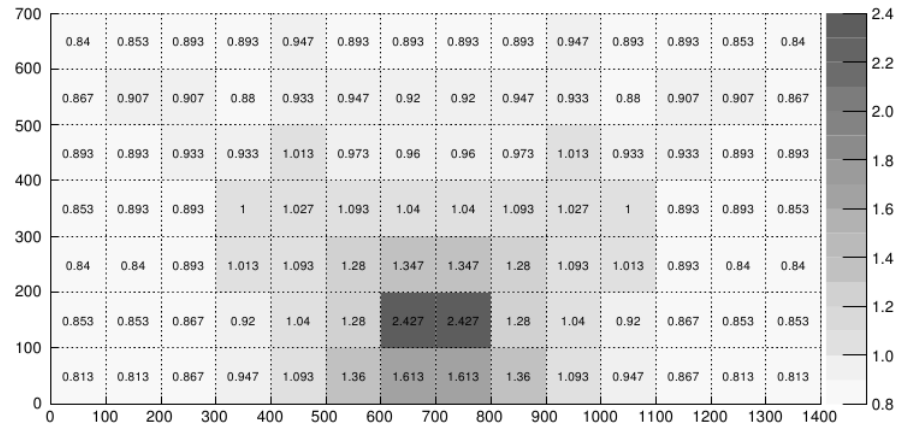

Figure 3.7: Grid scan results from simulation [99], with the axes, scales and PMT position as in fig. 3.6 above. The general picture agrees very good with the measurements. It is noteworthy, however, that the deviations from the average are much larger in the simulation results.

New veto calibration

In preparation for the CRESST Run33, a re-calibration with high energy γ source was carried out. Standard γ sources have a maximum energy of 2.614 MeV from ^{208}Tl from the Thorium decay chain and mainly interact via Compton scattering (see fig. 3.5) in scintillator material. To make use of the full available range of the DAQ, since muons crossing the material deposit on average about 10 MeV, the signals from the calibration sources (^{60}Co) needed to be amplified.

Data files

The muon veto data at Gran Sasso are written to disk separately from the signals from the cryogenic TES detectors in binary files with the identifier ".qdc", as they are recorded by a Charge-to-Digital converter (QDC). In the parameter file, which is the file describing the data recording structure, all settings of the DAQ parameters are readily available in plain text.

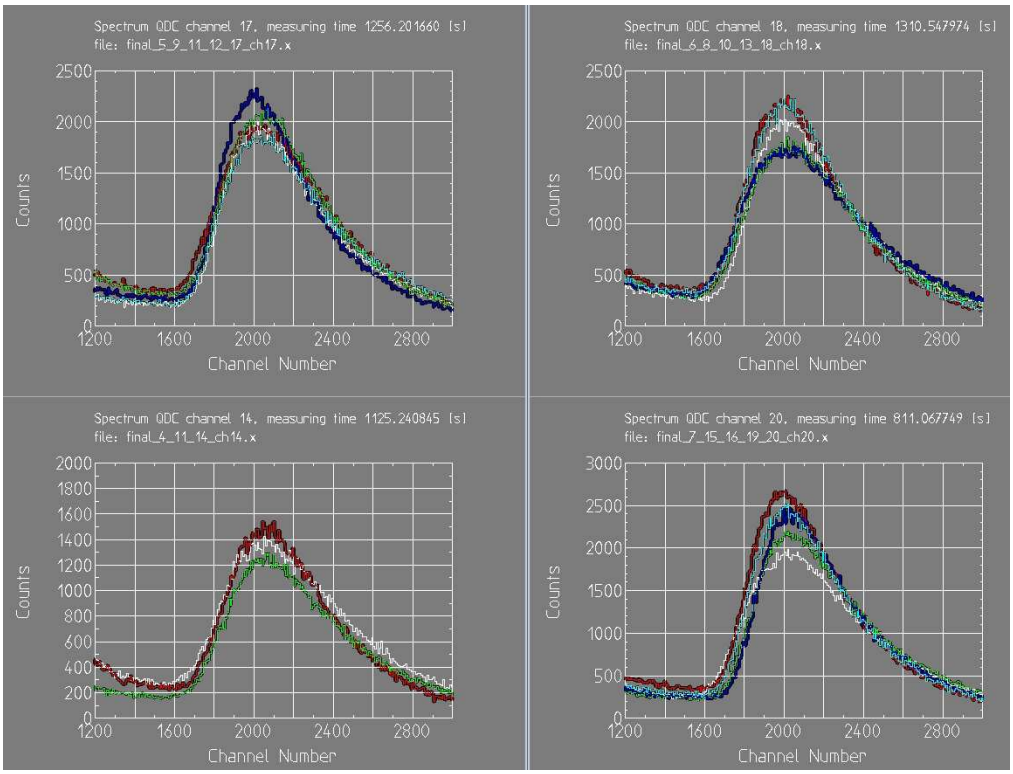

Figure 3.8: Example screenshot of test and calibration pulse height spectra from surface level measurements done in Munich. The maximum of the Landau distribution created by the muons was positioned at a pulse height of about 2000 channels to be able to easily identify muons.

#	abbr.	name	#	abbr.	name
1	cl	Ceiling Left	3	fl	Floor Left
2	cr	Ceiling Right	4	fr	Floor Right
5	ftr	Front Top Right	13	btl	Back Top Left
6	ftl	Front Top Left	14	btr	Back Top Right
7	fbr	Front Bottom Right	15	bbl	Back Bottom Left
8	fbl	Front Bottom Left	16	bbr	Back Bottom Right
9	rtf	Right Top Far	17	ltn	Left Top Near
10	rtn	Right Top Near	18	ltf	Left Top Far
11	rbf	Right Bottom Far	19	lbn	Left Bottom Near
12	rbn	Right Bottom Near	20	lbf	Left Bottom Far
21	sum				

Table 3.3: List of the channel numbers and the corresponding panel names. Two- and three-letter abbreviations in the text and pictures use the first letters only.

DAQ settings and trigger definition

The DAQ settings leading to trigger definitions of veto events for single panels as well as the sum signal are discussed in this section. As already mentioned in the setup description, these do not result in the actual trigger signal rates of each photomultiplier, but rather the event rates generated by the combination of a sum trigger and the electronic readout suppression of the panels. In the language used here, the terms trigger rate and event rates will be used similarly in the context of muon veto events.

To understand this nomenclature, the standard trigger and readout settings for the muon veto DAQ (QDC) are provided in Tables 3.4 and 3.5, as they were used in Run32. At the beginning of Run32 before the file bck_014, there were several modifications in the DAQ

settings, e.g. trigger enabled on all channels, which is why these data files are not used in the analysis. In all other data records, the settings were retained with a few exceptions, which do not influence the data taking. During some short measurements, all available QDC channels were enabled. But since the unused channels (numbers > 21) were unoccupied and also the readout suppression was set to a very high value, the veto data is not influenced.

	QDC trigger				
channel	enabled/disabled (1/0)				
1-5	0	0	0	0	0
6-10	0	0	0	0	0
11-15	0	0	0	0	0
16-20	0	0	0	0	0
21	1				

Table 3.4: Standard trigger settings during Run32, 31 and 30: all single channels are disabled except for the analog sum channel, which has a threshold of 60 mV. Thus signals are recorded *only if* the analog sum of the panel photomultiplier surpasses the threshold. This trigger is also called *sum trigger* in the text. These conditions are subject to changes in Run33.

channel	readout threshold for panel trigger [ch]				
1-5	96	96	96	96	96
6-10	96	96	96	96	96
11-15	96	96	96	96	96
16-20	96	96	96	96	96
21 (sum)	0				

Table 3.5: Standard QDC readout settings during Runs 30–32. All available channels with signal values greater than the suppression threshold are read out. The sum signals therefore have an effective trigger threshold of 60 mV.

Trigger and event definition

There are effectively two different trigger definitions generally used in the experiment until Run32:

- The sum channel is the only channel which has a hardware trigger requirement and is recorded whenever this condition is met. Those events are called **sum trigger** or **sum signal** here. The standard trigger value was set to 60 mV.

- In addition a digital threshold called 'readout suppression' (Table 3.5) is used for the single photomultiplier channels to avoid large amounts of low energy or noise signals. The signal pulse height value for a panel is only recorded in addition to the sum signal if it surpasses this digital threshold. We call these signals **panel triggers** or **panel signals**, or according to the number **m** of recorded photomultiplier signals **multiplicity m signals**.

This means that according to the 21 different channels an event is described by the formula $sum + m \cdot panel$, with the multiplicity m ranging from 0 to 20. In the following, the words "trigger" or "signal" are used within this context, while "event" in general is the record of an event in the veto DAQ. Note that these definitions are not valid anymore for Run33, where the trigger settings have been changed.

3.3 Veto induced dead time

The DAQ time needed to acquire and read out a single event is short, but contributes to the overall DAQ dead time. The time window of the logical signal for both the multiplicity and summation has a length of about 500 ns. The readout time needed per event in the QDC is about 8 μs, during which no veto events can be recorded. For a realistic overall rate of recorded veto events of $\approx 5\,\mathrm{s}^{-1}$, the DAQ induced dead time fraction is

$$8\mu s \cdot 5 s^{-1} = 4 \cdot 10^{-5},$$

which can safely be neglected. One has to remember that this is only for the veto data and does not include coincidences with signals in the detector modules. Without including a selection bias, one has to use the full time window, which would be blocked after a veto event even in the case no event in the cryogenic detector module has occurred. Therefore, if a common two-sided time window of $2 - 10$ ms around an event in the detector modules is used [56,87,88], the real dead time is much higher. If the entire veto rate of typically $\sim 5\,s^{-1}$ were used, the dead time fraction would be

$$20\,\mathrm{ms} \cdot 5 s^{-1} = 10\%,$$

which, while being an upper limit, is substantial. This detail alone demonstrates the need for appropriate selections in the veto data. It will be shown later that the distribution of muon-coincident events is statistically always after a muon event without the distribution leaking to negative time differences, therefore a one-sided time window is sufficient.

4

Veto operation: monitoring and diagnostics

The main topic in this chapter is the analysis of the veto detector data from the extensive background data campaign Run32 of CRESST-II, primarily to address the long term performance and gain a better understanding of the characteristics of the muon veto system. In the course of this chapter, the veto data from the two previous runs 30 and 31 are also examined, although they have a greatly reduced amount of available data compared to Run32.

For an efficient and reproducible muon identification and the subsequent rejection of muon-induced signals in the detector crystals, it is necessary to achieve stable operating conditions in the experiment, both for cryogenic detectors and the muon veto. The latter issue is the topic of this section. Various aspects are covered, which can be used for stability monitoring and/or for diagnostics in further analyses, especially when viewed in the context of muon identification.

In previous measuring campaigns the muon veto data was not used in the final analysis for the published data, and it was just noted that the veto system was installed prior to Run30. Due to the high number of other background signals in the dark matter search region, the data from the veto was not needed, as the sensitivity was not limited by muon induced background events. Nevertheless, the veto data of Run30 and Run31 are considered retrospectively here, and will be compared to previous work [87, 102] in the following chapters. In this chapter the focus is on reliability of the veto data, especially the stability of the veto system. The order is to analyze chronologically newest to oldest, i.e. first Run32, then Run31 and Run30.

	net hours	gross hours	%	time frame
Run30	3289.0	5344.8	61.5	2007
Run31	2029.5	2635.2	77.0	2008
Run32	11587.7	14686.2	78.9	2009-2011

Table 4.1: Overview of the total (gross) recorded amount of data for each campaign and the corresponding total time. Note the improvement of experiment background run availability over time. Gross times include the phases for calibration. The data used for muon analysis is noted in the respective chapters.

Monitoring and diagnostics parameters

Monitoring the stability of the veto detector is very important. The crucial issue mainly is the influence small variations could have on the measured muon rate and identification

quality, which due to the quite small number of muons (few per hour) is hard to identify and quantify.

This chapter lists a number of diagnostics parameters and issues which are useful for monitoring the veto detector to identify possible problems. These parameters, discussed in this chapter, are:

- event rate in each single panel over time (sec. 4.1)
- the ratio of the sum signal divided by the single channel pulse height (sec. 4.2)
- pathological events and their abundance (section 4.4)
- signals with a multiplicity of zero (sec. 4.6)
- signals with a multiplicity of one, also called single-hit events (sec. 4.8)

Depending on the problem at hand, these parameters can be used to monitor different types of issues, which will be explained in the respective sections. As will be seen, the event rate in general is in the range of several signals per second. Judging from this number, it is clear that the vast majority of the recorded signals does not stem from muons, which are expected in numbers of several signals per hour. Therefore a suppression of background signals of about three orders of magnitude has to be achieved.

4.1 Rate evolution in panels

The first monitoring parameter naturally is the panel event rate. In the following section, an overview of all panels is given, highlighting similarities and differences between the Runs 32, 31 and 30 as well as between the panels themselves.

Event rates in Run32

In fig. 4.1 the overall event rate is shown averaged over one hour for the whole duration of Run32. Additionally in the appendix the signal rates for all panels are shown in fig. B.1a and fig. B.1b. Most panels display a relatively constant rate of recorded events, but some exhibit strongly varying features, which are discussed in this section. Some examples of these panels are shown in fig. 4.2 together with stable examples. Especially the horizontal panels (fig. 4.2a and top two rows in fig. B.1a), show continuous increases and decreases, respectively, over the whole Run32. This could be due to a drift in the gain of the photomultipliers or a drift in

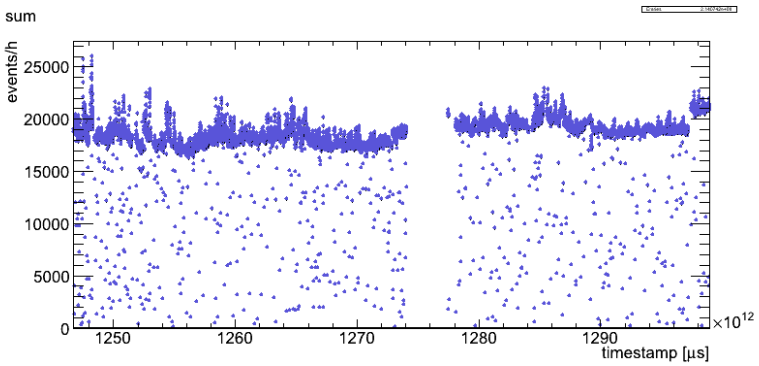

Figure 4.1: Run32: Events per hour. No drastic shifts are visible except for a short period at the end of the run, in contrast to several single panel rates (see section B).

the electronics. If the pulse heights are shifted from slightly above or below the panel trigger, the rate in the panel increases or decreases, respectively. This scenario is plausible, because the digital readout suppression was introduced to lessen the impact of the exponential tail of low energy (background or noise) signals, which most scintillator panels show.

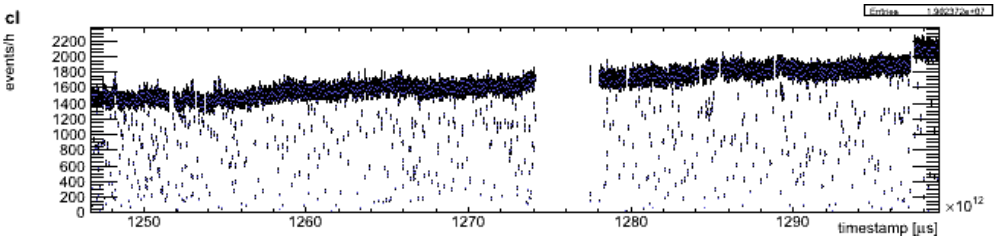

(a) #1-ceiling left

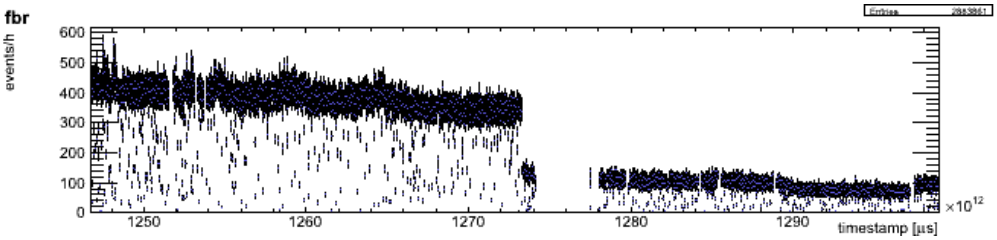

(b) #7-front bottom right

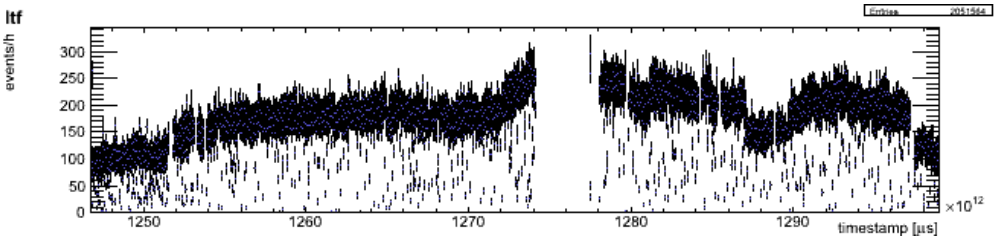

(c) #18-left top far

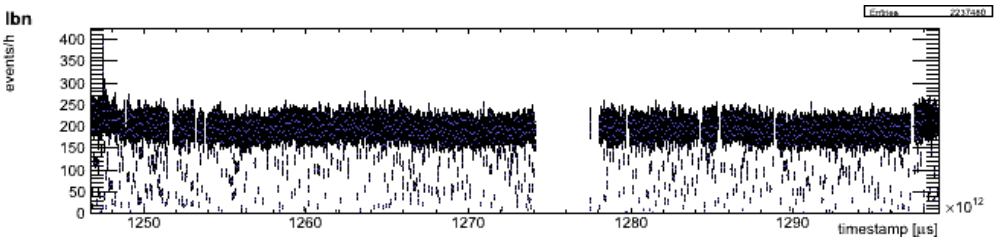

(d) #19-left bottom near

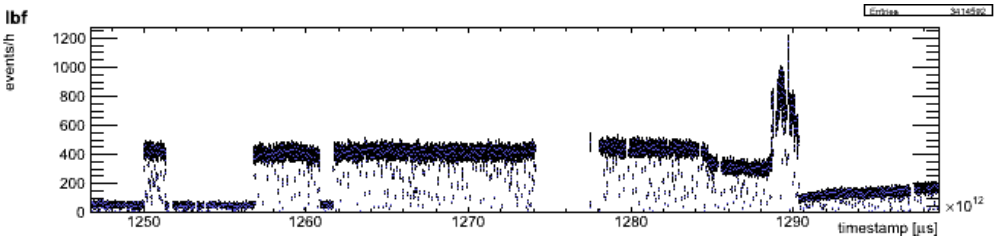

(e) #20-left bottom far

Figure 4.2: Signal rates in selected panels in Run32. The #7, #18 and #20 panels are discussed in the text.

In several detectors, one or even more clear discontinuities (steps) in the rate can be seen, most notably in #20-*left bottom far* (fig. 4.2e), #7-*front bottom right* (fig. 4.2b), and to a lesser extent #18-*left top far* (fig. 4.2c). This obviously cannot be explained by any particle physics process, but must be due to problems in the data acquisition. Reasons for this behavior could be that the electronics does not give constant signal heights or erratic electric contacts are present in the cabling. There are strong hints for the latter [103] and

steps are being taken to avoid this in future runs. In this and the following chapter the effect of these discontinuities on the muon selection will be discussed.

In fig. 4.3 the example of the #7 (*front bottom right*) panel is used to indicate a correlation between the rate step and the pulse height spectrum. For the two phases separated by this step the respective normalized spectra are shown on the left. The red curve, representing the measurement period mostly after the pause, has a steeper low energy contribution, implying a relatively larger contribution of this part to the overall spectrum. Also the peak is shifted to a higher pulse height, and the structure is broader, meaning a worsened energy resolution. The short "spikes", which can be seen in fig. B.1a and B.1b in the rates of several detectors, are most commonly connected to the start of a new file, and also especially after work in or around the Faraday cage, which can influence the conditions of the electronics. It should be noted that the diagram is binned in hours, and most data points in the excess regions are in the first bins only, i.e. at the beginning of the data recording period. In the following sections and chapters it will be shown that most of these instances do not influence the effective operation of the veto detector with respect to muon identification and vetoing power.

However, the graphs containing the simple event rates are a good and in particular a quick indicator for controlling the behavior of each of the panels. This is especially important since the muon rate at the LNGS is –within the CRESST setup– too small to be used to identify possible problems within a reasonable time. The sum and panel trigger rates are more then 10^3 times higher and thus a much faster way to detect changes in operation conditions.

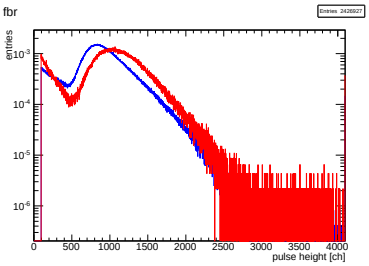

(a) Normalized pulse height spectra before and after the step in the rate. Notice the variation in the spectra (blue: before, red: after drop) with a steeper low energy contribution and the peak shifted towards higher energies after the pause.

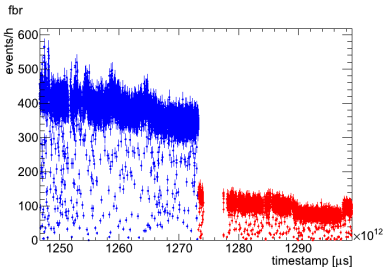

(b) Signal rate. A drastic drop in the event rate by ~75% occured shortly before the pause for the neutron calibration, concurring with the spectral shift in the figure on the left.

Figure 4.3: Run32: panel #7-*front bottom right* panel.

Event rates in Run31

The CRESST Run31 was a three-month data taking campaign from August until December 2008. This was an intermediate run mainly used for testing before the long term Run32. Due to the nature of the run and the relatively short time of just over 100 gross days, the results were not published. Nevertheless, the muon veto data is used here. We follow the same steps as above and show the characteristics and behavior of the veto system.

The general veto DAQ settings were retained for all files included in this analysis and are the same as in the later Run32, see Tables 3.4 and 3.5. At the beginning of Run31, a few data files with corrupted veto timestamps were recorded, amounting in total to about 20% of the run (see table 4.1). These files consequently have not been used in the analysis. Fig. 4.4 displays the overall event rate in Run31.

Rate comparison Run31 vs Run32

Although comparing the signal rates for Run32 and Run31 with regard to long-term trends is difficult due to the much shorter measuring time, some remarks can be made. In general, the average panel rates, agree to about 10%, with no clear trend which detectors have a

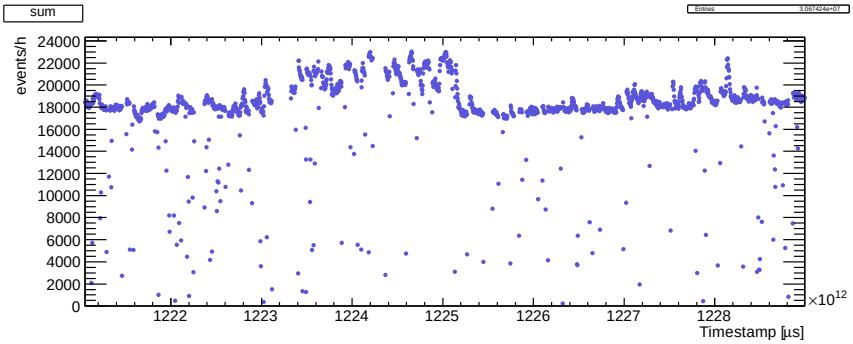

Figure 4.4: Run31: Events per hour. The rate is at a similar level as in Run32. Most panels exhibit the bump in the second quarter of the Run.

higher or lower panel signal rate. The drift is similar e.g. in panel #8 (*front bottom left*) as shown in figs. B.1a and B.1b compared with figs. B.2a and B.2b. In this panel, the increase is by nearly 100% during Run32, but already noticeable in the short time of Run31, too. Also notable is the behavior of the problematic panel #20 (*left bottom far*). This detector, which shows multiple rate jumps in Run32, has had a similar step-like rate reduction for a while during the first quarter of Run31. It seems there are at least two operating conditions for this panel/photomultiplier combination, because the behavior is very similar, with slightly higher rate during Run32 and periods of erratic behavior at the end of that run.

The panel #18 (*left top far*), rather unstable during Run32, has only several thousand signals overall recorded during Run31, which is much less than expected considering the difference in measurement periods. This is due to a large contribution from near-threshold events, as will be shown in the discussion about a potentially damaged panel (section 5.6).

Event rates in Run30

The CRESST Run30 was the first longer measuring phase where the newly installed muon veto was taking data. Overall, the amount of data collected during Run30 spans over more than seven months from March to November 2007, with an net duration of 3300 hours. Some settings were still experimental, rendering some data unusable for analysis. A notable example in the recorded veto data is that in one data file the trigger on all single channels was switched on with a very low threshold value at only 1/4 of the standard sum trigger value. While this measurement period was only about five minutes, the approximate data acquisition dead time fraction in the three detector modules was less then 5%. With these settings, though, the veto trigger rate is higher than usual by about a factor of 100, leading to an excess amount of veto data, which is very difficult to handle. A more important argument against changing these settings, if the thresholds are not increased, is that almost none of the additional events are due to muons. These data will therefore be ignored in the following. An overall trend is visible in figures 4.5 (sum) as well as B.3. The event rate in the whole veto system is decreasing over the time span of about six months. Each of the 20 panels has the same behavior except for the #20-*left bottom far* panel, which has long periods with almost no recorded signals, akin to the later runs. The trend of step-like decreasing rates also shows up in coincident events of multiplicities higher than one, as can be seen in fig. 4.6. A particle physics origin is unlikely, since no process can plausibly explain the combination of contributions to high multiplicities on the one hand and step-like changes in the rate on the other hand.

Further analysis with respect to the deposited energies in the panels reveals that the rate decline only happens in lower energy events. In figure 4.7 the black and red time series show that the lower parts of the sum channel spectrum are responsible for the rate drift seen in each channel. The lowest energy events with sum < 500 are mainly responsible for this drift, while the event rate for sum > 1000 is relatively constant. This strongly hints at a gain drift in the photomultipliers. An explanation by a light contamination is unlikely, since this would imply that all 20 photomultiplier would have seen too much light simultaneously,

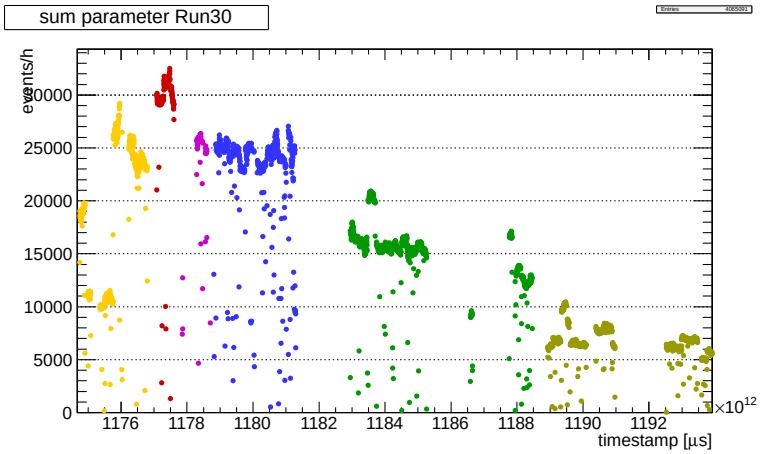

Figure 4.5: Run30: event rate. An overlying almost linear decrease in the event rate during the whole about three months of the run can be seen, ranging from $\sim 9s^{-1}$ at the beginning to $\sim 1.5\,\mathrm{s}^{-1}$ at the end of Run30. The analysis in [102] likely covered one of the two periods with few interruptions either around timestamp $1.180 \cdot 10^{15}\mu s$ or $1.184 \cdot 10^{15}\mu s$, both consisting of about 25 days of data taking.

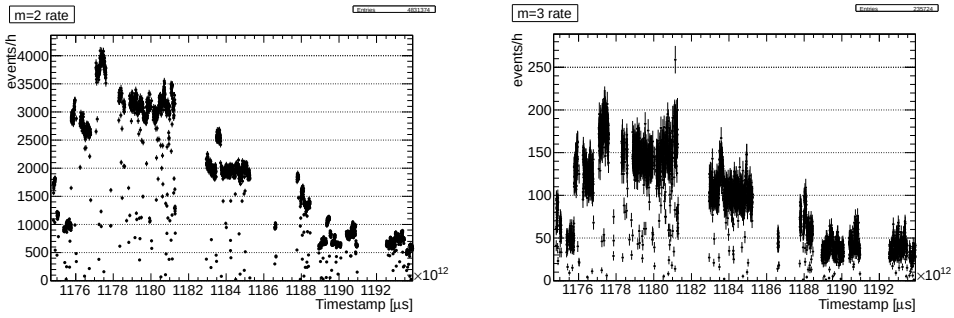

(a) multiplicity 2 **(b)** multiplicity 3

Figure 4.6: Event rates [h^{-1}] for the sum channel during Run30 for multiplicity 2 and 3 events. The behavior is similar also for $m \geq 4$. A particle physics origin therefore is unlikely (see text). The overall rate is again dominated by $m = 1$ events, which can be seen by comparing the scales of the above pictures with fig. 4.5.

which is highly improbable.

Conclusion Run30 rates

Run30 provides a longer data sample compared to Run31. It was recorded with a different electronics setup (sum signal building) than in Run32, nevertheless some common features are noticable. The most noteworthy is that the #20-*left bottom far* panel experiences the same feature of sudden rate variations (decrease/increase) as in the two later runs. In Run32 this went along with a low energy shift in the spectrum, so it is likely that the photomultiplier gain was set too low.

4.2 Ratio sum/panel

A second possible parameter for the stability monitoring is ratio of sum signal to the pulse height in a single detector ($m = 1$), in other words $\frac{\mathrm{ph}(sum\ event)}{\mathrm{ph}(panel\ event)}$. This ratio should remain constant throughout data taking. Changes in the ratio would indicate a modified response

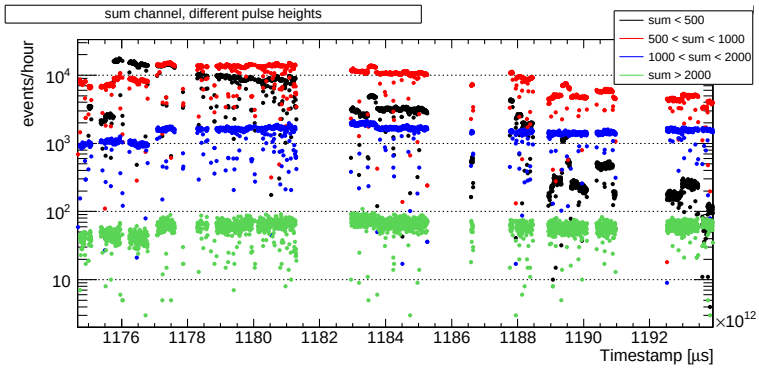

Figure 4.7: Sum channel rate during Run30 for different pulse height regions: $sum < 500$, $500 < sum < 1000$, $1000 < sum < 2000$, $sum > 2000$. This shows that the behavior mentioned in the text and shown in figures 4.5 and B.3 happens almost only in the low energy regime. If only the maximum sum entries (sum ≥ 4095) are used, this rate does not show any exceptional variations.

of either the summation module, a variation of the gate (time window) allowing coincident signals to be added up, or a problem in the signal chain from the photomultiplier to the DAQ. Ideally e.g. a gain change in the PMT should have the same effect on the panel signal and the sum signal. Due to the coincidence gate for integrating in the sum module, this may not be true in all cases, because the signal acquisition is different for single channels and the sum. In general the sum/panel ratio is less than one, with typical values around 0.5, but there are some exceptions mentioned in the text. It will be seen that the sum/panel parameter can be an indicator for a big shift of the single panel spectrum.

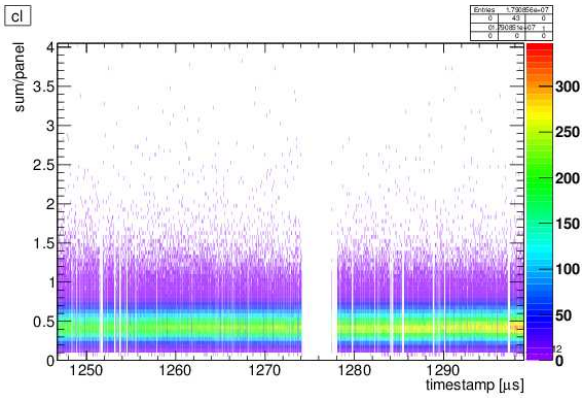

Figure 4.8: The sum/panel ratio in panel #1-*ceiling left* remains constant during Run32, while the rate (color index) in the panel increases continuously throughout the run, as shown in fig. 4.2a.

Run32

In fig. 4.8, the sum/panel ratio is depicted for one ceiling panel during Run32, which is exemplary for most other panels. The color code in the ordinate gives an indication for the event rate. However, in fig. 4.9a the pulse height of the #12-*right bottom near* panel decreases in relation to the sum. Since the trend is unique for this panel, there is a problem in the this channel. The corresponding spectrum plotted in a time series (fig. 4.9b) points out that the $m = 1$ peak, which is the easiest accessible value, starts to drift to smaller pulse heights.
Even in those panels with sudden variations of the event rate, in the new operating state after a rate discontinuity the ratio sum/panel remains constant, see e.g. the #18-*left top*

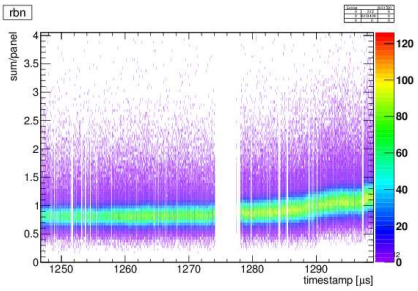

(a) Sum/panel ratio. The ratio is constant at ~0.8 until the pause with increasing rate, as exemplified by the larger width of the green band. The increasing slope after the pause to > 1 indicates a modified response of the panel's DAQ.

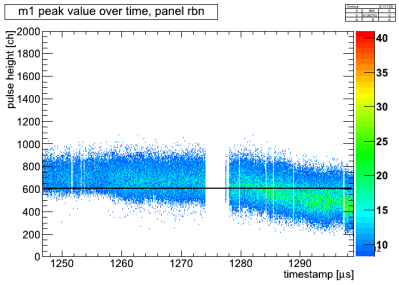

(b) The sum/panel drift shown on the left is caused by spectral shift of the single hit peak in the #12-*right bottom near* panel.

Figure 4.9: Run32: panel #12-*right bottom near*.

far panel. This behavior is shown in fig. 4.10a. This means that if a single panel shows a step in the rate over time, and the sum/panel ratio remains constant, there must be a small spectral shift near the panel trigger threshold, where the influence of a shift on the single detector trigger rate is large.

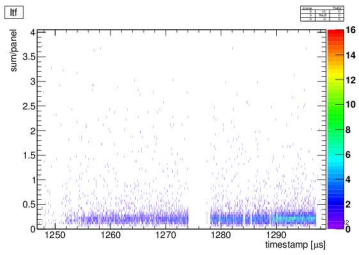

(a) left top far

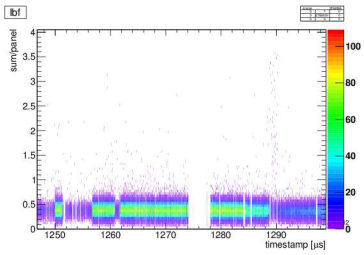

(b) left bottom far

Figure 4.10: Run32: in contrast to fig. 4.9a the sum/panel ratio remains constant even for the two panels with strongly varying signal rates: #18-*left top far* has a continously varying low signal rate, while its neighboring panel below #20-*left bottom far* exhibits several steps in the rate.

Run31

During Run31 the sum/panel ratio parameter remains at an almost constant level. Only in some short intervals, where the width of this parameter is increased, the average level is lower. This is shown in fig. 4.12b, which again uses the #20-*left bottom far* panel as an example on the right, but shows the #17-*left top near* instead of #18-*left top far* panel, since the latter only has very few events recorded. Almost all panels except for one have a ratio of sum/panel of less than one as described above. The #12-*right bottom near* panel has an inverted ratio (sum>panel), which is continuously at a value of three. This is related to the fact that the m=1 peak in the corresponding pulse height spectrum is barely visible and shifted towards lower energies, and the number of high energy signals is very small, likely because of a too small voltage of the PMT. The mentioned panel #12-*right bottom near*, which exhibits an increase of the sum/panel ratio towards the end of Run32, is depicted in fig. 4.13a for the Run31 data. Since the live time of this run is very short, a comparative statement is difficult to make, but from the profile in the graph, only a slight increase is visible.

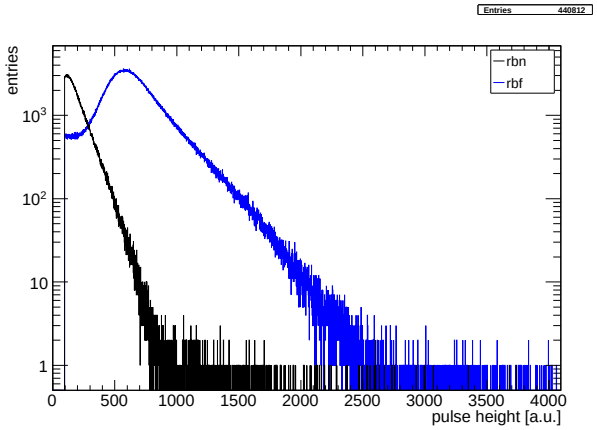

Figure 4.11: Run31: spectra of the panels #11-*right bottom far* (blue) and #12-*right bottom near* (black). The former shows the m=1 peak, while for the latter the whole spectrum is shifted towards lower pulse heights, and there is only a hint of the peak visible by the slope of the spectrum towards lower pulse heights.

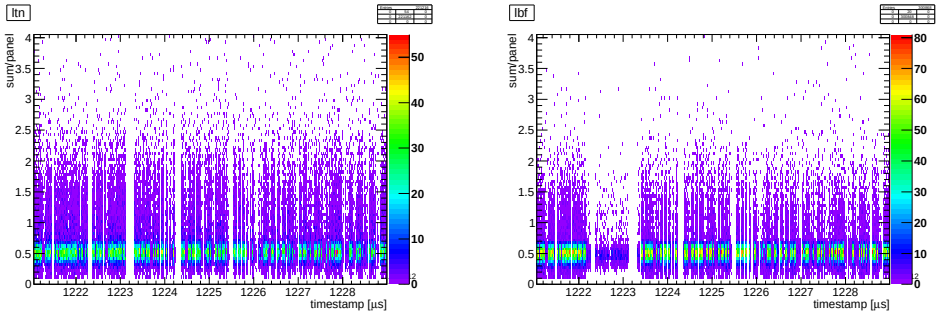

(a) #17-left top near

(b) #20-left bottom far

Figure 4.12: Run31: the sum/panel ratio remains constant. #17-*left top near* (left) has a low event rate which varies continously, while #20-*left bottom far* (right), the neighboring panel below, is the only panel which experiences a large rate drop, recovering after a short period, while the sum/panel ratio remains constant throughout.

Run30

During Run30, although the signal rate shows large variations, the ratio is at a very constant level with a few exceptions (figs. 4.13b,4.14). As an example, the #12-*right bottom near* panel is mentioned again, where at the beginning, around timestamp $1.176 \cdot 10^{15} \mu s$, when the signal rate is not yet at its maximum, the ratio is slightly lower than during the rest of the run. This indicates that there were, for this short period, different running conditions. As previously the sum/panel ratio is less than one, consistent with the other runs. In figures 4.13b and 4.14b, and also partially in the low-rate panel #18-*left top far*, fig. 4.14a, the spectral shift brought up in section 4.1 can be seen in the smaller sum/panel ratio near the beginning of the run.

Conclusion sum/panel

The sum/panel parameter can be used as a long term indicator for single panels, as in Run32 for panel #12-*right bottom near* (fig. 4.9a), where the pulse height in the $m = 1$ peak shifted towards lower energies at the end of the run. If the sum parameter remains unchanged for single hit events, but the $m = 1$ pulse height varies, changes e.g. in the photomultiplier gain can be detected with the sum/panel parameter. For the two panels, which had major

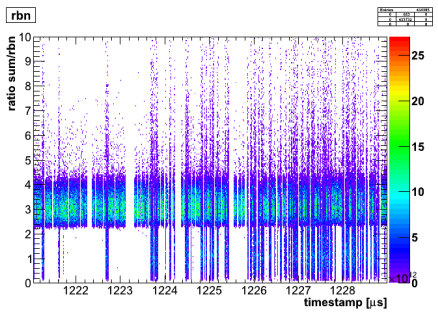

(a) Run31: In contrast to fig. 4.9a, the ratio remains constant to within ∼3%, but the time scale of Run31 is rather short. Nevertheless a behavior as in Run32 (cf. fig. 4.9a) should already be visible on this scale.

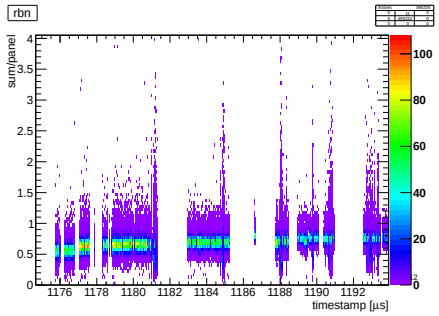

(b) Run30: The ratio remains almost constant even in the phases with very high signal rates, and shows only a slight increase in over the course of the run with reducing signal rate (color scale). Only at the beginning the ratio is about 10% lower than in later periods.

Figure 4.13: Ratio sum/panel for #12-*right bottom near*.

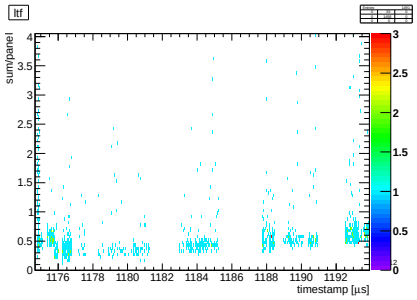

(a) #18-left top far

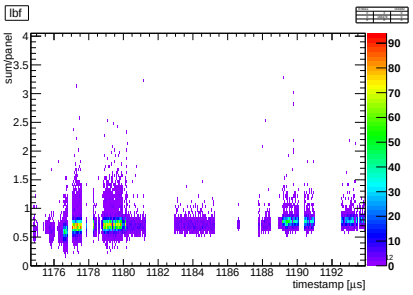

(b) #20-left bottom far

Figure 4.14: The sum/panel ratio remains rather constant during Run30, even though the rate in the detector varies strongly in both cases: #18-*left top far* (left) has a low event rate which varies continously, while #20-*left bottom far* (right), the neighboring panel below, exhibits several large steps in the event rate.

rate jumps in Run32, #18-*left top far*, fig. 4.10a, and #20-*left bottom far*, fig. 4.10b, the parameter is insensitive to the rate changes, so the spectrum does not change, which is a first hint that the rate steps are not automatically a serious problem.

4.3 Multiplicity histograms

In this section, as a short interlude, the multiplicity distributions of Runs 32, 31 and 30 are shown to emphasize the observations made so far: veto events, where only one photomultiplier triggered, dominate the distribution, and events with signals in two ($m = 2$) and three ($m = 3$) panels are overabundant: the whole $m = 2$ class alone would contribute a "muon" rate of about $0.25\,\mathrm{s}^{-1}$. Thus the high multiplicity events remain, which still contribute almost 10^4 signals or $\sim 1\,\mathrm{h}^{-1}$. If one assumes that higher order events are predominantly induced by muons and statistically distributed events in multiple panels, a power law is simple assumption for the distribution, which has also been used slightly modified in the literature [104]. All distributions in the histograms of figs. 4.16, 4.17 and 4.18 can be fitted with a power law function for $m \geq 5$, achieving similarly good results, as listed in table 4.2.

$$f(m) = am^b \qquad \text{with multiplicity m and b} \approx \text{-5.2 ...-5.6, see tab 4.2} \qquad (4.1)$$

The exponent is almost the same for all three runs to within the uncertainties for $m \geq 5$, which indicates that higher order events behave in the same way since the beginning of

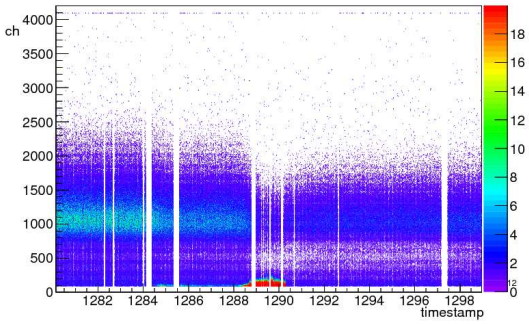

Figure 4.15: Signal pulse height variation during a part of Run32 in #20-*left bottom far*. The rate (color scale) is enhanced strongly for a short period around $1.290 \cdot 10^9$ s. The spectrum (y axis) shows that this increase occurs only close to threshold and dominates the spectrum. The mean pulse height outside this phase is constant.

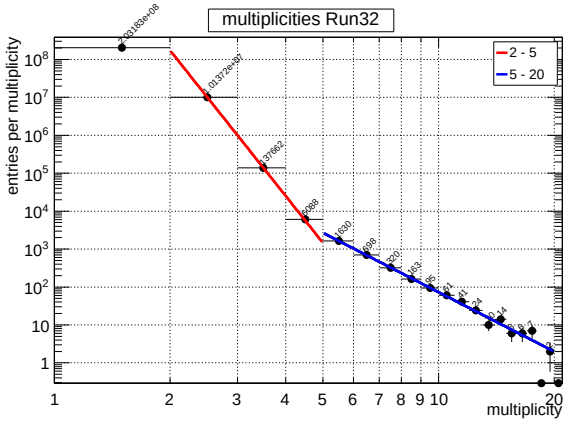

Figure 4.16: Run32: multiplicity distribution of veto events. The red line indicates the slope for $m < 5$, while the blue slope is drawn for high-multiplicity events. The highest entry has a multiplicity of 19. The $m = 1$ bin nicely shows that these events contribute more than 90% of all veto events. The $m = 0$ events are not included here.

$m \geq 5$	slope parameter	error
Run32	-5.202	0.084
Run31	-5.483	0.315
Run30	-5.567	0.136

Table 4.2: Fit parameters for power law fit.

Run30 and are not affected by the –mostly low energy– instabilities shown previously. An explanation for this is that muon-induced showers yield the same distribution of such high multiplicity events in the given veto geometry, which indicates that these high multiplicity events are in fact created by muons. The harder slope at $m < 4$ cannot be due to random coincidences, which are expected at a much smaller rate (section 4.10). The discussion of the likely origin of the $m = 1$ signals can be found in section 4.8. Thus it is necessary to select the muons in the $m \leq 4$ data.

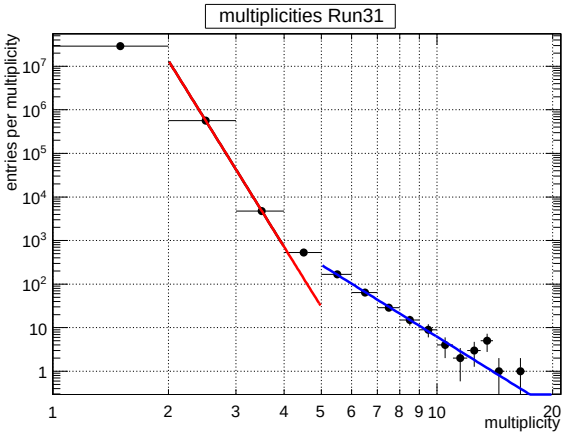

Figure 4.17: Run31: multiplicity distribution with power law fits. The total event number is $\sim 3 \cdot 10^7$ with a maximum multiplicity of 16. At $m = 13$ a slight excess seems to exist, but this can not regarded as significant due to the low number of events. Each of these individual events contains at least one very small panel contributions, thereby artificially increasing the multiplicity.

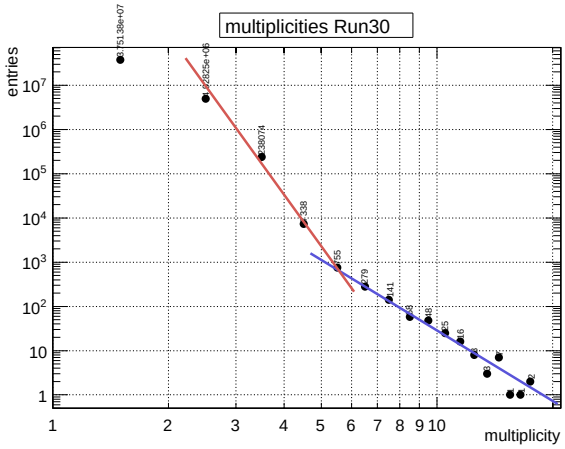

Figure 4.18: Run30: multiplicity distribution. The total event number is $\sim 4.3 \cdot 10^7$ with a maximum multiplicity of 17. At $m \leq 4$ the slope is much steeper then for $m \geq 5$. The higher multiplicity slope is similar to Run32 and Run31. A difference to Run32 and Run31 is that the contributions from the $m \leq 3$ veto events are larger here, which is due to the large low-energy event rates as discussed in section 4.1.

4.4 Pathological signals

As an additional viable parameter to monitor the veto operation, the lowest spectral range of sum events just above the trigger threshold was considered, because muons are not expected to be found in this region. The pulse height spectrum has a peak near the trigger cutoff, shown in figure 4.19 exemplary for Run32. This results from the increasing trigger efficiency, which contrasts the exponential low energy background/noise tail. One would expect that for events at very small sum values, the contributions from the panels also have a rather small pulse heights and, more importantly, also should not have high multiplicities.

There are clearly pathological events, which have large energy depositions in several panels, rather high multiplicity, but on the other hand a very low sum value. Table 4.3 lists a few notable events of this type for the different runs. The single panel spectra of these events here also feature isolated, prominent maxima in a range of up to 1000 channels, with a quickly diminishing number of entries to higher pulse heights. This could be an indication

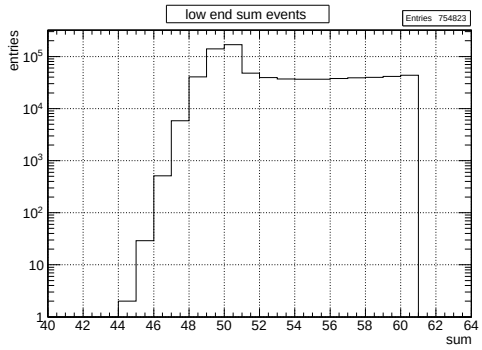

Figure 4.19: Low energy part of the sum spectrum in Run32.
The steep, exponential decrease towards the lower end is due to an increasing trigger efficiency and steeply rising spectrum from noise and background close to threshold. The single panel spectra of these sum ≤ 60 events here also have the peak at ~800 ch.

run	multiplicity	sum par	sum of panels
Run30	4	45	765
	4	57	518
Run31	8	49	13417
	6	55	11400
	4	44	8781
	4	45	6690
	4	45	4829
	4	52	5426
	4	55	7337
	4	58	5842
Run32	4	50	709
	4	50	642
	4	59	751

Table 4.3: Pathological events with sum $\ll \sum_{panels}$ and $m \geq 4$. The highest multiplicities found are 4 for Run30 and Run32, and 8 for Run31. In Run31, the sum of the single panel pulse heights is far off the sum value, while by contrast the Run30 and Run32 events have plausibly small values.

for an electronic problem, for example a defect analog addition module. In Run31, the highest multiplicity for such events is 8, while in Run30 and Run32 events with a maximum multiplicity of 4 are found.

While in Run31 the high multiplicity events also have very high panel contributions, adding easily up to values much larger than the overflow value, the same cannot be said about Run30 and Run32. The latter present low energy sum events with also low energy panel contribution, as one would expect. Overall this is a clear indication that at least the low energy Run31 data is to be used with caution.

Conclusion low energy pathological signals

There are a lot of near threshold events, i.e. with a very small sum value. At the sum values ≥ 60 ch considered here, only events with very small panel pulse heights are expected, which should in general be near or below the panel trigger (readout suppression). Thus it is surprising to find such veto events with multiplicities of up to eight. Since this happened in all runs, it indicates that the integration time for the sum signal was probably too long. Most of these pathological signals occurred during Run31, where the low-sum events also had very large panel trigger contributions, as noted in table 4.3, while the problem was reduced in Run32. It can be concluded that checking the multiplicities of such events can be

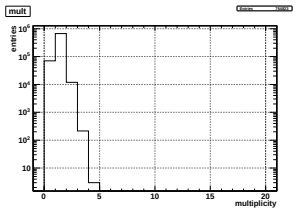

(a) Run32. As noted in table 4.3, in Run32 these events typically consist of panel trigger signals just above the readout suppression, and therefore are unlikely to be muons.

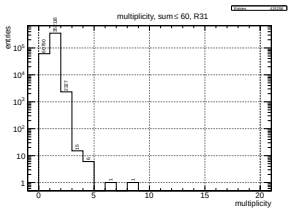

(b) Multiplicity histogram for low energy sum events in Run31. There are several entries with $m > 4$, see also table 4.3. This is a clear indication that the the sum signal was not constructed reliably.

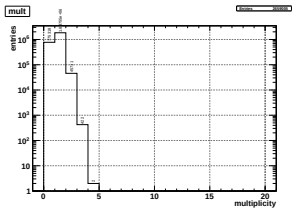

(c) Multiplicity histogram for low energy sum events in Run30.

Figure 4.20: Multiplicity histogram for low energy sum events with sum ≤ 60. Such signals with a high multiplicity are dangerous to reject, as they could still be muons considering the multiple signal structure.

a useful parameter for remote testing against wrong or drifting settings in the electronics. The result of this section is again that the sum signal is not a good selection parameter to accept or reject veto events as muons. High-multiplicity events with a small sum signal should not be discarded automatically, as they could be muons judging from event structure.

4.5 Undetectable muon candidate events

The discussion in this section is concerned with event classes of undetectable muon candidate signals, which will be defined and used to estimate the amount of muons, which are lost due to the nature of the event types, and also referred to in the $m = 0$ discussion in section 4.6. Several possibilities for such events can be constructed. The top (ceiling) panels both have a semi-circular cut-out as listed in table 3.1 to allow for the cryostat cold finger feed-through. Therefore, viewing from a zenith position, the net area not covered by plastic scintillator is

$$A_{hole} = \pi r_{hole}^2 = \pi \cdot (0.295m)^2 = 0.2734m^2. \tag{4.2}$$

Relative to the whole top area, this results in the percentage of area not covered from above

$$\frac{A_{hole}}{A_{top,total}} = \frac{\pi \cdot (0.295m)^2}{2 \cdot 0.80 \cdot 1.616m^2} = 10.6\%. \tag{4.3}$$

This number can be used to get an estimate on how many muons are not detectable due to the geometry. If a muon produces secondary particles in a shower, these particles could produce signals in several panels with pulse heights depending on the secondary energies. The estimation of the number of muons which cannot be either clearly detected or identified at all is divided into cases according to the veto construction setup. The categories are listed here for the purpose of the estimate only, since they are experimentally not distinguishable.

- **case A: stopped muons**. This case has two subcategories.

  A1: passed hole – stopped Muons passing through the opening in the veto setup and stopping within the lead/copper shield, not creating any measured signal at all in the plastic scintillator, but possibly in the cryodetector modules either directly or via secondary particles.

  A2: passed one panel – stopped Muons, which can cross one panel of the veto system and then are stopped inside the shielding.

- **case B: passed hole**. Muons passing through the hole, subsequently through the lead/copper shielding and then exiting this volume by crossing through one panel (or inverse path). As in case A, these particles are required to come from the zenith angles $0 \ldots 85$ degrees due to the geometry.

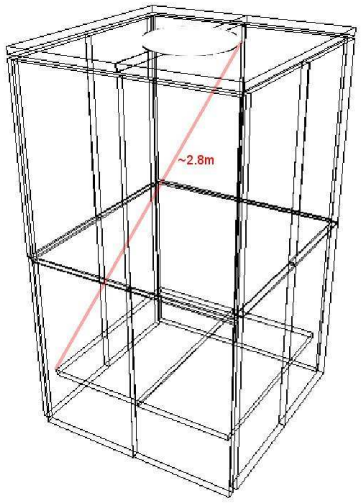

Figure 4.21: The maximum path length for a particle inside the muon veto without passing through a scintillator panel is ~2.8 m.

- **case X:** the cases remain, where a particle crosses one or more panels, but the signal is too small to reach the sum trigger. Such events can intrinsically not be measured and therefore are not considered here.

Cases **A2** and **B** are multiplicity 1 events, if the panel trigger condition is fulfilled, and are practically indistinguishable in the veto data, but have different physical origin. In practice, due to the geometry one expects more muons passing through the hole and exiting the veto detector while being detected in exactly one panel as opposed to case A2. For the stopped muons it is helpful to calculate the longest possible path for a particle inside the veto box (see fig. 4.21). This calculation is used to estimate the relative amount of stopped muons *within* the CRESST muon veto using the depth-intensity relation [60] for the muon flux. The overall longest path is simply the diagonal of the inner veto box. Here the total height of two panels on top of each other is reduced by ~22 cm due to the recessed floor panels. see fig. 4.21.

$$\text{path} = \sqrt{(2 \cdot 1.35 - 0.22)^2 + (2 \cdot 0.80)^2 + 1.616^2}\,\text{m} = 3.36\,\text{m}, \tag{4.4}$$

The longest path through the hole and subsequently exactly one panel is 0.5 m shorter.

Depth-intensity relation

The muon flux the Gran Sasso laboratory site is calculated [68, 71, 74] with the depth-intensity relation $I(h)$ at depth h in the following parametrization[27] with the corresponding fit parameters

$$I_\mu(h) = A \left(\frac{h_0}{h}\right)^\alpha e^{-\frac{h}{h_0}} \tag{4.5}$$

where

$$\begin{aligned} \text{A} &\approx 2 \cdot 10^{-6}\,\text{cm}^{-2}\text{s}^{-1}\text{sr}^{-1} \\ h_0 &\approx 970 - 1150\,\text{hg/cm}^2 \\ \alpha &\approx 1.1 \end{aligned}$$

As only a relative number is desired, the uncertainties are neglected for the estimation.

[27] The two-parameter Fréjus function of [104] yields the same results.

Shielding material stopping power

The fraction of stopped muons can be estimated using measured muon rates at the LNGS and calculating the "stopping power" for the longest possible path for muons travelling through the setup. Since the massive copper and lead shielding provide most of the stopping power within the veto box, for a first guess we first use only a toy model setup of the shielding to calculate the longest particle path. Using the technical drawings, it can be deduced that a cube with edge length 1.30 m is sufficient for the purpose, which results in a path length of $\sqrt{3 \cdot 1.30^2}\,\mathrm{m} = 2.25\,\mathrm{m}$. We further assume the whole shielding to consist of lead with density $11.4\,\mathrm{g}cm^{-3}$ compared to copper with density $8.94\ \mathrm{g}cm^{-3}$ [6]. Therefore the total mass is overestimated by ∼27% in the copper part, which leads to a more conservative (higher) estimate of stopped muons. The cold box is also assumed to consist of solid material. As rock overburden the value ∼ 3800 m.w.e. [79] is used. With eq. 4.5, the "muon attenuation factor" can be calculated by the flux reduction within the particle path. A shielding with 2.25 m of lead equals an additional 10 m.w.e. of overburden, which is only slightly increased, if the maximum path of eq. 4.4 is used. A more realistic number is ∼4 m.w.e. for the path through the experiment, when the different material densities are included.

Inserting these values into equation 4.5, the loss in intensity and therefore the percentage of muons stopped within the experiment's veto can be estimated to ∼0.2 %. While about two in 1000 muons being stopped inside the setup seems high, it has to be kept in mind, that this is the upper limit for the longest path of a muon in the experiment, and the flux reduction is calculated for the vertical intensity only. Because the flux of muons through the cryostat hole according to eq. 4.3 amounts to only ∼ 10.6% of the total flux, the result is further reduced by a factor of 10. Stopped muons are expected to deposit a large amount of energy[28] in the material, and therefore should also create signals in several scintillator panels or in multiple detector modules. Since the events discussed in this section also contain $m = 0$ signals, which are low energetic, those events can therefore be neglected.

4.6 Multiplicity 0 event discussion

It has been mentioned already that the data acquisition also allows for veto events to be recorded with a multiplicity of zero, when only the sum signal is recorded. As will be shown later in section 4.10, the overall number of random coincidence events, calculated for all veto events, is very small and already for twofold coincidences negligible for practical purposes. It is unlikely that such events could be constructed from an accidental combination of sub-readout panel events that only contribute to the sum trigger signal, so they must be of some correlated origin. From the description it is therefore clear that such $m = 0$ events

run	$m = 0$	relative %	mean rate (h^{-1})
R30	835775	1.9	254
R31	988073	3.2	487
R32	607065	0.3	52

Table 4.4: Number and fraction of $m = 0$ events relative to all veto events. The rates are each at least one order of magnitude higher than the expected flux, so carrying $m = 0$ events as muon candidates is unreasonable.

should only happen for very low-energetic signals. The fractions of $m = 0$ events are listed in table 4.4 for each run. Due to the non-negligible number of $m = 0$ events and the basic possibility that they are due to muons, an analysis of this data is presented here, but the full $m = 0$ data set is not considered afterwards regarding muons for two reasons: a) no useful cut can be applied to the data and therefore no categorization as muons is possible, and b) in table 4.4 the fraction of such signals relative to the total number of recorded events in the muon veto is listed together with the run-averaged rate. In every run the number of $m = 0$ signals is at least an order of magnitude higher than the expected muon rate of a few per

[28] The average muon energy in the Gran Sasso underground laboratory is about 270 GeV [6].

hour. It is therefore not reasonable to consider these events as muon candidates, and they can be neglected as was explained in section 4.5.

Nevertheless, the $m = 0$ data can be useful for diagnostics. The described origins of these signals implies that by definition the events should be on the low end of the pulse height spectrum, and as such close to the threshold of sum trigger and also –indirectly– panel trigger. So any variation in near-threshold conditions should directly translate into a change of the event rates of this kind. By this means this event class is a good indicator for the stability of the whole veto.

Rates The rate of $m = 0$ events in Run32 is shown in fig. 4.22. After a relaxation period at the beginning starting from about 70/h, the number of these signals is rather constant at about one per minute. The constant line in the figure is drawn at 50/h as a guidance. For

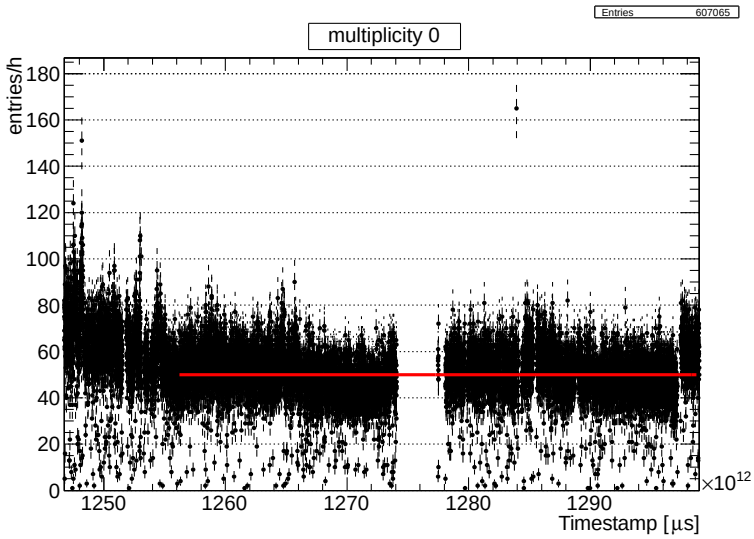

Figure 4.22: Run32: $m = 0$ events per hour.

Run31 and Run30, two illustrative examples are given in fig. 4.23, showing different issues of the $m = 0$. In Run31, as also noted in Table 4.4, the $m = 0$ fraction is about an order of magnitude larger than in Run32, and also within Run31 there are two distinct operating states. The Run30 $m = 0$ rate picture shows several short bursts of events, but otherwise for most of the run has only a very small level of such signals, much lower than in Run32. Since both pictures in fig. 4.23 display an erratic behavior of the $m = 0$ rate, they can be used as diagnostics parameter, but should be neglected for muon analysis, which is in agreement with sec. 4.5.

To take a closer look at the $m = 0$ event class, we use the spectra of these signals as the only accessible parameter apart from the event rate.

Run32 From fig. 4.24 it can be seen that the sum pulseheight spectrum extends to ~1400 ch, which is remarkably large for not recording a single panel trigger. To demonstrate that the amount of these signals is problematic, we arbitrarily use from the spectrum in fig. 4.24b only the tail with sum> 400 ch, which would require four panels below panel threshold to combine to a $m = 0$ event[29]. The rate of such events with about $0.5\,\mathrm{h}^{-1}$ would produce a sizable contribution to the muon flux.

Run31 The pulse height spectrum reflects the two rate levels in a double-peak structure compared to the Run32 spectrum, which can be seen by selecting the the high- and low-energy regions of the spectrum and observing the respective rate behavior (fig. 4.25). The

[29] If a sum/panel value of ~0.5 is assumed (sec.4.2), still two coincident panels below threshold would be needed.

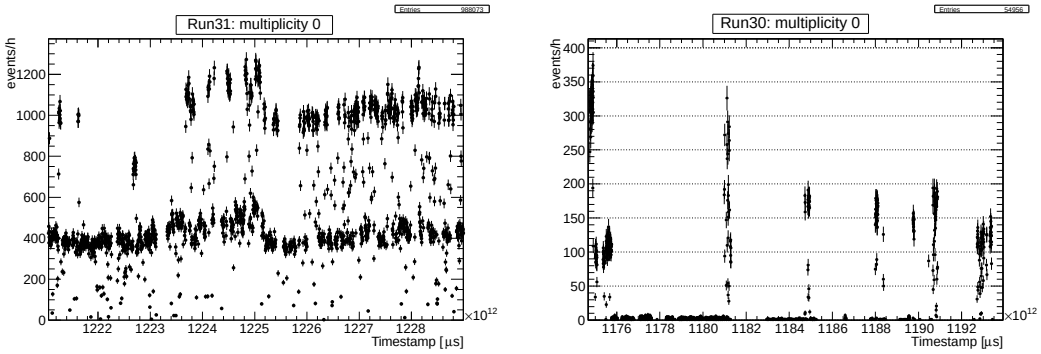

(a) Run31 **(b)** Run30

Figure 4.23: Run30 and Run31 $m = 0$ rates indicating stability problems.
Run31: There are two clearly different operating states of the veto, both of which have extremely high $m = 0$ event rates compared to Run32.
Run30: the periods with extremely high number of events correlate with high rate periods in panels, which indicates an electronic problem during these phases. The constant very low rate phases have less than ten events per hour.

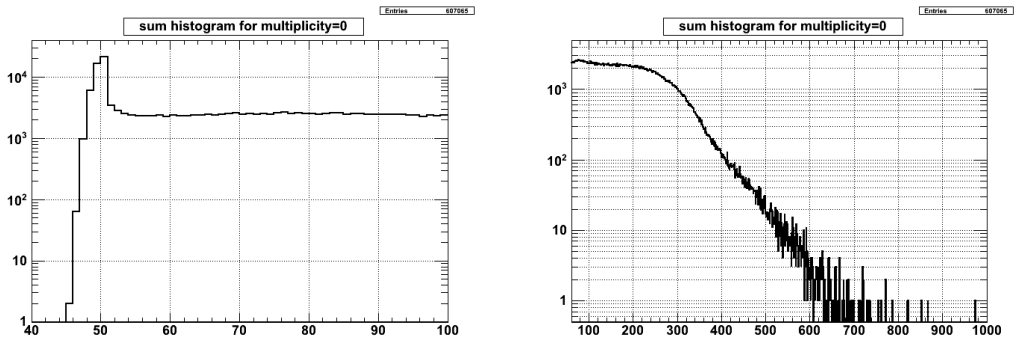

(a) low energy part **(b)** high energy part

Figure 4.24: Run32: spectra of multiplicity 0 veto events

exponential slope of the $m = 0$ spectrum extends up to ~2000 ch, much higher than in Run32, with almost 100 events even in the DAQ overflow (fig. 4.26a), which under normal circumstances cannot be explained without at least one panel signal. These events cannot be explained plausibly in a muon scenario, so it is very likely that these events are due to an unknown electronic problem.

Run30 In fig. 4.23b the $m = 0$ rate for Run30 is shown. The phases with high $m = 0$ numbers correlate with the event rates in the panels (figs. B.3, 4.7), as shown in fig. 4.27 with the pulse height shift, which indicates a general stability problem during the run. The high energy part is different from Run32 and Run31, a clear peak is visible with a maximum at $\lesssim 700$ ch. This spectral shape is typical for the single panel spectra. Also in Run30 the exponential slope extends up to ~2000 ch with very few events above.

Summary multiplicity 0 veto events

Concluding the discussion of multiplicity 0 events, these signals can be neglected as muon candidates, but the data from this event class can be helpful, especially since the fraction of those events is not small and varies a lot between the different runs. The $m = 0$ events are unusable for vetoing purpose, because due to their nature, no statement about single channels is possible. However, because they can in principle only occur for small signals

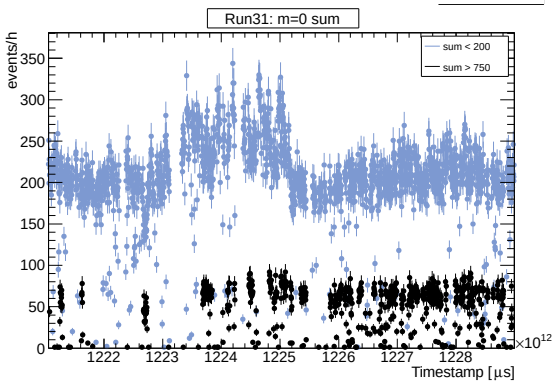

Figure 4.25: Run31 $m = 0$. In black (sum>750) the high-low rate bands can be seen, which is not the case for the low-energy blue/grey curve (sum<200).

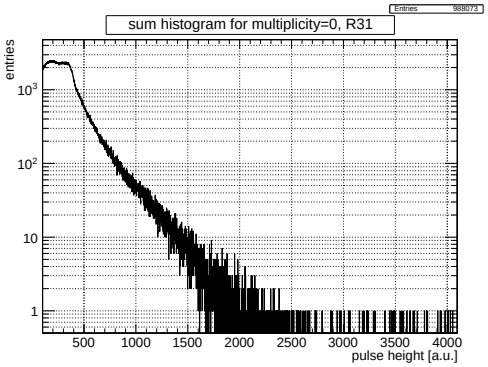

(a) Run31: $m = 0$ spectrum. Between 100 and 400 channels the spectrum can be fit with a combination of two gaussian distributions.

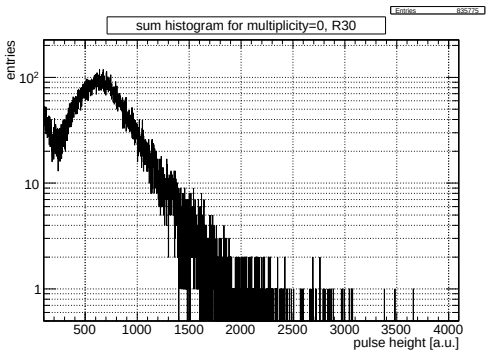

(b) Run30: $m = 0$ spectrum. Note the peak at a pulse height of ~700 ch, which a typical peak position in the $m = 1$ spectra.

Figure 4.26

close to the trigger or readout threshold, they are a good diagnostics or stability monitoring parameter to discover disturbances, possibly in combination with near-threshold multiplicity 1 events.

4.7 Monitoring: conclusion & outlook

In conclusion, it is clear that a better monitoring of the veto system is needed to avoid the irregularities and discontinuities in the trigger rate. Several steps have been taken already to identify the source of the rate variation problems [103]. For one, the connectors on the outside of the Faraday cage are very sensitive and require careful grounding. This was tested with a pulser at the setup in preparation of Run33. A second measure to avoid the problems is to switch on the triggers on each panel in Run33. While this will increase the overall trigger rate, it may be possible to achieve a faster identification of problems of the same kind as in Run32. In particular, the $m = 0$ problem can be avoided with this triggering scheme. On the other hand, especially low energy veto events close to trigger threshold can create high rates for $m = 1$ type events, and could also contribute to higher order events. These signals are typically not induced by muons and would wrongly inflate the actual number of muons.

The parameter sum/panel pulseheight for $m = 1$ events turns out to be a good indicator for changes in the behavior of single photomultipliers. With this parameter a shift of the spectrum relative to the sum can be detected in addition to the rate. Together with other indicators (low energy sum events and multiplicity 0 events), it can be helpful for future monitoring of the veto.

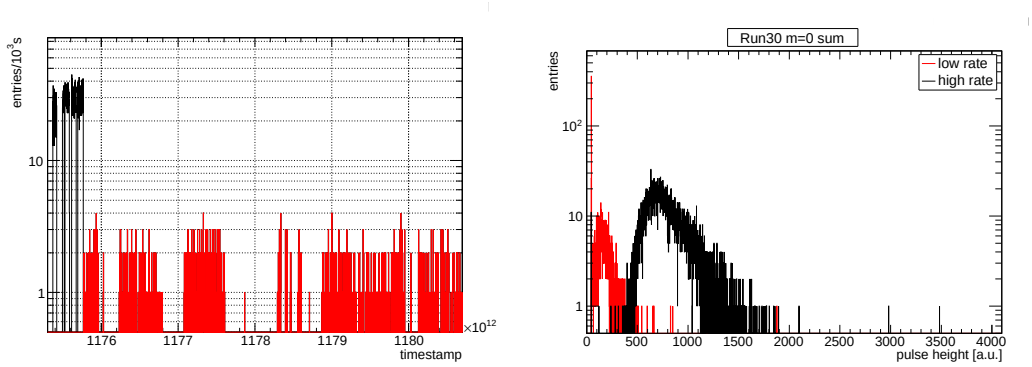

(a) rates **(b)** pulse height spectra

Figure 4.27: Run30: pulse height spectra (right) for two phases with low and high event rates (left). During the high rate phase (black), the spectrum is shifted towards higher pulse heights with a peak around channel 700 (see also fig. 4.26b). Only parts of the Run30 data were used for this figure.

Thus, for a quality monitoring of the veto system some suggestions and recommendations can be made. While a first glance with triggers activated on all available QDC channels, i.e. for all panels, did not generate an enormously large additional deadtime (∼5%) there is not much advantage. A practical downside however is, that working with this setup would increase the amount of data by about two orders of magnitude with basically no gain in muon identification potential, because only the low energy signals are enhanced. Continuing with the present setup has some advantages as well. With a simple check of the trigger rate and the sum/panel parameter, potential problems of the veto can be identified quickly. To this purpose, it may be worth lowering the readout suppression by a small amount, but this would require tests in order not to increase the amount of unnecessary data, as noted above. However, the next sections will show that the monitoring is mostly needed for control purposes, because the influence of trigger rate variations on the muon rate is an entirely different issue, which will be handled in the subsequent chapter.

4.8 Multiplicity 1 event discussion

It has been noted already that events with just a single panel signal are by far the most abundant in the veto data. In Runs 31 and 32 more than 95% of all recorded veto events are in this class (table 4.5). In this section it is argued that in reality only a small fraction of these events could be considered as potential muons, as also explained in section 4.5, but the major part can be explained by other origins. This is also the reason to open the discussion before the muon definition in chapter 5. The energy spectra of the photomultiplier signals are explored for the $m = 1$ veto events and a plausible explanation for the features in these spectra will be discussed.

	$m = 1$	$m \geq 2$	fraction (%)
Run30	37513756	5175002	86.2 (87.9)
Run31	29114639	571538	94.9 (98.1)
Run32	203183038	10284081	94.9 (95.2)

Table 4.5: Number of veto events with multiplicity 1 compared to the number of all veto events. In brackets are the fractions without including the multiplicity 0 events. It is noteworthy that the fraction of multiplicity >1 events is much larger in Run30. This can be due to a different sum signal generation.

4.8.1 Estimated fraction of muons with single panel event

In section 4.5 the longest possible path for particles crossing the muon veto was calculated. That section focused on muons which are stopped within the veto setup. Here, further estimates are given which limit the number of $m = 1$ events as muon candidates.

Geometry

As a first step in looking at the $m = 1$ event characteristics, the largest possible angles for muons or other particles entering the veto through the cryostat hole are estimated. For this purpose, we take the measures of the scintillator panels, neglecting their thickness and the PMT volume. In this approximation there cannot be $m = 1$ veto events in the ceiling panels except for particles stopped within the veto volume or particles with an entry zenith angle of 90°. The horizontal panels below the radon box are the obvious candidates for receiving most of the muons passing through the hole at the top of the experiment. In those panels, the number of high energy (muon-type) single-hit events should therefore be higher than in the others. For the ceiling panels one would expect no single-hit muons at all except for muons stopped inside the veto, which is only a small fraction (sec. 4.5). In all other cases at least one additional panel would measure a signal.

Only the signals with pulse heights in the DAQ overflow bin of 4095 ch are considered here. Since in the calibration the pulse height spectrum was adjusted in a way that the muon maximum was positioned at the center of the DAQ range (see section 3.2) at ~2000 ch, the maximum bin, which corresponds to an energy[30] of about 20 MeV, should result in a data sample with suppressed background. Most events with an overflow pulse height in one panel are from higher multiplicity ($m \geq 2$) events, as listed in table 4.6, and this class of events will be analyzed in chapter 5. For the lower side panels (the "bottom" panels), the zenith angles

	panel	m=1 & PH≥ 4095			$m \geq 1$
		Run32	Run31	Run30	Run32
1	cl	340	8	22	1445
2	cr	26	12	21	1849
3	fl	74	164	25	765
4	fr	16	7	13	412
5	ftr	17	7	12	378
6	ftl	8	13	9	471
7	fbr	84	18	27	519
8	**fbl**	**227**	**32**	**52**	1379
9	rtf	52	4	12	761
10	rtn	32	1	11	1349
11	**rbf**	**185**	**22**	**16**	821
12	**rbn**	**39**	**0**	**34**	312
13	btl	48	10	18	1228
14	btr	2	0	6	515
15	bbl	58	13	30	307
16	**bbr**	**45**	**7**	**16**	289
17	ltn	32	4	4	608
18	ltf	22	0	3	935
19	lbn	66	10	17	531
20	lbf	108	13	25	619
	overall	1481	345	373	
	[h^{-1}]	0.13	0.17	0.11	

Table 4.6: $m = 1$ events with pulse heights ≥ 4095. The **bold-faced** entries indicate where an excess would be expected. In the right column all multiplicities are included for Run32. Also the floor panels do not show more events than the ceiling panels.

accessible for a $m = 1$ muon are about $[24° \ldots 39°]$, as visualized in fig. 4.28. Muons passing

[30] The mean energy loss for minimum ionizing particles passing through matter is ~1.9 MeV cm^{-1}.

a panel in such angles means a larger mean energy deposition, as the path in scintillator material is increased by $\frac{5\text{cm}}{\sin\Theta}$, where Θ is the angle from zenith. For the upper side panels, the allowed angles from zenith is larger with a range of $[39°\ldots 85°]$. Provided a large number of events and no background contamination, the upper and lower panels should therefore have a different muon pulse height spectrum.

Bottom side panels The sketch of the veto setup (fig. 4.28) illustrates that the horizontal floor panels are recessed with respect to the lower side panels by ~20 cm, which additionally allows single hit muons with an inclined muon track in the scintillator. Therefore there should be a larger number of high energy signals in the vertical bottom panels compared to the vertical top panels. Additionally, a small excess of muons could be expected in the "right" side panels in direction towards L'Aquila, where there is the least rock overburden. These panels, as well as the neighboring ones, are marked in **bold** in table 4.6, but no excess can be determined.

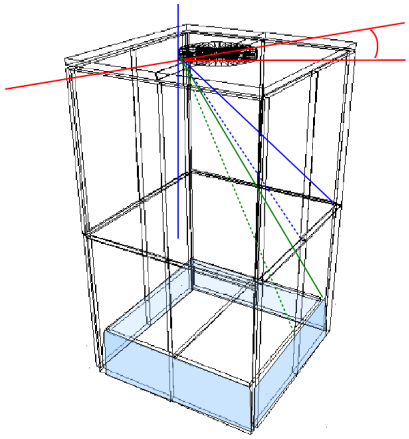

Figure 4.28: Sketch of the CRESST muon veto as used in oxRop. The hole area corresponds to $\approx 10.6\%$ of the top panels. Note that the two floor panels are recessed by ~20 cm (shaded areas). The lines indicate the minimum (red) zenith angles for muons entering through the hole, and the allowed angles for single hits in upper (blue) and lower (green) side panels.

panel	Run32	Run31	Run30	panel	Run32	Run31	Run30
ftr	0.20	0.38	0.12	fbr	3.60	1.74	2.44
ftl	0.19	0.40	0.08	fbl	2.63	1.94	1.49
rtf	3.25	4.46	3.05	rbf	2.77	2.61	0.97
rtn	3.17	5.36	2.07	rbn	1.04	1.21	0.34
btl	2.22	0.89	0.72	bbl	3.70	3.54	0.39
btr	0.24	0.46	0.04	bbr	2.34	1.86	0.52
ltn	0.48	0.33	0.29	lbn	2.27	1.03	0.42
ltf	0.75	0.00	0.01	lbf	3.06	0.57	0.96

Table 4.7: Run-averaged rates in $[\text{h}^{-1}]$ of events with pulse heights above the muon peak (as shown in fig. 3.8) in each respective panel for $m = 1$. Only the vertical panels are listed, left: top side panels; right: bottom side panels.

High energy tail In fig. 4.29, the $m = 1$ pulse height spectra of the high energy tail above ~2000 ch (as in fig. 3.8) are shown for all panels. Table 4.7 lists the rates from these muon candidates averaged over the runs. Both the variation and the level of the rates are evidence that the majority of these signals are not caused by muons.

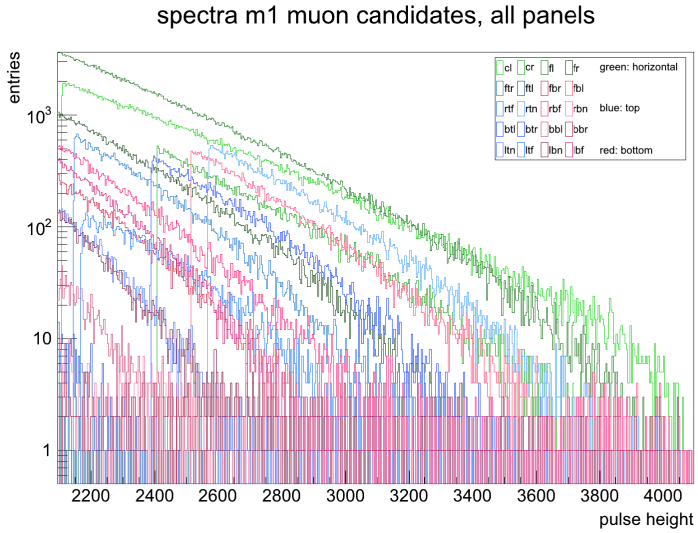

Figure 4.29: $m = 1$ pulse height spectra for all panels. The graphs include only high-energy entries above the muon peak value in the respective panel (as in fig. 3.8). Note the large amount of entries per panel, which is too large to be muons.

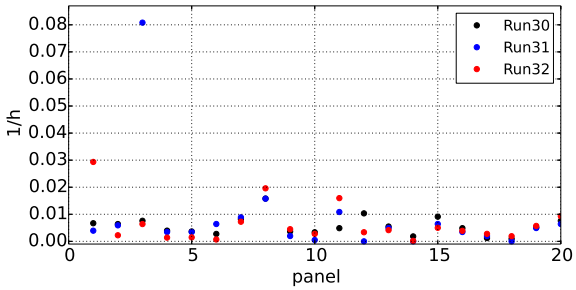

Figure 4.30: $m = 1$ overflow event rats in the single panels, as in table 4.6. The visualization shows the same trends for the panels between the runs, indicating similar operation characteristics. The first four entries are the horizontal panels (ceiling/floor).

4.8.2 Pulse height spectrum $m = 1$

A typical $m = 1$ pulse height spectrum is shown in figure 4.31 for the example of the peak in the #11-*right bottom far* panel. With the exception of one panel (#18-*left top far*), all spectra have a distinct maximum at pulse heights less than 1000 ch. This peak in the $m = 1$ spectra is not due to the QDC pedestal, but points to a physical origin. Figure 4.32 shows that the peak positions follow a relatively even distribution with values in the range of 600-1000 channels, which translates to energies of about 2.5 to 5 MeV, assuming a linear energy response of scintillator and photomultipliers. Such high energy single hit signals cannot be easily produced in plastic scintillators other than by minimum ionizing particles such as muons or from radioactivity. The highest gamma energy from natural radioactivity originates from the ^{208}Tl beta decay in the Thorium series with a decay gamma energy of 2.615 MeV. In this regime, photons mainly interact via Compton effect, which has a maximum allowed electron energy of 2.38 MeV. Higher energies could of course still come from nuclear transitions, but could not explain the abundance of events, as there is no plausible source in plastic scintillator materials. These materials, such as the Bicron BC408 (Polyvinyl toluene), mainly consist of hydrocarbon compounds with the addition of so-called "organic fluors" providing the fluorescence properties. Such materials can be produced with

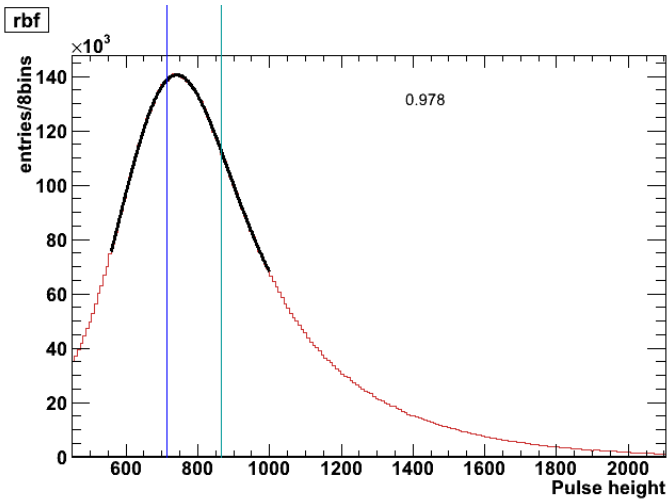

Figure 4.31: Pulse height spectrum including a combined fit of two Gaussian distributions around the $m = 1$ maximum to determine peak position and approximate energy resolution. For the pictured spectrum of the #11-*right bottom far* panel, the maximum is at about 750 ch with an energy resolution of 22% (1σ).

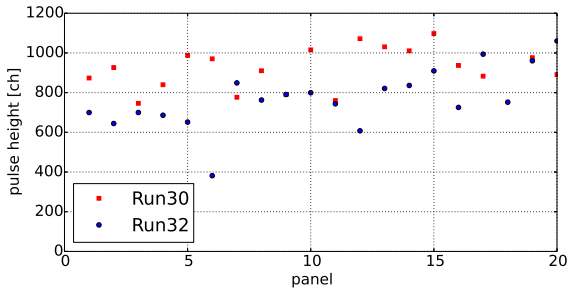

Figure 4.32: Fit of Gaussian distributions to the $m = 1$ peaks for all panels during Run32 and Run30. The peak position is shifted towards lower energies from Run30 to Run32 with a slightly smaller variation, but the general trend is similar. One panel in Run30 is omitted, where no peak could be determined.

a good radiopurity, and therefore no significant amount of radioactivity is to be expected from the scintillator itself. In addition the material consists of light elements, mainly C, H and O, which do not provide suitable decay energies.

In the photomultiplier tubes, however, electronics, dynodes and metal structure and especially the glass can contain radioactive trace elements. The glass windows of PMTs are known to have radioactive contaminations[31]. In the ET9900B photomultiplier used in the CRESST veto panels the window is made of borosilicate glass [97], which can contain several percent of alkali oxides. The manufacturer provides the fraction of several contaminants in the material, which are listed in table 4.8. In the following an evaluation is conducted if these contaminations can be responsible for the large single-panel event rates. If in fact radioactive decays in the glass, which produce mainly γ with MeV energies, are responsible for the $m = 1$ peak, geometry suggests that the gamma interaction with a large energy deposition occurs in vicinity of the photomultiplier. Therefore the measured energy could be expected as a broadened Compton edge. The energy resolution of a plastic scintillator as well as a photomultiplier is not good, so the expectation can only be to detect a maximum in the pulse height spectrum centering roughly at the Compton edge, with a very broad (Gaussian) distribution.

[31] Hence the efforts of e.g. the DAMA and XENON collaborations to acquire low radioactivity photomultipliers.

element	content	specific activity	activity
K	300 ppm	35 Bq/g	0.37 Bq
Th	250 ppb	4080 Bq/g	0.04 Bq
U	100 ppb	25280 Bq/g	0.08-0.16 Bq

Table 4.8: Trace elements in the ET9900B photomultiplier window, taken from the manufacturer's data sheet. The right column lists the estimated activity from these contaminations per photomultiplier, details see text. A systematic uncertainty of about 20% is realistic, as the mass of the glass part is estimated. In the last line the specific activity of natural Uranium in secular equilibrium is given.

The total mass of one 29 mm ET9900B photomultiplier is taken from the data sheet as typically 55 g (see Appendix A.1). Since the mass fractions of the borosilicate glass components and the photocathode are not known, both of which include most of the K, Th and U traces, it is estimated that about 2/3 to 3/4 of the PMT mass consists of glass. For an estimate of the signal rate due to radioactivity 35 g glass per PMT is assumed. The potassium, thorium and uranium contamination levels reported by the manufacturer are listed in tab. 4.8. Using the specific activities, the activity from decays of those elements adds up to almost 0.5 Bq per PMT, as shown in the last column in the table. Since the photomultipliers are inserted into the veto panels and the PMT glass is fully surrounded by scintillating material, the only non-scintillating area is the path through the dynodes, so a decay particle leaving the glass can be expected to create a light signal in the plastic scintillator in at least 50% of all cases.

In summary, when only the event rates provided by radioactive decays are considered, it is plausible with this estimate that the elements listed in table 4.8 can account for the bulk of the signals in the $m = 1$ peak, which are the main contribution to the overall signal rate of $\sim 5\,\mathrm{s}^{-1}$ in the veto detector.

Conclusion m1 events

The discussion of the $m = 1$ events has shown that only a fraction of less than 10% of all muons should have a signal in only one scintillator panel. However, in the data this event class is dominant and provides more than 90% of all recorded events. A plausible explanation for the large amount of single hit events has been found. Gamma decays from Uranium, Thorium and especially Potassium are the leading candidates for creating the large amount of $m = 1$ events. These signals are created near the photomultipliers, and therefore more light is collected and the pulse height is larger than for a gamma event from the environment. Since there is no possibility to distinguish signals caused by radioactivity and by muons, it is thus doubtful that the $m = 1$ events can be used for a muon safe analysis.

4.9 Conclusions for stability

At the beginning of this chapter, the importance of a reliable muon veto system was stressed. For three separate data taking runs, the data from the CRESST muon veto was analyzed. Several parameters could be identified, which are suitable for monitoring the standard operating conditions of the veto detector at short time scales. This is important, since the muon flux in the setup is only a few muons per hour, which does not allow a fast monitoring.

It was shown that there were unstable periods in all three runs, which should be monitored, as different categories of problematic events occured. These can be separated into two main classes: a) pathological signals (section 4.4) and b) an overabundance of $m = 0$ signals (section 4.6). The latter issue is resolved in Run33 by triggering and recording all panel signals. As a result, the amount of recorded data is several times larger, because at low pulse heights the full QDC pedestal is then registered as well. The additional data therefore contain only events, which are not caused by muons, but are useful to monitor the operating conditions of the veto.

4.10 Random panel-panel coincidence rate

An upper limit of the random coincidence rates is estimated in this section. For the calculation the measured $m = 2$ events of Run32 are used, with the signal rates averaged over the respective data files. In general, the random or accidental coincidence rate of m detectors can be calculated from the single rates in each detector [105, 106]

$$R_{rc} = 2\tau \prod_{i=2}^{m} R_i, \tag{4.6}$$

where τ is the resolving time window of the coincidence circuit for accepting i events as coincident and R_i are the single detector rates. In the CRESST muon veto system, τ is given by the QDC gate of ~500 ns length and a two-fold panel-panel coincidence ($m = 2$) with a typical maximum single panel rate of $1\,\mathrm{s}^{-1}$, the resulting random coincidence rate is

$$R_{r,ij} \sim 10^{-6}\, s^{-1} \tag{4.7}$$

which amounts to less than one event per 10 days. In the following, only two-fold coincidences are taken into account, because the probability for higher-order random coincidences is negligible. For the the real setup with 20 scintillator panels in the muon veto system, each having a different signal rate, all panel possible $\binom{20}{2} = 190$ combinations have to be considered, which leads to an upper limit on the random coincidence rate of $1.9 \cdot 10^{-4}\mathrm{s}^{-1}$ or about one per two hours. This is only an estimated upper limit, because in reality the trigger rates in each panel can vary by up to two orders of magnitude. When these rates are factored in for all possible panel combinations as listed in table 4.9 and visualized in fig. 4.33, the total random coincidence rate is

$$R_{rc} \approx 1.3 \cdot 10^{-5}\, s^{-1}, \tag{4.8}$$

which equals about one random coincident event per day between any two panels compared to the $m = 2$ rate of about $0.25\,\mathrm{s}^{-1}$. Accidental coincidences between two or more panels are therefore negligible compared to the rate of actual two-fold veto events.

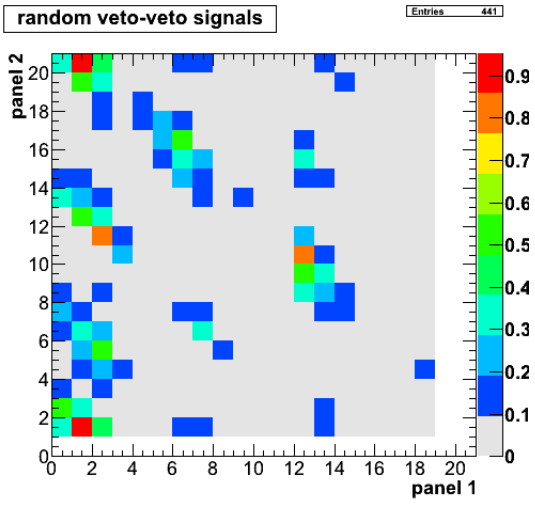

Figure 4.33: Graphical normalized representation of the random coincidence rates of all possible combinations listed in table 4.9. The horizontal ceiling/floor panels are numbers 1-4.

	cl	cr	fl	fr	ftr	ftl	rtf	rtn	btl	btr	ltn	ltf	fbr	fbl	rbf	rbn	bbl	bbr	lbn	lbf
cl	3.763	5.277	1.765	0.283	0.559	1.074	2.121	0.983	0.183	0.450	0.230	0.325	3.195	1.164	0.741	0.154	0.174	0.253	0.389	
cr		9.532	3.164	0.508	0.996	1.951	3.764	1.757	0.335	0.800	0.404	0.618	5.572	2.097	1.290	0.278	0.311	0.454	0.671	
fl			4.431	0.711	1.396	2.727	5.279	2.460	0.468	1.121	0.569	0.863	7.824	2.931	1.812	0.389	0.436	0.635	0.954	
fr				0.237	0.467	0.904	1.762	0.819	0.155	0.376	0.190	0.286	2.617	0.975	0.608	0.129	0.145	0.212	0.320	
ftr					0.075	0.145	0.282	0.131	0.025	0.060	0.030	0.046	0.418	0.157	0.097	0.021	0.023	0.034	0.051	
ftl						0.284	0.557	0.259	0.049	0.119	0.060	0.089	0.829	0.308	0.193	0.041	0.046	0.067	0.101	
rtf							1.076	0.502	0.096	0.228	0.116	0.179	1.589	0.599	0.368	0.080	0.089	0.130	0.193	
rtn								0.981	0.184	0.448	0.229	0.327	3.177	1.163	0.736	0.154	0.174	0.252	0.387	
btl									0.086	0.208	0.106	0.156	1.465	0.542	0.339	0.072	0.081	0.118	0.179	
btr										0.039	0.020	0.031	0.270	0.103	0.063	0.014	0.015	0.022	0.033	
ltn											0.048	0.072	0.667	0.247	0.156	0.033	0.037	0.054	0.082	
ltf												0.034	0.346	0.125	0.080	0.017	0.019	0.027	0.044	
fbr													0.451	0.189	0.106	0.025	0.027	0.041	0.057	
fbl														1.727	1.121	0.228	0.261	0.375	0.582	
rbf															0.400	0.086	0.096	0.140	0.210	
rbn																0.053	0.060	0.087	0.137	
bbl																	0.013	0.019	0.028	
bbr																		0.021	0.032	
lbn																			0.046	
lbf																				

Table 4.9: Random panel-panel veto event rates for all possible combinations in units of $10^{-7}\,\mathrm{s}^{-1}$. The overall random rate for a gate length of 500ns is $1.3 \cdot 10^{-5}\,\mathrm{s}^{-1}$.

5

Muon definition and rates

This chapter lists the procedures in detail to identify signals in the veto data originating from muons. To this end, at first the expectation for the muon rate within the CRESST muon veto setup is estimated. As shown in the previous sections the rates of single panel events ($m = 1$) and zero panel trigger events ($m = 0$) are too high to include only muons. As explained in the preceding chapter, only a small fraction of these event classes is caused by muons.

The main focus in this chapter therefore is on signals with a multiplicity of at least two. Of those events, the cases $m = 2$ and $m = 3$ will be treated with the most care, since they are the most abundant and since such signals are preferred by geometry and for plausibility reasons. For these event classes, a multi-level discrimination depending on multiplicity and pulse height is introduced for the muon identification process.

Important definitions

This work emphasises the positive identification of muons to the best achievable ability. Trying to maximize the number of identified muons, on the other hand, would include a rather large amount of signals falsely identified as muons. While then the obvious advantage is missing as few muons as possible, the implications are twofold. For one, the dead time increases, possibly to undesired levels, which will be discussed later. The second issue is that in the dark matter search data, one would like to identify muon induced signals. Referencing too large a data sample with lots of falsely muon-tagged signals only weakens the experimental results.
In the following therefore the distinction is made between

- **muon safe:** detect muons with a high efficiency while rejecting background signals of different origin as much as possible. In other words this means to safely identify and select muons with a high probability. The resulting selection consists only of muons.

- **veto safe:** include as many veto events as possible, thus have the highest likelihood for *including* a muon in the muon candidate sample. This stands for the possibility to safely veto signals in the detector modules. All muons are (also) included in this selection.

This distinction is important for the calculation of the muon detection. Up to this point, there was no differentiation in definition between signals in the veto detector, which are due to muons, and events due to any other effect. As a reminder, the general *veto events* consist of a number m of panel trigger signals, which give the multiplicity of the event.

For muon candidate signals, a procedure to calculate panel specific pulse height thresholds will be introduced in this chapter that define a pulse height (energy) level, above which a veto event can be classified as a muon. These events are called *muon events* or *muon candidates*.

5.1 Expected muon rate

For a calculation of the expected muon rate in CRESST, the directional flux of muons at the LNGS site is needed. The MACRO [68, 69], LVD [71] and BOREXINO [107] experiments have measured the muon flux in Hall C and Hall A, respectively, over many years. All of these published data sets are in very good overall agreement with the depth-intensity relation of surface muons propagating through the mountain overburden to the LNGS site. MACRO, in addition, has also published the directional data, from which an approximate (inverted) relief of the Gran Sasso massif can be reconstructed as shown in fig. 5.1. This

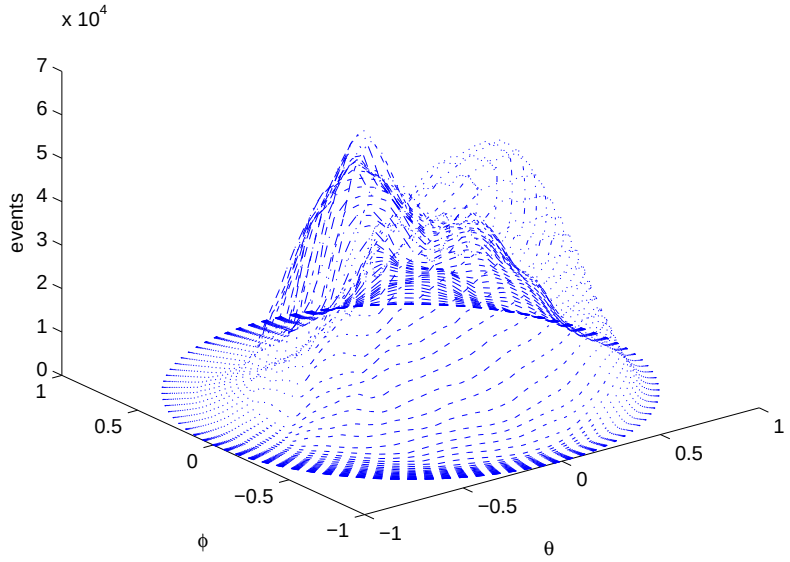

Figure 5.1: The Gran Sasso mountain overburden above the LNGS in muon flux representation, calculated from MACRO muon intensities [68, 108].

data set, provided in a processed form by L. Pandola / M. Knapp [109], is used here to calculate the expected muon rate within the CRESST experiment's veto structure from the measured and published flux.

The MACRO experiment measured the muon flux for the full hemisphere and provided the data with a resolution of four degrees in azimuthal angle and 2.25 degrees in zenith direction [68]. Since the spatial and angular resolution with scintillator panels of a size of about $1m^2$ is limited, these resolutions are sufficient.

Effective coverage area

As a first step for calculation of the expected muon rate and later also the veto efficiency, the effective area which is covered by the veto system needs to be calculated.

In the following, we assume that a possible muon detection can only occur, if a muon would pass through the cuboid representing the muon veto (see fig. 4.21), therefore requiring a pass through the experimental space in vicinity to the cold box. In general then a two-fold coincidence hit pattern in two panels is expected, if the muon is not passing through the hole on top of the cold box or not stopped within the lead/copper shield or the cold box with the detector modules. One simplification with this assumption comes from the given geometry of the setup, because there is a possibility for muons to pass through the lower side panels and only hit one of these panels (see fig. 4.28), since the floor panels are not aligned to the bottom of the side panels.

Gaps There are two further minor items, which are presented for the sake of completeness, but subsequently neglected. During the installation of the side panels, due to the safety of the construction it was not possible to avoid a gap (slit) of about 2–3 mm between the top and bottom panels in addition to the sheet covering the panels which has a thickness of 0.7 mm. Muons passing through these gaps and being missed can realistically only be a problem for muons crossing perfectly parallel to the edge into the cuboid containing the shielding and detector volume, which is negligible because the allowed opening angle would be at most about 3° for muons entering the cuboid in such a way. The remaining case of muons passing completely through two gaps would require zenith angles of $(90 \pm 0.1)^\circ$ and therefore is highly unlikely. All these mentioned cases contribute mainly to lost multiple-hit muons and result in a slightly enhanced $m = 1$ and $m = 0$ rate. With the tabulated MACRO data, one can estimate the additional muons for $m = 1$ to a fraction of about $10^{-6} - 10^{-5}$ of all muons.

A rather obvious area which cannot be fully covered are the photomultipliers, which are integrated into the scintillator material. The PMT diameter is smaller than the scintillator thickness, leaving about 10 mm on either side, and the plastic scintillator surface is covered with reflecting material, so it is safe to neglect possible light losses due to particle hits in the PMT housing. Signals may lose in pulse height due to a shorter path through the material, but the geometry suggests that such events should also have a multiplicity of higher than one, therefore increasing the chance of a detection as a muon. From table 3.1 one can be see that there are three different shapes of the 20 plastic scintillator panels. The top (ceiling) panels each have a semicircular cut-out to allow for the cryostat cold finger to reach the detector module space, the cold box. The top plane consists of the panel area and the hole, and is visible to all muons. Each of the side walls consists of four panels of equal size, and at most two walls are visible to a muon at the same time. Using all available measures, we get

$$\begin{aligned} A_{hole} &= 0.273\, m^2 \\ A_{top} &= 2.586\, m^2 \\ A_{side} &= 4.158\, m^2 \end{aligned} \tag{5.1}$$

for the areas of the top and side panels as well as the whole in the top plane.

The resulting effective area A_{eff} is then calculated by integrating over the azimuth Φ and zenith Θ angles with the weight of each angle given by the normalized data from MACRO, therefore projecting the veto cuboid in the direction of an incoming muon. The expected muon rate then can be calculated by multiplying the vertical muon intensity at the underground site with A_{eff}. Possible muons from the semi-sphere below a zenith angle of 90°, for which there are no data and the flux is almost zero compared to the flux from smaller zenith angles, are not considered. The total effective area of the box covered by scintillating material is then calculated to

$$A_{eff} = 5.11\, m^2. \tag{5.2}$$

With the vertical muon fluxes from LVD and MACRO of $1.2/(m^2 \cdot h)$, as used in eq. 4.5 (section 4.5), we can estimate the muon rate for the CRESST experiment:

$$\Phi_\mu(\text{CRESST}) \approx 6\, h^{-1}. \tag{5.3}$$

5.2 Multiplicity 2 and higher

Most of the muons, which create signals in the veto detector, are expected to pass through the box-like geometry in the given CRESST setup. Therefore they should create scintillation light in at least, in most cases exactly, two panels. These characteristics from muon signals require a definition of pulse height (energy equivalent) thresholds for muon candidate events.

As a simplification, which will be noted also later, the highest multiplicity signals will automatically be treated as event caused by muons for the fact that a very high initial energy is needed and only high energy neutrons or cosmic muons can possess this energy, range

and abundance. A justification for this approach is given after the muon definition, where additionally several aspects of $m = 2$ and $m = 3$ veto signals are discussed. Subsequently the focus of the discussion will be placed on muon rates.

Panel threshold and cut determination for Runs 30-32

The most important part in the decision if a veto event is in fact a muon is the determination of an energy threshold for the pulseheight in each panel, above which events are likely to be muons. The previous sections have shown that a simple threshold condition alone is not sufficient due to the high number of $m = 1$ veto events. Here as a first step the procedure to determine the threshold is explained in detail, and subsequently several data cut methods for higher multiplicity events, especially with multiplicity 2, are discussed. Considering that the largest amount of data was taken during Run32, the section starts with this run. All procedures will be explained on the basis of this data, and Run31 as well as Run30 are analyzed subsequently with the same methods.

Note on Run30, Run31

Due to lower available amount of data and therefore less statistics, some variations in the veto panel threshold determination were needed for Run30 and Run31. This will be explained in the course of this section in the appropriate sections.

5.2.1 Muon identification and tagging

Methods of μ threshold determination for panels

In previous studies [87, 102], the focus was placed to a greater extent on a *veto safe* signal identification as opposed to muon safe. The pulse height (energy equivalent) thresholds, above which veto events are considered as muon or muon candidates, were calculated in the following way: a condition was set on the sum parameter to only allow a selection of veto events with very high pulse heights, typically the maximum available[32] by the DAQ or close to that value. While in [102] only sum pulse heights larger than 4000 ch were used for the "Clear Muon Events" (CME) class, in [87] the lower limit on the sum signal was chosen at 2500 ch. With such a selection and no restriction on the multiplicity one can produce the resulting pulse height spectral histograms for each panel for the full available pulse height range. This simple yet effective measure, also used in this work, suppresses the dominant lower-energy contributions deriving mainly from $m = 1$ events, and also undesired background events as well as most contributions from environmental radioactivity and enhances the spectral "bump" in the pulse height distribution that is due to muons. The pulse height spectra were fitted with a Landau distribution as implemented in ROOT [110], and the fit results used to determine the thresholds for muon detection. This approach approximately provides the intended results of selecting muon candidate events, but there are some drawbacks in fitting only the Landau distribution to the relevant part of the pulse height spectrum. At small pulse height values the Landau function rapidly drops to zero[33] and thus is not suitable to include the rising background spectra seen in some panels (see e.g. fig. 5.2). Therefore the method is strongly dependent on the fit onset, which is critical for the fit to converge and to especially attain an acceptable width (resolution) of the resulting function. For these reasons, an improved method to extract the threshold information for muon identification was developed. The initial data preparation is similar to the previously described procedures. Here only the highest energy sum signals, i.e. $sum \geq 4095$, were selected, where data quality allows for it. Only for small data samples as in Run31 the procedure was modified and smaller sum values were accepted. Then with these data samples the histograms with the pulse height spectra for each panel were generated as shown in fig. 5.2. Subsequently the further steps are

[32] The digitizer (QDC), which was used, has a range of 12 bit, which translates to the usable pulse heights (also named 'bins' or 'channels' (ch) here) between 0 and 4095.

[33] see example in fig. 1.12.

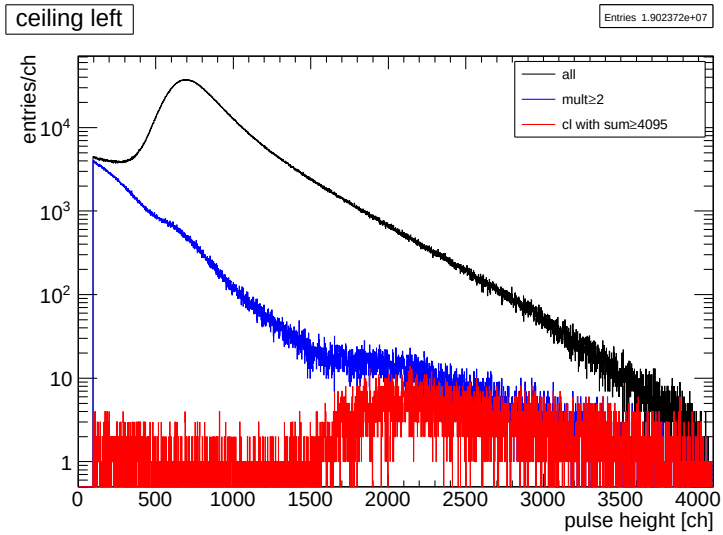

Figure 5.2: Example of data reduction used in the threshold determination process. The spectra shown are from the #1-*ceiling left* panel including all signals (black), all $m \geq 2$ signals (blue) and all events with sum ≥ 4095 ch. The important issue in this picture is that a clear muon peak is not visible even for the $m = 2$ signals, but is only revealed when an additional constraint is imposed on the sum.

- assume exponential or gaussian tail background (noise/low energy) contribution from near-threshold events for fit function in low energy regime.
- determine rough value for fit onset of the Landau distribution. This can be done by finding an approximate minimum between the low energy slope and the muon peak.
- perform both fits in reasonable respective part of the spectrum: low energy for background, high energy for muons.
- combine fit function over whole energy range.

Adding the exponential background to the fit procedure makes use of the whole pulse height spectrum and results in a more robust and better fit quality, i.e. peak determination and reduced width of the Laundau distribution. This allows a more consistent and and reliable determination of the muon threshold. Figures 5.3 and also 5.2 show the different influences of the low energy spectral region. A further advantage is that by using the whole spectrum it is possible to automatically calculate the threshold, where previously for each panel a fixed fit range needed to be provided.

The maximum of the Landau distribution defines the most probable value (mpv), where the maximum of the muon distribution is expected. It should be noted that this value is not exactly the *mpv* fit parameter in ROOT [111], but has to be corrected by a shift as noted in the documentation [110]. This leads to a slightly lower peak value of the distribution, see fig. 5.3. In contrast to [87,102] a slightly more conservative (i.e. higher, therefore more *muon safe*) threshold is defined here in view of the focus on muon identification. The cutoff at low energies is $2.0\,\sigma$ below the corrected *mpv* value instead of $2.5\,\sigma$ [102] and $3\,\sigma$ [87], where σ is the width parameter. This still allows for a high percentage of identified muons, but slightly reduces the number of muon candidates. With this acceptance level, the probability of identifying a muon can be calculated by integrating the normalized fit function to

$$P_\mu(m) = \left(\int_{threshold}^{\inf} f_{fit,normalized} \right)^m = 0.9935^m \qquad (5.4)$$

per panel, where m is the multiplicity. It should be emphasized that while this probability of a positive muon identification is lower than in [102] (applied to Run30) and [87] (applied

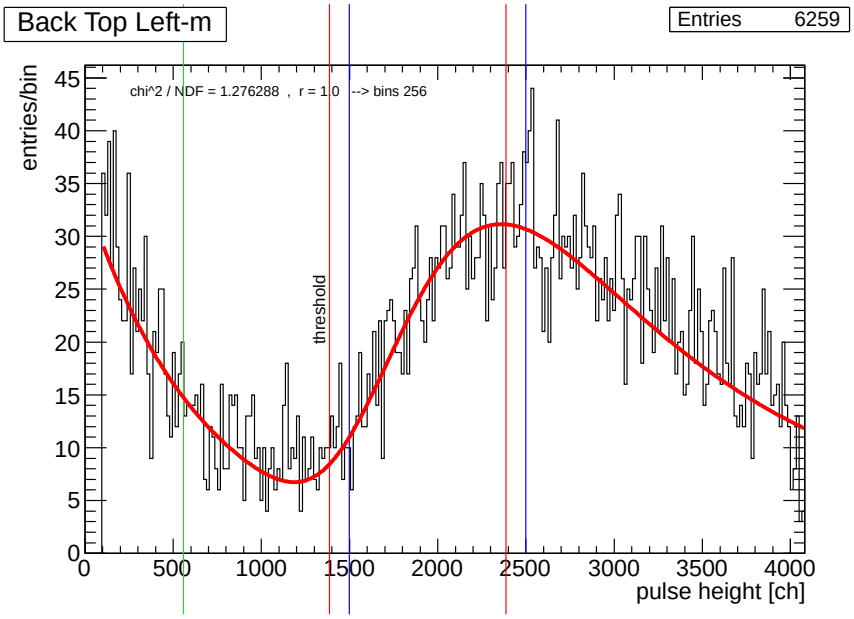

Figure 5.3: Example of the combined exponential & Landau fit of the whole spectral range for the #13-*back top left* scintillator panel. The red fit curve is a combined function of a low-energy exponential tail and a landau distribution to higher energies, clearly showing the muon peak. The vertical blue and red lines indicate the unshifted and the corrected threshold values used for the analysis.

to Run32), the chance of a false positive tagging of background events is also reduced, the selection is thus more *muon safe*. As mentioned, the procedure makes use of $m \geq 1$ veto events, and determines the muon threshold for each panel separately. In the further steps the resulting thresholds listed in tables 5.1 and 5.2 are used for the definition of a muon signal in the data.

Run31 and Run30

- Run31: due to the shorter run (see table 4.1), a lower selection value on the sum parameter was chosen for the data sample used for the threshold determination, namely channel 3000 instead of the overflow value of 4095. This allows for a larger number of events while still avoiding a large a data contamination from low pulseheight events. In Run32 and Run30 this step is not needed.

- In both Run30 and Run31, some panels do not allow a fully automatic fit of the spectrum with the method used in Run32 due to less statistics. The affected spectra were fitted again with modified starting parameters, giving very good results as shown in fig. 5.4.

- Run30: some data had to be discarded due to modified trigger settings in a few files.

5.2.2 Definition of data cut and muon candidates

In the course of this work, several methods have been tested to define an appropriate muon safe cut on the data. Within this section, the data cuts to define muons –in a muon safe context– are developed and explained according to the multiplicites of the veto events. Naturally, as already hinted in the explanation thus far, the most important factor in achieving a muon identification is to reduce the number of $m = 2$ and $m = 3$ veto events.

#	panel	threshold	mpv	width of fit (σ)
1	cl	1520.6	2107.7	293.6
2	cr	1885.4	2406.3	260.4
3	fl	1435.2	1945.7	255.3
4	fr	1129.3	1603.1	236.9
5	ftr	976.0	1759.4	391.7
6	ftl	989.1	1670.6	340.8
7	fbr	1106.7	1855.9	374.6
8	fbl	1692.9	2514.5	410.8
9	rtf	1349.1	2145.9	398.4
10	rtn	1661.9	2568.4	453.2
11	rbf	1417.4	2072.7	327.7
12	rbn	1109.8	1631.3	260.8
13	btl	1386.6	2387.3	500.4
14	btr	1051.5	1845.9	397.2
15	bbl	808.1	1555.4	373.7
16	bbr	624.8	1289.2	332.2
17	ltn	1327.4	2084.2	378.4
18	ltf	1100.4	2168.3	533.9
19	lbn	1058.3	1817.5	379.6
20	lbf	1233.1	1968.9	367.9

Values are in [ch].

Table 5.1: Calculated thresholds, most probable values and width from the combined exponential & Landau fit for Run32. Values are in DAQ channels. The most probable value (mpv) indicates the peak position of the muon distribution.

		Run31			Run30		
#	panel	threshold	mpv	width (σ)	threshold	mpv	width (σ)
1	cl	1379.4	1804.0	212.3	1625.5	2087.8	231.1
2	cr	2100.8	2540.4	219.8	2357.5	2895.6	269.0
3	fl	1144.6	1577.3	216.3	1609.7	2078.8	234.6
4	fr	1066.4	1435.4	184.5	1374.2	1803.5	214.6
5	ftr	1198.7	1770.0	285.7	1511.5	2240.8	364.7
6	ftl	1431.7	2171.7	369.9	1754.8	2626.8	435.9
7	fbr	1334.8	2022.1	343.6	1416.2	2101.6	342.7
8	fbl	1509.7	2277.6	383.9	1841.8	2490.1	324.2
9	rtf	1182.1	1823.0	320.5	1367.5	2006.5	319.5
10	rtn	1422.7	2022.6	299.9	1787.2	2513.1	362.9
11	rbf	1409.9	1830.8	210.4	1409.4	2060.9	325.7
12	rbn	309.3	594.9	142.8	1667.8	2372.7	352.5
13	btl	1691.2	2191.8	250.3	1490.9	2454.1	481.6
14	btr	1126.0	1610.4	242.2	1411.9	2174.8	381.4
15	bbl	931.0	1452.7	260.9	1527.6	2161.5	316.9
16	bbr	582.8	1183.5	300.4	980.1	1571.7	295.8
17	ltn	1111.5	1712.9	300.7	1224.2	1812.3	294.1
18	ltf	951.5	1651.2	349.9	1079.8	1915.8	418.0
19	lbn	958.0	1560.6	301.3	1204.9	1834.2	314.6
20	lbf	1107.8	1719.5	305.8	973.1	1670.8	348.9

Values are in [ch].

Table 5.2: Threshold values as in Table 5.1, but for Run31 and Run30.. The latter can be compared to the values from [102], which are listed in Table A.1 in the appendix.

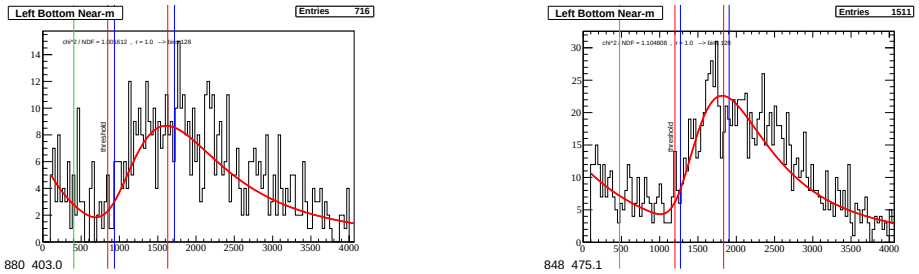

(a) Run31 **(b)** Run30

Figure 5.4: Example of the combined exponential & Landau fit of the whole spectral range for the #19-*left bottom near* scintillator panel, details are the same as in 5.3. A good fit can be achieved even with a low number (< 1000) of histogram entries.

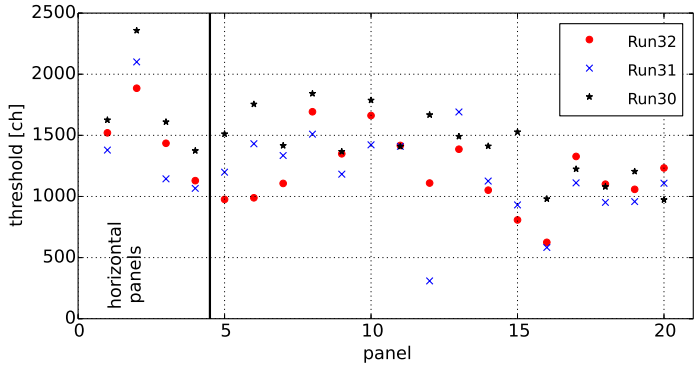

Figure 5.5: Comparison of calculated muon thresholds in Run30, Run31 and Run32. The labels on the abscissa denote the scintillator panels, the ordinate are the threshold values from tables 5.1 and 5.2. The tendency is similar between the runs, only the #12-*right bottom near* values show a large separation, especially for Run31.

Discussion of data reduction methods

The $m = 2$ and $m = 3$ event categories (classes) are overabundant in the raw data by a large factor (compare to fig. 4.16), where the major part can not be due to muons. Identifying all $m = 2$ signals as muons would result in a rate of $87.5\,\mathrm{h}^{-1}$, and for $m = 3$ events the respective rate would amount to almost $12\,\mathrm{h}^{-1}$. Both numbers for themselves are not compatible with the expected muon flux at the CRESST site $\sim 6\,\mathrm{h}^{-1}$, which explains the need for a clear and strong rejection of background events with those multiplicities.

Several ways of data reduction have been considered and tested for the mentioned event classes, starting with $m = 2$. It should be noted here that the term *panel threshold* refers to the software threshold for muon identification as calculated in the previous section and should not be confused with the hardware *panel trigger* values from the readout settings, which are comparatively low, usually at 96 ch.

$m = 2$ case

For this case, a combined cut on both contributing panel triggers is desired. There are a few feasible options listed below, where the indices indicate the panels:

- 2D sum : $(value_1 + value_2) > (threshold_1 + threshold_2)$
  This method selects an event population with a diagonal cut in the two-dimensional pulse height plane of the respective panels. An extension to higher dimensions ($m \geq 3$)

is possible. A disadvantage of this method is that the discrimination of veto events is possible only on the combined signal of two panels, as the selection includes clear non muon safe events.

- 2D product: $(value_1 \times value_2) > (threshold_1 \times threshold_2)$
  Also this method is an illustrative 2D cut possibility, which follows the distribution (see fig. 5.7) and can be extended to higher dimensions. While this method looks promising at first glance, it too can only discriminate veto events based on the combined signal of two panels. It is for example possible that a low energy signal in one photomultiplier would in coincidence with a high energy signal in another create a large enough product to pass the cut condition and be recorded as a muon even though one of the signals is below the panel threshold value. This is unwanted in a muon safe scenario.

- exclusive AND: $value_i > threshold_i$
  The threshold condition is imposed on each detector separately. Each signal can be handled as independent parameter and an event-by-event discrimination is possible. Naturally, this method can easily be extended to higher dimensions. This is the most conservative method for a muon safe data reduction.

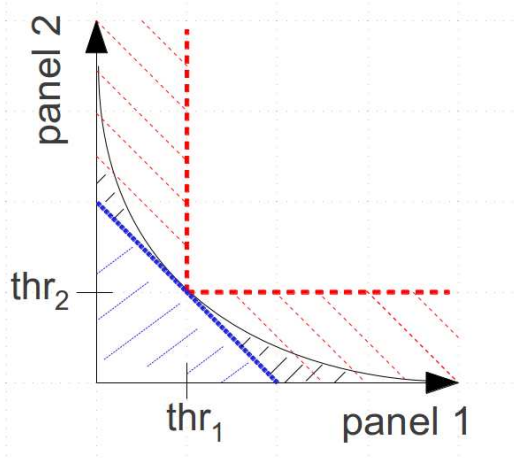

Figure 5.6: Symbolic representation of the three discussed cut methods. The area below the respective curve indicates that the panel-panel pulseheight combination signal is removed by the cut.
1 (blue), 2D sum: the sum of two panel trigger events is required to surpass the sum of the two corresponding panel threshold values.
2 (black), 2D product: the product of two pulse heights needs to be larger than the product of the corresponding threshold values. Equal to a 1/x function.
3 (red), exclusive AND: each signal has to pass its panel threshold independently.

A quantitative ranking between the methods can be seen in fig. 5.6, which is a symbolic representation of the different methods listed above. If one uses the example of two equal threshold values, as presented in the figure, the 2D sum cut is the weakest, removing the least amount of signals from the data sample. On the other hand, it is clearly visible that the third method, the exclusive AND cut, has the strongest requirements on the data, removing a larger portion of the data.

Between the second and third method, the difference in the number of selected muon candidate events is actually relatively small on the order of percents. This is reasonable, because a muon is in most cases passing through the setup and hitting either directly or via secondaries at least two panels, generating two or more high-energetic signals. These signals would survive both the second and third cut method, while a signal with a low pulse height in one panels would still be suppressed.

Finally, method 3 was selected for further use, since it especially allows the muon-safest event-based selection. The exclusive AND cut is applied for the cases $m = 2$ and partially

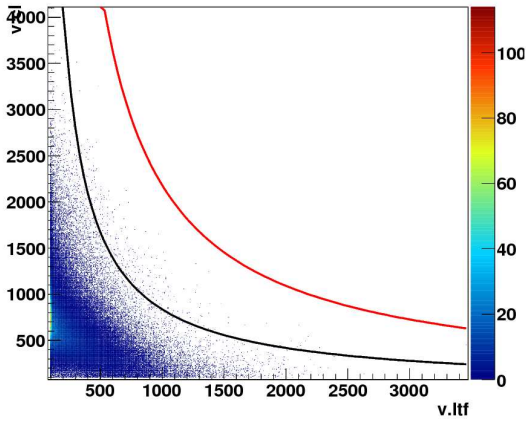

Figure 5.7: Cut method 2: illustrative example of the 2D product cut on the pulse heights of a horizontal and a vertical panel.

for $m = 3$: for $m = 3$ signals an additional decision level was introduced, see next section, and veto events with at least four panel trigger contributions ($m \geq 4$) are by default tagged as muon candidates.

$m = 3$ case

While the data selection cut on the $m = 2$ data is relatively straightforward, some reasoned explanation has to be given for the $m = 3$ case, and in principle also for higher multiplicity signals. Especially the $m = 3$ events are due to their large abundance still influenced by non-muon low energy contributions. The event structure suggests in some cases that a muon origin is unlikely, especially for high multiplicity events with a small sum signal, because the sum signal in principle is the total detected energy in the veto. Several scenarios for $m = 3$ veto events have been tested, which in principle can also be used in the same fashion for higher multiplicity events.

1. a cut requiring only two of the three signals to be above the respective thresholds. An argument supporting this method is that a muon crossing the veto detector would mainly create two strong signals, but there is a chance for a third signal, if e.g. an edge of another panel is touched.

2. as above in method 3 for the $m = 2$ case, the exclusive AND cut, requiring a pulse height larger then the channel's threshold value in each panel. This is a logical continuation, but also a rather strong requirement, since the cut quality for $m = 2$ events is already very good in suppressing background signals. A threefold AND is muon safe, but would reject true muons (see table 5.3), which is not desirable. Thus this method is not preferred.

In addition a few other methods have been tried:

3. a modified version of the cut above with relaxed conditions is to use only those $m = 3$ events, where two of three panels pass the panel threshold and the third is required to have a signal larger than an intermediate level. This level is defined via the exponential low energy tail, as shown by the turquoise lines in figures 5.3 and 5.4. The aim is to further remove a part of the low energy contributions in the pulse height spectrum.

4. a relatively weak cut was also tested, where all panel signals of the event are required to be larger than an arbitrary rather small value, set at 200 ch. The reason for this method is that a similar cut was used for the Run32 dark matter search publication of CRESST-II. Even with such a weak requirement a substantial amount of the $m = 3$ signals is removed, thus proving that most of these events are influenced by very small contributions by at least one panel.

The first method has an additional advantage. There exists a range of zenith/azimuth angles due to the recessed floor panels, which allows muons to create large signals in three panels. Choosing the softer condition of only two signals above threshold incoroporates these categories. Table 5.3 lists the results of all discussed methods and the number of events surviving the cut as well as their percentage relative to the original number of $m = 3$ signals. The raw $m = 3$ rate before cuts amounts to almost 12/h within the net measurement time, which is already twice the expected muon rate. Applying only the simple arbitrary cut reduces this to less than 2/h, and the more plausible cut as for $m = 2$ further lowers the rate to about 1.3/h.

	$m = 3$ candidate events	fraction of all $m = 3$
3x threshold AND	5512	4%
2x threshold, 1x intermediate	9947	7.2%
2x threshold AND	14819	10.8%
intermediate only	10547	7.7%
3x panel > 200	19826	14.4%

Table 5.3: Number of events which pass the different cut methods for $m = 3$ events, methods are detailed in the text. The original sample of $m = 3$ events includes almost 140 000 signals, or about 12/h, using the net measurement time.

Fig. 5.8 shows the resulting effective veto multiplicity distribution for all $m \geq 2$ events, when only two panel trigger pulseheights have to be larger than muon threshold. Only 2.7% of the muons are shifted to multiplicities below two. This effect can be easily explained by the decision to accept all events with $m \geq 4$ as muons without using the muon thresholds. The new 'reduced' multiplicity distribution can now be described by a single power law.

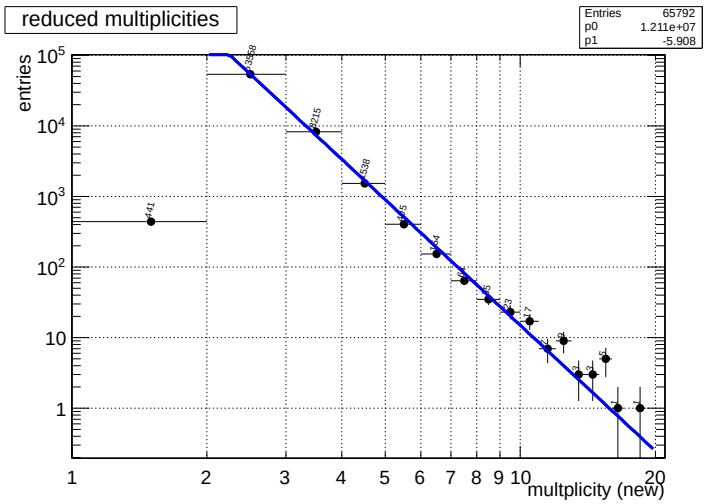

Figure 5.8: Run32: Reduced multiplicities with power law fit. Also the $m = 2$ and $m = 3$ events can be included now. The slope is slightly harder than in section 4.3, and only the highest multiplicity events do not agree with the fit.

5.2.3 Future improvements

Having observed the results of Runs 30, 31 and 32, where evidently the operating conditions of the muon veto were different from each other, it makes sense to use the settings from the earlier, shorter runs with caution and at most as a guidance, as the pauses between runs usually last a few months involving different upgrades and installations at the experiment.

If a muon identification should be made from the start of a run without adequate statistics for a Landau fit, it might be worthwhile to preselect a threshold range as long as not much

data is available. Here, the previous thresholds can already be tested, if they can be valid for a new campaign. This range can also be defined and narrowed down by a (re-)calibration in preparation for the run, where the panel response can be tested with the settings planned for later use.

Due to the small flux at the experimental site, a real-time monitoring of the muon rate is only reasonable after recording enough data to provide a good threshold determination. It could be shown e.g. in fig. 5.4 that less than 10^3 signals with the appropriate pulse height can be sufficient to get an acceptable fit and threshold calculation, which amounts to about one month of continous data taking.

5.2.4 Conclusion muon definition

In the course of this chapter, the definition of muon events in CRESST was outlined and described in detail. A consistent approach was developed, which effectively allows an in-situ calibration of the muon veto detector, with the reservation that a certain amount of data is needed. The results of the definition of muon events will now be compared in more detail than in section 5.2.1 to previous work for two different measurement campaigns (Run30 and Run32), and the major differences as well as some improvements are outlined.

After that, the validity of the definitions will be tested with several methods. This issue is especially important, since the preceding chapter showed that the raw signal rate is not very stable. Muons, however, depositing a large energy, should be detected at a constant rate.

5.3 Comparison of results with previous work

This work focuses on the *muon safe* detection and identification of muons as described at the beginning of this chapter. Due to this, a contrast to the previous work of [87] and [102] as well as the data selection used for the CRESST Run32 publication emerged.

Because the definitions of muon candidate events are different in each of the two theses, the results are only partially comparable. A short overview of the basic differences is given here, and a comparison will be attempted where applicable by using either the cited results or implementing the cited methods on the data.

5.3.1 Run32 I

S. Pfister [87]

The selection procedure for muon candidates is detailed as following:

- as already noted above, the muon definition in [87] requires the sum channel signal to be above 2500 channels.
- the veto event multiplicity has to be at least two, as here for the muon safe case.
- each of the contributing panel trigger signals has to pass a threshold determined by a fit of a Landau distribution on the panel pulse height spectra, similar to section 5.2. The threshold is quoted as a lower 3σ boundary, which is assumed to result from the same approach as in this work. The lower threshold means a more veto safe identification, but requiring each panel to pass the threshold is in principle a m-fold AND cut for multiplicity m, which is strongly muon safe.

Introducing the cutoff on the sum as described in the first item excludes a number of possible muons. This is due to the fact that the sum trigger parameter results from the analog sum of all panels in the DAQ, which is not equal to the digital sum of all contributing panel trigger signals. Furthermore, there are several panels with muon thresholds below 1000 ch, which indicates that a sum of two such signals is smaller than the cutoff. Since the panel threshold values used for the muon selection are not listed in [87], a direct comparison with the number of selected muons is not possible. However, the difference created by the sum

cutoff can be quantified in the following way: the conditions listed in the items above are applied, but the threshold values of this work (Table 5.1) are used.

First the effect of the sum $>$ 2500 ch condition is considered, which results in 63135 muons. Without the restriction on the sum the number of muons is 65792; the difference is illustrated in fig. 5.9. As expected, the largest effect can be seen for $m = 2$, as it is more likely that the sum parameter is still below 2500 ch for a two-panel event as opposed to higher multiplicity events, notably there is no difference for $m > 5$, where the all events have a large sum channel signal. The large difference for $m = 4$ is a result of the convention in this work to accept *all* such events as muons. The constraint on the sum misses 4% of the positively identified muons overall, and 3.2% of the $m = 2$ muons. Thus it is advisable that no sum cut of this magnitude should be applied.

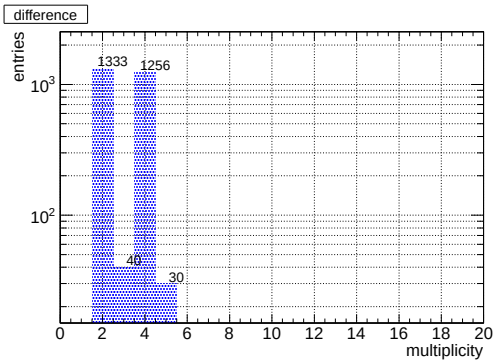

Figure 5.9: Effect of the condition $sum > 2500$ as in [87]. Events with multiplicities 2-5 are removed from muon sample when requiring The thresholds listed in table 5.1 are applied here. The main difference is visible for the $m = 2$ and $m = 4$ events. For $m = 4$ the difference is large, because in the proposed cut *all* $m \geq 4$ signals are considered as muons. For $m > 5$ there is no difference, the sum then is always > 2500 ch as one would expect.

A short comment is in order regarding the third item listed in the selection procedure above. If one takes into account the handling of higher multiplicity signals as detailed in [87], then much more signals are removed from the muon sample. As described above, **each** panel pulse height has to be larger than the respective muon threshold in this panel[34].

The consequences for higher multiplicity signals are rather drastic, shown as a muon multiplicity histogram in fig. 5.10. In black the standard sample as resulting from the muon safe cut of this work (see section 5.2) is shown, and in red the same for the selection 'each panel pulseheight above panel threshold', here also called *hard cut*. In principle this hard selection is strongly muon safe, but leads to the rejection of clear muons, which is a major drawback.

With the hard cut the maximum multiplicity is reduced to eight as opposed to 19, which is the maximum in Run32. A reduction in multiplicity itself is not surprising, since, as noted earlier, many high multiplicity signals have small pulseheight contributions from at least one panel trigger. The problematic issue here is, however, that with this strong signal rejection, as can be seen for example by the strongly reduced maximum multiplicity, a large amount of very high multiplicity m veto events is not accepted as a muon, even if in these events $m - 1$ panel pulseheights fulfill the threshold conditions and only one panel pulseheight is below the muon threshold[35].

The 'hard cut' approach rejects a fraction of more than 25% of all muons as defined in this work. While the selection leads to a data sample, which only includes muons, the muon flux is greatly underestimated. Especially high multiplicity muons, which are more likely the result of showers and therefore can be more dangerous, are discarded from the vetoed muon sample. Due to this problem this cut should not be be applied.

[34] See also the discussion of $m = 3$ events in section 5.2.2 and table 5.3.

[35] For example, the two events with the highest multiplicities, $m = 19$, would be discarded in this scenario.

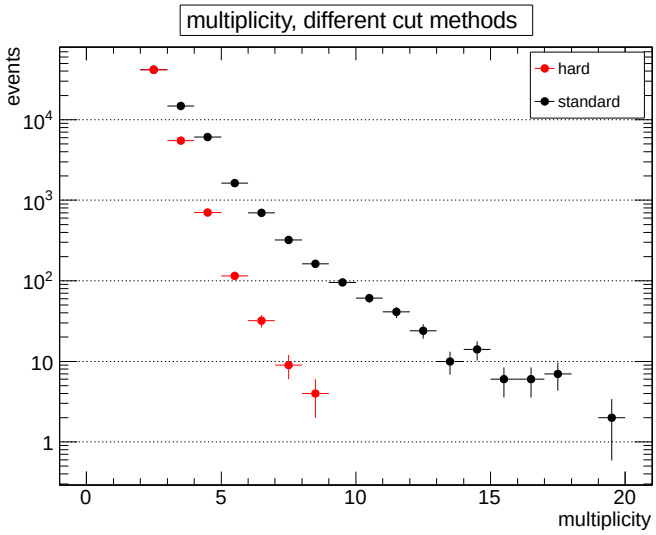

Figure 5.10: Comparison of cut methods: standard muon sample (black, right) and muon sample after applying the cut *each panel signal above muon threshold* (red) [87]. The condition $sum > 2500$ ch is not used here.

5.3.2 Run30

M. Kimmerle [102]

The data used in that work only cover the limited amount of about 1/6 to 1/4 of the measurement time in Run30. A direct comparison to [102] is difficult, because only the length of the data sample is noted, but it is not known which part of Run30 was used. In the previous chapter two periods can be seen, one of which is likely the analyzed one. Nevertheless, an acceptable fit of the muon Landau distribution could be achieved, see fig. 7.2 in [102]. The resulting threshold values from [102] are listed in Appendix A.2. Since in that work a larger part of the Landau distribution was used by choosing the thresholds 2.5σ below the peak of the distribution, those muon thresholds are not directly comparable and were recalculated using the 'mpv' values and the width as listed in the Appendix. In most cases the re-calculated values are slightly lower in the work presented here, which has two reasons. First, the peak value (most probable value) of the Landau distribution in [102] was not corrected for the shift as noted in the ROOT documentation. Secondly, in this work almost the complete Run30 was used, enabling a better fit due to the larger data sample in spite of the stability problems. The fact that the full spectral range of the panels is fitted in here also improves the fit quality.
In [102] the events are separated in three classes:

1. the *All Recorded Events* (ARE) is the simplest group, including all veto events registered in the DAQ. By definition this event class is veto safe.

2. the *Clear Muon Events* (CME), which contains all recorded signals with a sum channel pulse height of at least 4000 ch, i.e. almost the maximum value allowed in the DAQ; these events amount to more than half of all tagged muons. For this event class, as the name suggests, it is unlikely that background signals are included, thus it is a muon safe selection. However, as noted in the thesis, the event class "is designed to learn about the distribution of the muon events in the single panels", and not all actual muons are contained in the selection.

   This event group basically is the selection sample used to acquire the pulse height spectra for the Landau fit, see section 5.2.1.

3. the *Dangerous Veto Events* (DVE), which aims to include as many muons as possible while keeping the influence of background events small. Consequently this class of

events is a hybrid between muon safe and veto safe, although, as described below, leaning towards muon safe. Only for this event class the calculated panel thresholds are applied.

The DVE class is split into two cases:

a) for $m = 1$ signals, only pulseheight values larger than the most probable value (peak) of the Landau distribution are used. In this way it is argued that still most of the $m = 1$ muons, an estimated 70%, are included in the resulting selection. The thesis quotes a simulation, according to which only 5% of the total muon flux should have $m = 1$, which is also in good agreement to the observations made here.

b) for $m \geq 2$ DVE events, the threshold determined by the Landau fit is applied, and the event is categorized as a muon if *one* contributing panel has a pulse height above its threshold. All events with larger multiplicities are handled in the same way.

Additionally, the $m = 0$ event class is completely included in the DVE group, but not discussed further. This adds a large number of signals to the muon selection, which are highly unlikely to be actual muons. Therefore the muon rate in [102] for the CME event class was determined to about $5\,\mathrm{h}^{-1}$, while for the DVE class a mean rate of roughly $200 - 220\,\mathrm{h}^{-1}$ is indicated, about 35 times higher than the expectation. Since the CME class doesn't include all muons, the DVE cut is analyzed further.

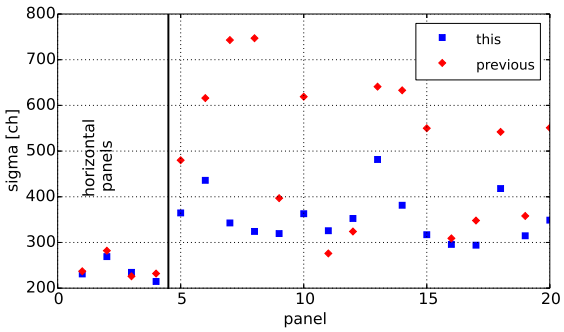

Figure 5.11: Run30: Comparison of fit widths σ of this work (blue) and [102] (red). The blue entries are similar for the horizontal panels, and for the vertical ones have smaller width (i.e. better fit) and more consistent parameters σ as a result of the new fit procedure using the whole spectrum.

Validity DVE cut vs muons

There are several key differences to the data handling proposed here. For the $m = 0$ and $m = 1$ event classes, it is difficult or impossible to give precise predictions for a muon-related rate from the data alone, since for the former ($m = 0$) no viable parameter can be used and for the latter the pulse height region where muons are expected is strongly influenced by a large amount of signals, which are unlikely to originate from muons. Hence the discussion is turned around and an estimate is given, which fraction of these event classes could be due to muons. This was done in section 4.5.

The main improvement of this work to [102] can be seen in fig. 5.11, where the fit results are clearly more consistent. The fit widths are distributed over a much narrower range and demonstrating the similar behavior of all panels. On the left side of the figure (entries 1–4), the horizontal panels have a consistently lower threshold than the vertical ones. This is owned to the shorter path through the scintillating material, which results in less straggling. The smaller widths from the fits as a consequence yield a higher threshold for the same chosen σ range, enabling a more muon safe data selection.

Since in [102] the $m > 1$ signals require only one of the panel triggers to pass the threshold, a much larger number of muon candidate events can be expected. We now try

to compare the results with these conditions to the outcome from the muon cut of this work, which requires at least two panels passing the threshold criterion for $m = \{2, 3\}$. Both Run30, which can be directly compared to [102], and Run32 are taken into account. The net measurement period of Run32 is about 3.5 times longer than Run30, therefore the

	panel	Run30	Run32	Run32 this work
horizontal	cl	3140	18768	12395
	cr	2803	12395	12369
	fl	8308	64738	14861
	fr	22922	29452	14245
vertical	ftr	2746	4557	7053
	ftl	1087	3492	6796
	fbr	2390	6890	6363
	fbl	1124	5384	7006
	rtf	9974	8067	8077
	rtn	6271	5723	8189
	rbf	1244	5006	6457
	rbn	731	2860	6960
	btl	3019	14896	7931
	btr	1156	3507	7807
	bbl	696	7458	5916
	bbr	641	6130	5521
	ltn	3126	3724	8564
	ltf	991	9936	9661
	lbn	3596	6099	7080
	lbf	7391	4850	7929
overall, method as [102]		83356	223932	
cut method, this work		20322		65792

Table 5.4: Application of the DVE cut from [102] in Run30 and Run32 with muon candidate events in columns 2 and 3. Notice the large variations in the second and third columns, which result from low energy influences of at least one panel in $m \geq 2$ signals. This points to a consistency problem of the cut method. The grey shaded examples are neighboring panels and should detect a similar number of muons. The corresponding results for the muon definition in this work present more consistent results, demonstrated in the last column.

corresponding number of tagged muons should also have the same ratio. Table 5.4 lists at the bottom the numbers of candidates with the cut method of [102] and in contrast in the last line the results with the muon cut of this work. For the former, the ratio of Run32 vs Run30 is 2.68, while for the latter the same gives a result of 3.24, much closer to the ratio of the measurement times (table 5.5), which indicates a more stable cut method in this work. In table 5.4 the variations between columns 2 and 3 are huge, also among panels of the same

	ratio $\frac{Run32}{Run30}$
one above threshold	2.68
two above threshold	3.24
measurement period	3.52

Table 5.5: Run32 vs Run30 results for different muon tagging methods, compared to the lengths of the two measurement periods. The condition 'two panels above threshold' is closer to the measurement period ratio, indicating that the cut works better for both runs.

type, some of which are marked. This is an indication that the cut method includes a large number of non-muon signals. The last column also shows some variations, which in part

result from higher-multiplicity contributions to muon events, as all muon-tagged entries are listed in the table. Concluding it can be noted that [102] used a two-fold approach, selecting different event classes with the CME group as the more *muon safe* approach, but missing a large fraction of muons. The DVE class, however, is a more *veto safe* selection including all $m = 0$ signals and requiring only one pulseheight above the muon threshold. Table 5.4 also shows the effect of this more veto safe approach: the number of accepted muon candidates varies strongly within a group of similar detector panels, best illustrated for the horizontal panels. In the last column of the table, the number of muon signals is more consistent for both vertical and horizontal groups of panels. The variations in this column mainly result from the the higher multiplicity muons ($m > 2$), which are counted as muon signal in the panel in the table.

5.3.3 Run32 publication

In the main publication [56] of the CRESST-II Dark Matter search Run32 also muon coincident detector module events are mentioned. The muon rate is not explicitly given, only the number of muon coincident cryogenic events signals is indicated, where at least one module has a signal in the nuclear recoil signal in the dark matter acceptance region. The selection criteria ('CRESST cut') used for these muon coincident signals were the following [112]:

- **[type 1]** a time window of ±2 ms around a cryodetector event is chosen. All contributing panel triggers must have pulse heights larger than 200 ch. For the muon coincident neutrons above no separate restriction is applied on the veto multiplicity[36].
- **[type 2]** the same conditions apply as for type 1, but the veto multiplicity is larger than one.

A short overview of the expected muon numbers and rates with this type of definition is given here (table 5.6). This veto cut as used for the CRESST publication poses very soft conditions on muon candidates. Only the lowest energy signals, which mostly contain background signals, are removed from the data by the type 1 cut. This type of data selection is a clear example of a *veto safe* method, which aims to include all veto coincident cryogenic signals. But it also leads to an artificially large dead time especially for the type 1 signals (∼3.5%), and thus unnecessarily increases the amount of vetoed background data.

The class of type 2 events still provides more than 3.2 million muon candidates for Run32, translating into a rate of about 280/h, about a factor of 50 higher than the expectation for the muon flux and the muon rate determined in this work.

	number	fraction [%]	rate [h^{-1}]
type 1	180728405	84.4	15600
type 2	3201903	1.5	280
all Run32	214074184	100.0	

Table 5.6: Muon candidate numbers and fraction relative to all veto signals as well as approximate rates for the data cut method used as in the CRESST publication.

5.4 Plausibility of muon definition

In this section, the muon rates in Run32, which result from the definitions and data selection in this work, are covered. Different methods are used to test if the rates are plausible. Naturally, one test of the validity of muon thresholds and definition is to compare the measured with the expected muon rate.

The easiest check is to calculate a simple muon rate by dividing the number selected muons by the whole net measurement period. For the data of Run32, this yields a mean

[36] The $m = 0$ veto events are not considered as muon candidates in this context.

rate of 5.7 muons per hour over a measuring period of about 1.5 years, which is slightly less, but still in close agreement with the expectation calculated in eq. 5.3.

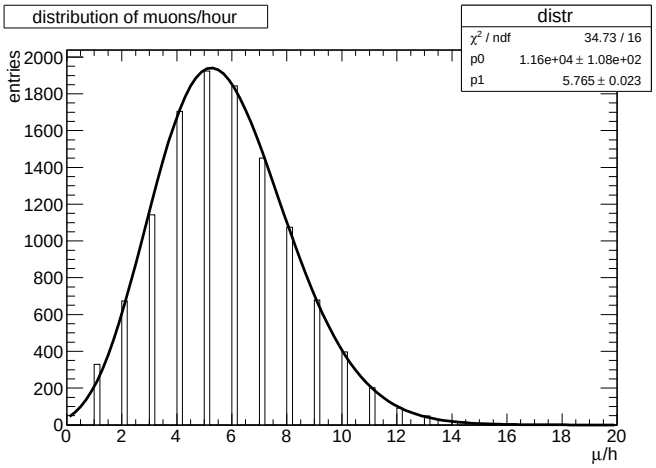

Figure 5.12: Poisson distribution with fit of the hourly muon rate. The mean of the distribution yields an average rate of 5.8 muons per hour.

According to the MACRO data, visualized in figure 5.1, the majority of muons is expected from zenith angles of about 30°. This should reflect in the data in the following way: the horizontal panels (ceiling and floor) should register the highest amount of muons in combination with other panels. The vertical panels have a smaller effective area, modified by the available entry angles for muons, as shown in section 5.1, thus resulting in a smaller muon flux compared to the horizontal panels. In principle the vertical panels should measure almost the same flux each. However, this is modified due to the fact that the bottom vertical panels do not have a full overlap with the floor panels, so especially for $m = 2$ signals a lower number of muons should be measured in those.

5.4.1 Muon rate in panels

Due to the geometry, the number of muons should vary between the different panels. The side panels ('walls', vertical panels) present a smaller effective area, because muons arrive mainly from near zenith, and the ceiling panels have a hole, reducing their area. On the other side, the floor panels are a little bit smaller than the ceiling panels, but for muon events, this effect is in principle cancelled, because the panels are on the inside of the four walls and therefore receive a signal in most cases where a muon passes through a side panel. Figure 5.13 displays the resulting muon rates in the respective panels. The first row contains the ceiling and floor panels, and second and third rows (left to right) the front, right, back and left walls, all seen from a position standing in front of the cryostat. The figure nicely shows that the muon rate per hour is larger in the horizontal panels ($\sim 25 - 30\,\mathrm{d}^{-1}$) by about a factor of two, as one would expect. Note that the daily muon rates in fig. 5.13 are not restricted to $m = 2$, but contain also the panel contributions to higher multiplicity events.

5.4.2 Contributing panels

One can check the muon definition validity also with the contributions of different panels to the $m \geq 2$ muon signals, where no overabundance should be expected for panels of the same category, vertical or horizontal. Table 5.7 furthermore lists the number of muon hits in each panel explicitly. In the right columns all muon events to which the panel contributes a signal are displayed, i.e. also higher multiplicity events, which explains the larger variations among the entries. The middle columns contain only $m = 2$ muons, where the numbers do not vary much for panels of the same type, which supports the cut method.

More importantly, $m = 2$ the remarks at the beginning of sec. 5.4 are nicely reflected in

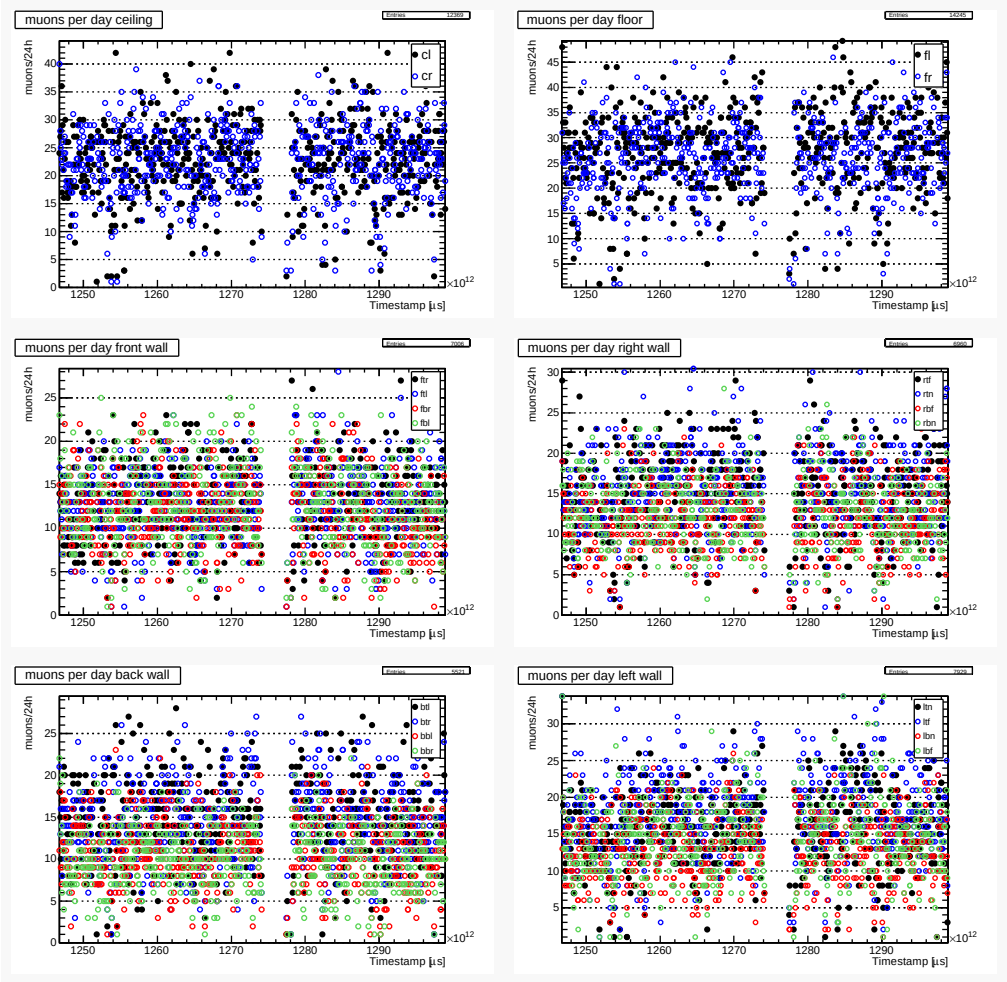

Figure 5.13: Muons per day in the scintillator panels after applying the data cuts.
first row: ceiling (left) and floor panels
second row: (left to right) the front and right wall
third row: (left to right) back and left wall.
The figures illustrate nicely two issues: the average number of muon signals per day in the horizontal panels is higher than in the vertical panels, just as one would expect, and the floor panels show a slightly enlarged muon count compared to the ceiling panels. Furthermore, all panels display -on a daily average- the same behavior.

the data. The horizontal panels have a substantially larger muon rate[37] than the vertical panels, and the floor panels show with $\sim 18.2\,\mathrm{d}^{-1}$ more events than the ceiling panels with $\sim 14\,\mathrm{d}^{-1}$. It is also noteworthy that the upper vertical/side panels consistently have a larger number of muon signals than the neighboring lower ones with only one exception. On average, the number of muons in a vertical top panel is 3771 ($\sim 7.8\,\mathrm{d}^{-1}$), while the mean for the bottom panels is 2788 ($\sim 5.8\,\mathrm{d}^{-1}$), about 25% less. From the geometry it is clear due to the recessed floor panels that the bottom side panels should detect a smaller $m = 2$ muon flux compared to the top side panels.

5.4.3 Time between muons

If the muon events occur independently, one expects an exponential distribution of the time between two muons. The slope parameter of a fit to this distribution then yields the muon

[37] The muon rate per day are indicated only for the $m = 2$ muons, where the variations are the smallest.

panel	m=2	m≥2	panel	m=2	m≥2
cl	6707	12395			
cr	6816	12369			
fl	8852	14861			
fr	8769	14245			
ftr	3947	7053	btl	3348	7931
ftl	3648	6796	btr	3549	7807
fbr	2612	6363	bbl	2689	5916
fbl	2726	7006	bbr	2772	5521
rtf	3843	8077	ltn	3845	8564
rtn	4051	8189	ltf	3939	9661
rbf	2862	6457	lbn	2694	7080
rbn	3066	6960	lbf	2881	7929

Table 5.7: Run32: muons in each panel. The middle columns show the contributions to muons, which only hit two panels ($m = 2$), while in the right columns also higher multiplicities are considered, thus the larger numbers. Panels with light grey background are the bottom side panels.

rate. Using this parameter has the advantage that all issues like short data files and pauses between files are no concern. Fig. 5.14 shows the histogram of the time difference between

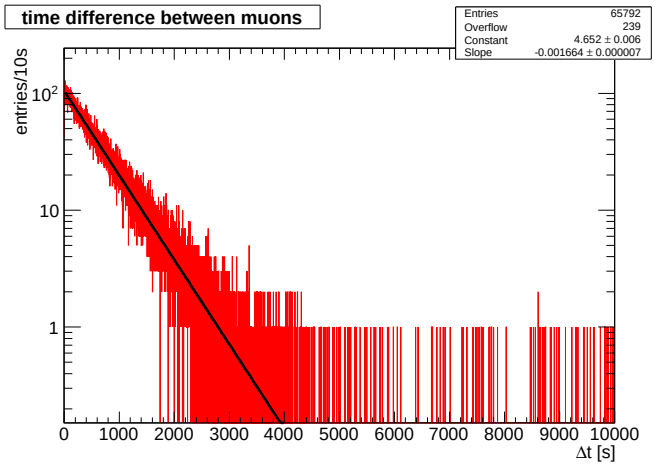

Figure 5.14: Run32: Time difference between muon-tagged veto events with a multiplicity of at least two in bins of ten seconds. A clear exponential slope corresponding to a rate of $5.99\,\mathrm{h}^{-1}$ is visible, up to $\Delta t \approx 1\,\mathrm{h}$, where the statistics become worse. The events at large Δt result from pauses between two data files.

muon events. The entries in the right half of the picture at very large Δt result from the pauses in data acquisition, for example refilling periods, and are not relevant. With the fit parameters listed in the figure, the muon rate for $m \geq 2$ can be determined to (5.99 ± 0.03) per hour, which is in good agreement with the mean muon rate, accounting for off periods, of $5.73\,\mathrm{h}^{-1}$. A similar procedure for all veto events yields $5.2\,\mathrm{s}^{-1}$ for the overall event rate in the whole system for Run32, confirming the averages calculated from the number of events in the files.

5.5 Muon flux variation

The yearly modulation amplitude of the muon flux is about 1.3% with the maximum at June 28th, accurate to less than one week, as most recently published in [107] with a total exposure of $\sim 4.6 \cdot 10^6$ muons from four years of measurement. The BOREXINO experiment

can detect around 4300 muons per day with a cross section of $146m^2$, about 30× more than is measurable in the CRESST experiment. Hence, it is unlikely that a seasonal variation of the muon flux can be detected in CRESST. A short plausibility argument is given here. For the CRESST muon veto one expects around 140 muons per day and $5 \cdot 10^4$ muons per calendar year. When the seasonal modulation is approximated by the summer quarter as maximum and the winter quarter as minimum with each about 11000 muons, the modulation would amount to slightly more than the 1σ statistical fluctuation of $\sqrt{11000} = 105$. Therefore, it is not possible to make a statement about the seasonal variation with the statistics of only about 18 months of available data from Run32. The mean-subtracted muon rate is shown

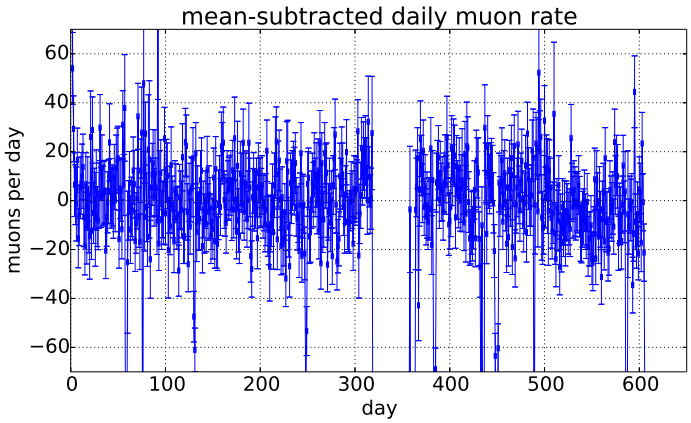

Figure 5.15: Daily muon rate in the veto during Run32 with subtracted mean.

in fig. 5.15. Within the error bars almost all data point are around zero, but the statistical error is rather large. There are a few periods either without any recorded data or without muon data, which warrant a short explanation. During the neutron calibration run, the polyethylen shield needed to be opened, because no suitable neutron source was available to irradiate the cryogenic crystals from the "source express" system integrated into the copper shielding, while this procedure was possible for a gamma source. Since the plastic scintillator panels are on the inside of the neutron shield, they also had to be moved aside. Thus the veto had to be switched off and opened during the neutron calibration, and there are no data for this period.

5.6 Discussion of damaged panel

In the early morning of April 6th, 2009, a 5.8 Richter scale earthquake occured with the epicenter close to L'Aquila. The earthquake occurred during the cool-down phase of Run32, and no veto data was being taken during this period. Because after the earthquake a shift of a part of the polyethylen neutron shield was found, in the analysis of [87] it was argued that also the CRESST muon veto was potentially harmed, specifically that the panel #18-*left top far*, which is closest to this polyethylen structure defect, may have been damaged.

Event rate The event rate in this panel in Run30 prior to the earthquake is very small also compared to other vertical panels. During Run32, the signal rate in this panel varied strongly; the average rate, however, with ~100-250 /h is similar or lower than most vertical panels.

Spectrum The Run30 pulse height spectrum shows a very hard spectrum at the lower end, which could be the cut off QDC pedestal of this channel. In addition a very interesting observation can be made. The typical $m = 1$ peak seen in other panels (section 4.8.2) does barely exist. Instead, this panel does not have many $m = 1$ events, but the overwhelming majority veto events with a contribution from the #18 panel are in fact $m = 2$ events with

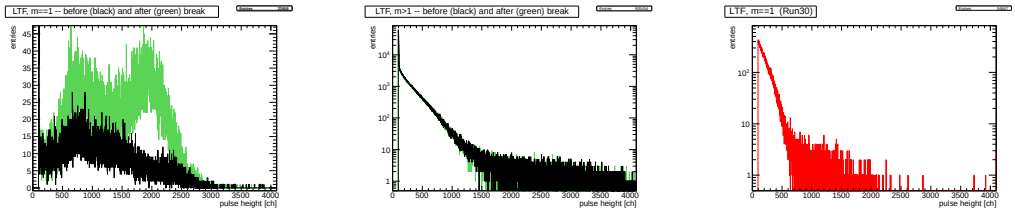

(a) $m = 1$. The typical peak is strongly suppressed. The second peak appears in the last phase of Run32.

(b) $m > 1$. The spectra are almost identical. Selecting phases with different signal rates gives the same result.

(c) Run30 $m = 1$ spectrum.

Figure 5.16: Panel #18-*left top far* before and after the neutron calibration break in Run32. The majority of events recorded in this panel is registered as $m > 1$. On the right the corresponding $m = 1$ spectrum for Run30.

characteristics like the pedestal tail, which are usually seen in the $m = 1$ spectra. This suggests that during Run32 there was a problem in the readout logic. The hard spectrum

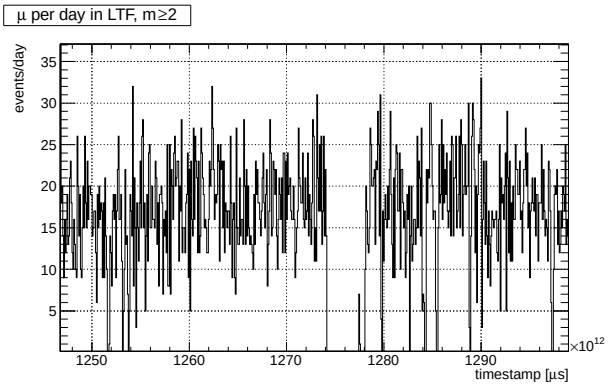

Figure 5.17: Daily muon rate in the #18-*left top far* panel.

near the panel trigger most likely is the right shoulder of the QDC pedestal, and for larger pulse heights in fact is a rather good panel with not much background. Subtle changes, e.g. of the signal cable grounding[38], could be responsible for the rate variations seen in this panel. The procedure for identifying muons in the #18-*left top far* panel is done in the same way as for all other panels. During Run32 the muon rate in this panel, shown in fig. 5.17, is consistent with the muon rates in the other vertical panels, which indicates that no significant damage occured in this panel and it can be used normally.

5.7 Summary muon definition

Before the analysis of coincident signals between the muon veto and the detector modules, a short summary is given to recapitulate the main points of this chapter. A muon in this work is defined in the following way:

- $m \geq 2$ and
- at least two panels have to pass the muon threshold defined in this chapter.
- $m \geq 4$ are accepted as muons automatically. This can introduce a small amount of low energy veto events, where the previous condition is not fulfilled.

[38] After the conclusion of Run32 and during the preparations for Run33, unsteady grounding of some signal cables was found.

With this definition the result is a *muon safe* data sample. Single-hit veto events are not considered as muons, because a clear identification is not possible. However, in some aspects such $m = 1$ signals can be useful to analyze the coincidence data. In these cases, the $m = 1$ signals as in fig. 4.29, i.e. the events with a single pulse height above the muon peak, are used. They are then referred to as 'muon candidate events'. The measured rate of ~ 6 muons per hour with these definitions is in very good agreement with the flux expectation from the depth-intensity relation.

An important result of this chapter is that the muon rate is stable and the rate in each panel is reasonable, shown in fig. 5.13, and in contrast to the event rates in the panels presented in section 4.1, there are no rate jumps. Also the overall daily muon rate (fig. 5.15) does not exhibit instabilities.

6

Veto coincident detector signals in Run32

After the definition of muon events, the next important step is to correlate the $CaWO_4$ detector module data with the designated muon events. Muons are expected to induce various types of unwanted background signal in dark matter experiments, of which the most dangerous events are created by muon-induced neutrons or neutron-like particles scattering in the crystals.

As a first remark it is stressed again at this point that the concept of the muon veto system is the (safe) identification of muons and subsequently the undesired background signals they induce in the detector modules, most importantly in the acceptance region for dark matter search. The differentiation between a *muon safe* and a *veto safe* muon definition, made in section 5 is therefore also relevant here. In the veto safe case some detector signals could be misidentified as muon coincident and thus too many signals could be removed from the data, even if they are not caused by muons. For this reason, the key aspect is finding a method to clearly select the data sample responsible for true coincidences between veto events or muons and the detector modules.

The approach is as following: at first the *muon candidate* veto events (high energy $m = 1$) as described in the summary in section 5.7 are inspected. It will be shown that no relevant information is lost in terms of coincident signals with the detector modules by discarding the veto events designated as 'muon candidates'. After that the muon selection for Run32 according to the definition in this work, recapitulated in section 5.7, will be cross-checked with the detector modules and a coincidence rate will be determined.

Note regarding timing convention

The veto timestamp has a higher precision than the rise time of a detector module signal, which is of the order of milliseconds. Since for a muon induced signal the veto timestamp is expected prior to a cryodetector signal, it is more suitable to define the coincidence time. The coincident events are expected to be centered at a time difference close to zero on the scale of the experiment and only determined by cable lengths, the electronics and detector time scales.

The timing convention for coincidences in this chapter is such that positive time differences Δt between muon and detector module indicate that the muon occurs prior to the detector module signal.

Detector coincidence time window

As a time window, in which different detector module signals are still registered as coincident, an interval of 10 ms around the veto timestamp was chosen in this work instead of 5 ms as in [56].

6.1 m=0

In section 4.6 it was argued that multiplicity 0 veto events are unlikely to be muons and even the largest $m = 0$ sum pulseheights are not caused by muons. It is rather assumed that those signals result from electrical perturbances. Were this assumption true, one can not expect a coincidence signal in the Δt distribution of $m = 0$ signals and the detector modules.

For slightly more than half of Run32, this was tested for all $m = 0$ events, shown in fig. 6.1. More than 4300 coincident signals have been recorded, which results in an average of $0.7\,\mathrm{h}^{-1}$. Fluctuations can be seen in the figure, but there is no significant signal[39] of true coincidences in the otherwise flat distribution. Given the rate of $m = 0$ events listed in table 4.4 and assuming an average cryodetector rate of $1\,\mathrm{s}^{-1}$, the expected rate of accidental coincidences would be close to 6000, which is fully consistent with the result in fig. 6.1.

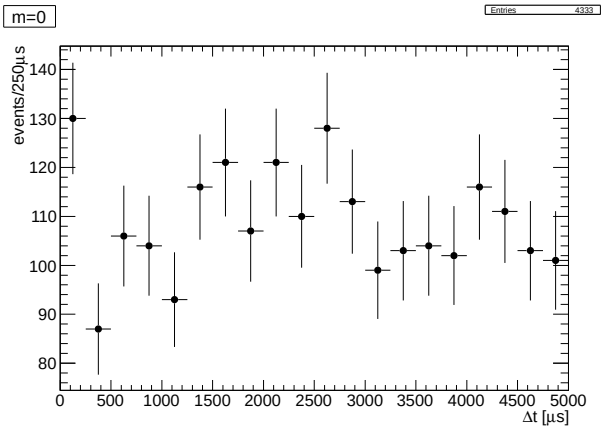

Figure 6.1: Time difference between $m = 0$ veto events and detector module events in bins of $0.25\,\mathrm{ms}$. In the flat distribution no coincidence signal can be seen, which would be expected at about $\Delta t = 1 - 2\,\mathrm{ms}$ (see fig 6.4). Note that only $\Delta t > 0$ is shown here.

6.2 m=1

As previously argued, the $m = 1$ muon candidates are overabundant even when only considering signals larger than the peak (most probable value) of the Landau distributions in each panel. In this part of the pulse height spectrum about 70% of the $m = 1$ muons would be included. The problem is, that this results in a huge amount of muon candidates, almost a factor of 50 larger than the expected rate. Because single-hit muons also make up only a small fraction of all muons, the argument that this data sample consists of mainly muons cannot be upheld. However, the data set containing these $m = 1$ signals is kept as a sample of *muon candidates* as explained in section 5.7 for further analysis and consistency checks. Consequently, if one searches for coincidences between these signals and the detector modules, a potential signal is expected to be small compared to a large random background in a given range of Δt. A first sample is displayed in fig. 6.2. The histogram does not show a coincidence signal, but has an average level of about 90 events per bin, consistent with random coincident background in the $\pm 10\,\mathrm{ms}$ time window from the $\sim 1.5 \cdot 10^6$ muon candidates again assuming an average cryodetector rate of $1\,\mathrm{s}^{-1}$. In fig. 6.3 the data sample only contains multi-detector events in coincidence with muon candidates. This second example is given to test the scenario described in section 4.5 that a single-hit muon either directly hits several crystals or creates secondary particles, which cause signals in the detector modules. There

[39] A signal would be expected around $\Delta t = 1\,\mathrm{ms}$. Thus the distribution in the figure means that $m = 0$ signals can at most include around 30 missed muons in this exposure.

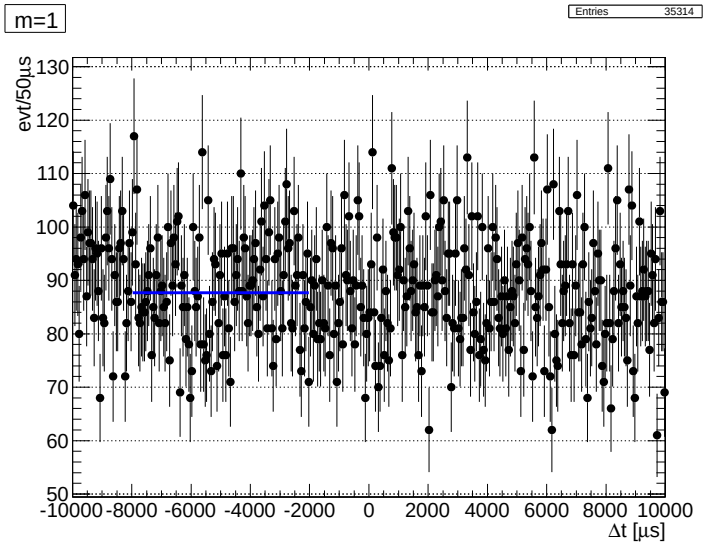

Figure 6.2: All detector coincidences for $m = 1$ muon candidates. One detector, which has a high trigger rate, is excluded in this figure. The constant line fit at about 90 events per $50\,\mu$s bin is at level with the expectation from random coincident events.

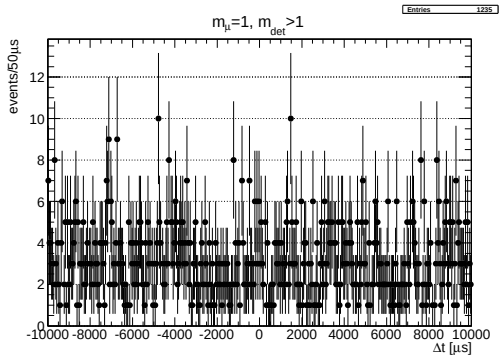

Figure 6.3: Coincidences for $m = 1$ and signals in more than one detector module.

is, however, also no indication for such $m = 1$ coincident signals, reinforcing the notion that also high energy $m = 1$ veto events are mostly not muons.

6.3 Muon coincident signals

This section covers the data sample consisting of the $\sim 6.6 \cdot 10^4$ muons ($m \geq 2$) in Run32 as defined in chapter 5, which will also be used for a comparison to previous work in section 6.4.

In figure 6.4 the muon coincident signals are shown in a Δt distribution for all detectors operated in Run32 with a chosen time window of 10 ms around the muon signal. There is a clear maximum around $\Delta t = 1\,$ms, with a steep rise starting around 0.8ms, and a tail to larger Δt, which results from low energy signals, where the detector signal onset is more difficult to determine. Even then the level of accidental coincidences in the distribution is reached at $\Delta t \approx 4\,$ms, which is used as the upper bound of the coincidence peak from here on. The blue distribution in the figure contains all available phonon detectors, which were operated in Run32, with a random coincidence level of a bit more than 3 events/50μs. One of these detectors showed a high signal rate due to higher internal lead contamination, which contributes to most of the random background in the distribution. In the red distribution

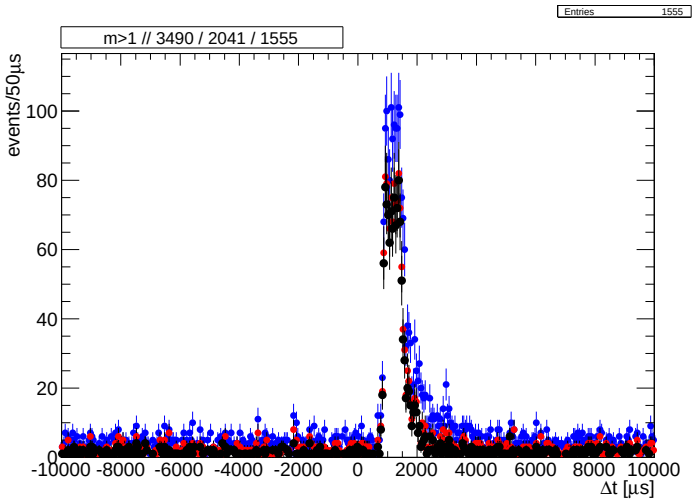

Figure 6.4: Muon-coincident event distribution in $\Delta t = [-10 \ldots 10]$ ms for all events (blue), for all detectors used in Run32 (red), and for recoil energies $\gtrsim 8$ keV (black). One of the phonon detectors, which was not used for the publication, had a high signal rate, leading to a large contribution of accidental background in the figure.

this effect is apparent, as the level decreases by more than 40% to 1.8 events/50μs, while the peak height is reduced by slightly more than 30%. A third distribution is shown in black, where only coincident signals with recoil energies in the phonon detectors larger than 8 keV are taken into account. With the removal of very low energy signals the random level is lowered further by almost 25% to 1.4 events/50μs, while the number of events in the peak is only reduced by 10%.

	random level	Events in peak
all (blue)	3.1	1827
used (red)	1.8	1226
$\gtrsim 8$ keV (black)	1.4	1114

Table 6.1: Events in peak from fig. 6.4 in the range $\Delta t = [0.75 \ldots 4]$ ms after subtracting the accidental coincidence background, as indicated. The accidental level was determined from a constant fit in the range $\Delta t = [-8 \ldots -2]$ ms.

6.3.1 Discussion and justification m≥4

In chapter 5 it was stated, that all recorded $m \geq 4$ veto events are considered as muon candidates independent of any panel threshold. As previously mentioned, with this choice the muon data set contains a contribution from 'small signal' events. These are cases, especially for the $m = 4$ class, and less so for higher multiplicities, in which each of the panels registered only a small signal with a pulseheight of only a few hundred channels, i.e. failing the muon requirement of at least two panels passing the muon threshold. But since the rate of random veto coincidences is negligible already for two-fold events, all $m \geq 4$ events are carried as muons. Most of the coincident signals are found at $\Delta t > 0$ also for the 'small signal' muon events, which means that those events do not contribute significantly to the random background in the Δt distribution. This is a clear indication that $m \geq 4$ veto signals –even when including *all* such signals– are also almost background free and do not add much to the number of random muon coincident signals, so the classification as muons is justified.

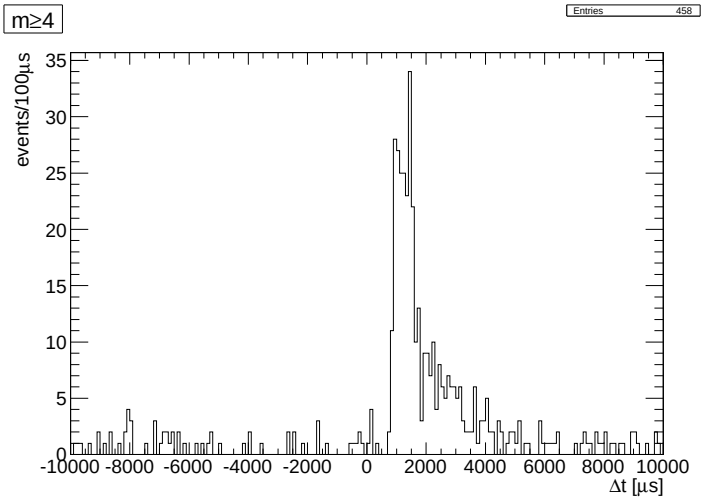

Figure 6.5: Muon coincident events for $m \geq 4$. Notice the almost background-free distribution at negative Δt. If there was substantial random contribution due to low energy veto signals, a continuous distribution would be expected here. The random level at $\Delta t < 0$ is slightly smaller than for $\Delta t > 5\,\text{ms}$, however. All detectors but the one with a high rate have been considered in this figure.

6.4 CRESST coincidences

This section is split in two parts and covers the Run32 data, which was used for the CRESST publication [56]. The first part focuses on applying the muon *cut method*, as described in section 5.3.3, which was used for the publication. In the second part the muon coincident signals removed from the published data set are re-analyzed in view of the muon definition presented in this work. Only the total number of these events is quoted in the paper and the coincident detector multiplicity is given in fig. 8 of [56]; the corresponding full data sample was provided by F. Pröbst [112] to compare with the muon selections of this work.

6.4.1 Cut method used for publication

At first the veto–detector coincident events will be determined, which result from the cut method explained in section 5.3.3, where type 1 and type 2 muon candidates are designated. Since both types yield veto safe selections, one expects a large contribution of random coincident signals in the Δt distribution. To get a better impression, a larger time window of $\pm 10\,\text{ms}$ around the muon candidate event is chosen instead of $\pm 2\,\text{ms}$ as in the publication. Due to the huge amount of data from type 1 muon candidates (see Table 6.2 with an event rate of about $4\,\text{s}^{-1}$), the analysis here is restricted to type 2 muon candidates, i.e. $m > 1$.

Figure 6.6 shows the whole resulting distribution of the time difference between coincident events for type 2 muon candidate events. At $\Delta t \approx 1\,\text{ms}$ a clear coincidence signal can be seen, and at small Δt a structure is visible in a few bins, which is the result of detector signals triggered in noise and having very small pulseheights. While the coincidence signal

	n(events)	rate	R_{rc}
type 1	$1.8 \cdot 10^8$	15600/h (4.3/s)	63/h
type 2	$3.2 \cdot 10^6$	280/h (0.08/s)	1.7/h

Table 6.2: Number and rate of type 1 and 2 muon candidates and rate as well as the expected random coincidence rate R_{rc} for an assumed detector event rate of $1s^{-1}$. These numbers were calculated for a time window of $\pm 2\,\text{ms}$ around a veto event, as quoted in [56], and for the full data set. Calculating the integral of coincident events (Fig. 6.6) in the time difference window $[-0.8 \ldots 3.2]\,\text{ms}$ adds up to close to $1.9 \cdot 10^4$, which is in good agreement to the above numbers.

is clearly visible, the overall accidental background level in the Δt distribution is twice as high as the signal, and the overall number of coincident events add up to more than $7.8 \cdot 10^4$ or $6.8\,\mathrm{h}^{-1}$, which is more than the total muon flux. Using the smaller time window of ± 2 ms as in [56] still yields 1.5 coincident signals per hour. Because the threshold on the sum trigger with a value of 200 ch is very small, this result is not surprising. A large amount of veto events of about 15 600/h (type 1) and 280/h (type 2) passes this relatively soft veto cut.

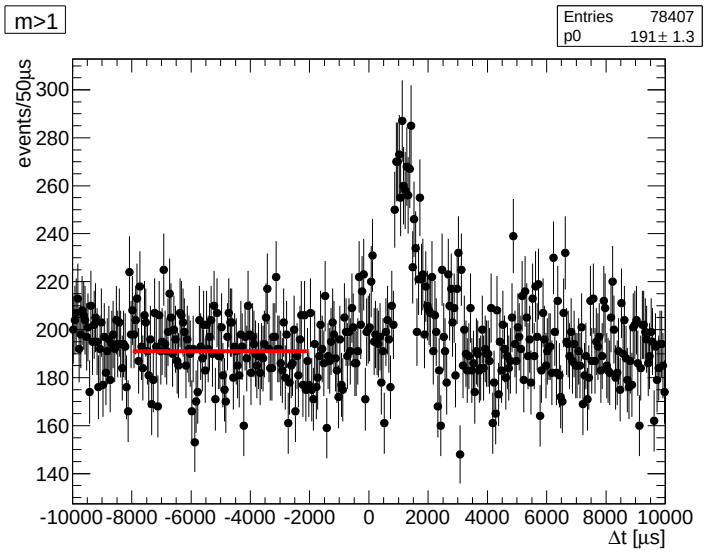

Figure 6.6: CRESST – Coincidences of all *type 2* muon candidates in a time window of ± 10 ms around the veto event with bin width $50\,\mu$s. The random coincidence level of the distribution is at ~ 191/bin, while the residual peak has just a height of ~ 90 entries. The data sample contains about $7.8 \cdot 10^4$ entries, more than the number of actual muons in Run32.

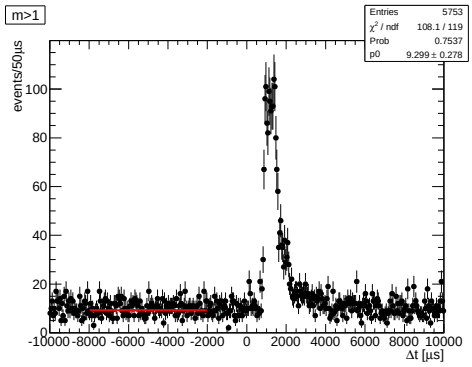

(a) sum> 1000.
The peak height remains as in the previous figure, but the accidental rate is reduced by a factor of 20, improving the signal/background from 0.5 to 10.

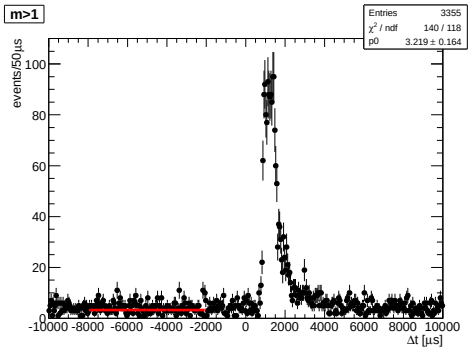

(b) sum> 2000.
The mean accidental rate is at less than 5 events/bin, similar to fig. 6.4, while the peak persists. Only $3.4 \cdot 10^3$ remain in this selection. However, a cutoff on the sum at this level can reject true muons, see fig. 6.8a.

Figure 6.7: CRESST – as in figure 6.6, but with a larger sum threshold.

In figures 6.7a and 6.7b two different arbitrary choices for a low energy sum cutoff were explored to analyze the effect of such a cutoff and to try and find an application of the cut method that yields acceptable results. Instead of the very small original value of 200 ch, in the first example a still rather small value of 1000 ch is used, followed by 2000 ch in the

second example. The effect of the first choice (sum > 1000) is already large and reduces the average accidental rate by a factor of ~20, while the signal peak height remains similar, thus improving the signal/background level by this factor.

muons	level
all	191
sum > 1000	9.3
sum > 2000	3.2

Table 6.3: Accidental coincidence level for all type 2 muon candidates and the two modifications. All numbers are per $50\mu s$ time bin. With the still rather weak condition $sum > 1000$ the background is reduced dramatically.

When the second cut (sum > 2000) is applied, the accidental level is further reduced by a factor of two to three, and the signal peak height is still similar, thus the signal/background ratio is improved dramatically compared to fig. 6.6. However, as figure 6.8a shows, such a cutoff bears the inherent danger of missing actual muon coincident signals, because the coincidence distribution visibly tails[40] to values smaller than sum=2000 ch. In this figure the Δt peak is visible as a distribution in the sum trigger parameter on the y axis. The picture also nicely demonstrates that with the CRESST-type cut the type 2 muon candidates are dominated by low pulseheight signals, while the muon coincident signals are at larger sum values.

A better discrimination of the coincidence peak can be seen in figure 6.8b, where on the ordinate the sum of the contributing panel pulseheights is shown instead of the sum parameter. Also here the low pulseheight signals dominate at a $\Sigma(panels) \lesssim 1000$, and a band-like structure in the region $[3500 \ldots 6500]$ ch can be seen, where most of the coincident muons and the accidental muon coincident events are located. This is expected and due to $m = 2$ signals, where the sum of any two most probable pulseheights is in that range, see also table 5.1.

Therefore two choices can be recommended instead of using a CRESST-type cut with sum > 200, which is too veto safe. It would be preferable to require a cutoff for the sum parameter of $\gtrsim 1000$, which reduces the amount of random coincident signals by more than an order of magnitude without losing true muon coincidences. A second, relatively simple method to discriminate true coincidences from the random background even after using the CRESST conditions has been shown in fig. 6.8b.

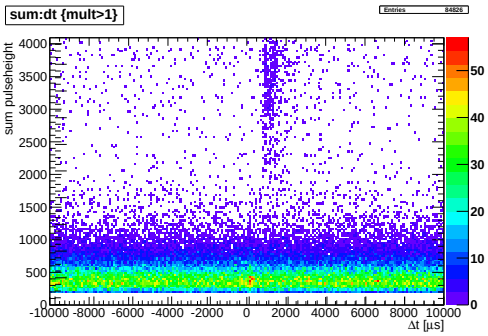

(a) Sum parameter pulseheight vs Δt. The maximum value of 4095 on the y axis is suppressed for better illustration.

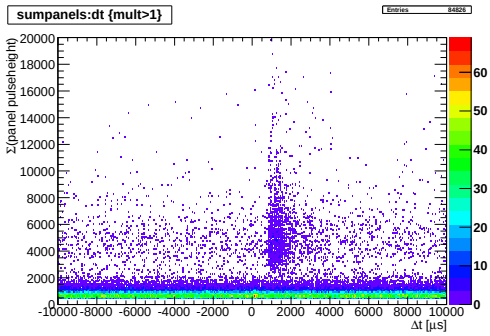

(b) Sum of panel pulseheights $\Sigma(panels)$ vs Δt. Notice the band of random coincidences at y values between 3500 and 6500ch. The number of events in the region $\Delta t = [1 \ldots 2]$ ms & $\sum(panels) > 3500$ corresponds to the results stated in sec. 6.3 and fig. 6.4.

Figure 6.8: Data sample as in figure 6.6.

[40] As noted before, the sum pulseheight can be smaller than the combined pulseheights of the panels.

6.4.2 Data set used in publication

The CRESST publication for the Run32 data [56] reports 40 muon coincident nuclear recoil signals in the region of interest ('acceptance region'), which is the recoil energy interval of $[12 \ldots 40]$ keV. This data sample, together with the coincidences in a wider energy and also in the electron recoil range is shown in fig. 6.9a and is used in this section for a posteriori tests. The validity of the muon identification in this data set will be tested.

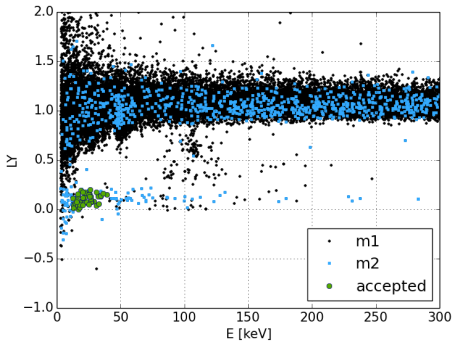

(a) Events considered as muon coincident in Run32 in [56] with the muon veto cuts as explained in section 5.3.3. Entries marked as *accepted* (green circles, both type 1 and 2) are coincident signals in the region of interest. The data for this plot was provided by F. Pröbst [112].

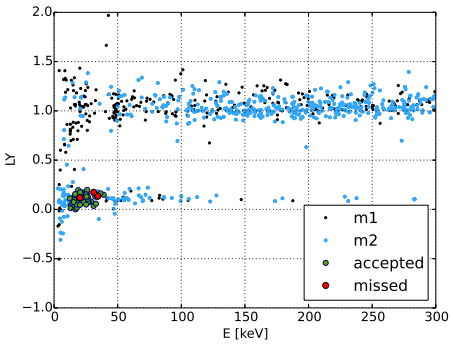

(b) Data set of publication (see left) with true muon coincidences as defined in this work. Note that the black dots are muon candidates only. The four signals marked as missed are discussed in the text.

Figure 6.9: Scatterplot of light yield vs phonon energy for recoil energies up to 300 keV.

Table 6.4 lists the number of signals for each class and type. The second column contains the number of events, where signals in multiple detectors within a time of 10 ms are considered as coincident and counted only once. The third column lists the events, which are also tagged as muon coincident with the muon definitions of chapter 5 of this work. The main conclusion form this table is that almost all of the 39 signals in the nuclear acceptance region[41], which are quoted in the publication [56], can be identified safely with a muon coincidence. Only four of the events found as muon coincident by the CRESST cut are not accepted as muon coincident by the cut in this work. Three of these events are $m = 1$ (type 1) events, and only one is designated as type 2. These four missing signals will be discussed in detail below.

Figure 6.9a shows a clear clustering of events in the electron recoil band at a recoil energy of 45-50 keV. The signals at these energies are likely from the β^- decay of ^{210}Pb, which stems from Radon contamination. This clustering is a clear hint that the data sample includes many random coincident signals, since the decay is uncorrelated to muons. In fact, only about 43% of the type 2 coincidences can be found in the muon safe data set, so less than half of these events can be safely assumed to be caused by muons, and the majority is falsely muon-tagged.

Furthermore the type 1 events are analyzed. The data sample consists of 26804 coincident type 1 events. Only a small fraction of less then 3%, or 667 events[42], can be identified as muon coincident, part of which are $m = 1$ muon candidates. Since it was already shown that the majority of these cannot be muons, the 3% fraction of identified muons is only an upper limit.

[41] There are two double and one triple detector signals in this data sample. Each is counted only once as coincident signal.

[42] ca. 60 of thos are multiple detector hits.

	class	μ candidates (w/o multiples)	found (μ safe)	found fraction
$m \geq 1$	accepted type 1	39	35	90%
	type 1	26804	667	$< 3\%$
$m > 1$	accepted type 2	29	28	97%
	type 2	955	408	43%

Table 6.4: Number of muon coincident recoil signals in Run32 as in [56, 112] with the CRESST cut. The second column lists the number of in the recoil energy range [0,300] keV corrected by multiple detector events. Only signals from the detector modules are included, which have been used for the publication. In the third column the events identified as muon-safe coincidences are listed and in the last column the fraction of positively found muons. The 'accepted type 1' class includes one triple and two double coincident detector events.

Four 'missing' type 1 / 2 accepted muons

Ordered by event date, the four events in the region of interest, which were not found as muon coincident, are analyzed individually to identify their structure and the reason they were missed in the muon safe cut used in this work:

- bck_149: 2010-01-01
  This is a triple coincident event, giving signals in three phonon/light detector modules within three milliseconds. Also, there are multiple veto events immediately (< 1 ms) preceding this triple event. Of those, the veto event with the earliest timestamp is a $m = 3$ event with a sum pulseheight of 3799 ch, but also with two small panel pulseheight contributions and only one panel pulseheight above its muon threshold, which explains why it was not designated as a muon. Within the next 1 ms there are three additional veto events, each with $m = 1$ and only a small panel pulseheight. Considering the signature this veto event could in principle originate from a crossing muon with relatively small energy deposition in the panels.
  Muon: maybe

- bck_333: 2010-09-09
  The corresponding muon data file is corrupted with an extraordinarily large file size, more than three orders of magnitude larger than comparable files. No definitive conclusion can therefore be drawn for the detector module signal, and it is recommended to discard this coincidence signal. Due to its large size, the file likely contains an excess of veto trigger events, so there is a high probability that the event is a false muon signal.
  Muon: probably no

- bck_348: 2010-09-28
  In the time window around the detector event, only one veto signal can be found, which has $m = 1$ and a low energy signal only in the *right top near* panel of 901 ch with a sum trigger value of 474 ch. Both values are unlikely to arise from a muon.
  Additionally, since the phonon detector channel has a very low noise, it can clearly be seen that its signal pulse starts about 2 ms *before* the veto signal, as shown in figure 6.10.
  Muon: no

- bck_349: 2010-09-29
  Two veto signals can be found in the vicinity of the detector signal. Both of those are $m = 1$ signals with small pulseheights of less than 800 and 700 (sum pulseheights similar), respectively, and both are in a bottom side panel. The original signal is in the Verena/Burkhard/Q module, and within 4 ms there are signals in three more phonon detectors, of which only one had a working light detector. Judging from the veto event structure this is unlikely to be a muon coincident signal.
  Muon: unlikely

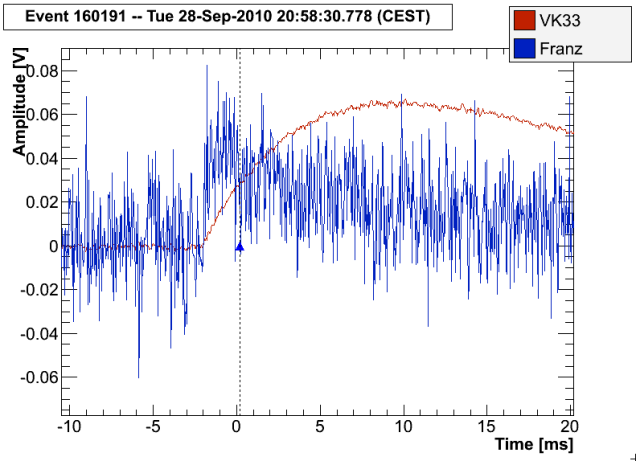

Figure 6.10: Event in bck_348, which is tagged as muon coincident and has a light/phonon detector signal in the nuclear recoil acceptance region. The blue triangle marker indicates the veto signal. Clearly the veto event occurs after the onset of the detector signal.

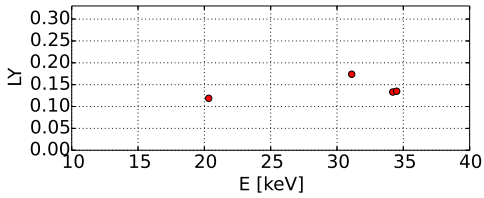

Figure 6.11: Energy and light yield of the four discussed events.

It can be argued, that at least two, likely three or all of the four signals from this list are not muon coincident. Consequently, these signals would have to be regarded as additional 'excess' events as labelled in the CRESST publication.

While the few signals referred to as muon coincident in the accepted (nuclear recoil) region could be inspected individually, such a procedure is inadequate for a larger number of signals, as for example the muon coincident type 2 events listed in table 6.4. Only less than half of the signals can be positively identified as muon coincident with the muon definition in this work.

The notes regarding the four signals show an issue of selecting the adequate veto event. For two of these events in the detector modules, clusters of veto signals around the coincidence timestamp were found. Thus it is -in a muon safe cut- important to select the correct veto event in this group of signals, which is responsible for the coincident signal. Due to the different time scales in detector module and muon veto, it may not be the best option to mark the veto event closest to a detector signal as the muon causing the detector event. Since the rate in the veto system is rather high, there is a chance that a true muon is not correctly identified.

An analysis of the 'accepted muons' (see table 6.4), which are identified as muon-safe, reveals this misclassification. Most of these events are correctly identified as type 2, and the remaining seven are classified as type 1. Only two of these seven can in fact be assigned to a $m = 1$ veto event, while the remaining coincident signals have higher true muon multiplicities, as listed in table 6.5. In fig. 6.12 one example of these events is shown, which illustrates the possible misclassification for clustering veto events. The updated histogram of the detector multiplicity distribution for the muon coincident events in the acceptance region (fig. 6.13) reveals that the four removed events have no consequence for the publication [56].

μ mult	date & remarks
6	2009-07-25
9	2009-07-27
1	2009-07-28 (sum = 3435)
4	2009-12-02 (double event)
(3)	2010-01-01 (missed #1, has a $m = 3$)
9	2010-03-31
11	2010-08-17
	2010-09-28 (missed #3, no μ, m=1)
	2010-09-29 (missed #4, no μ, m=1)
1	2011-02-18 (sum = 1222)

Table 6.5: Coincident type 1 events in the region of interest. The left column indicates the *true* multiplicity of the actual muon. See text for the details.

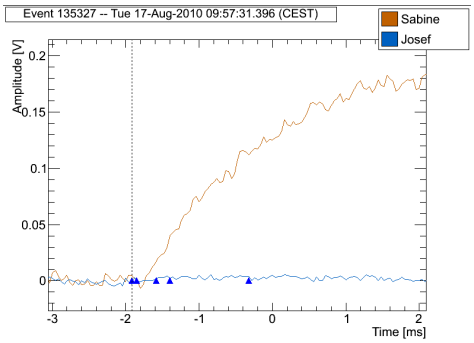

(a) Muon coincident event in a detector module. There a cluster of four veto signals within about 0.5ms at the coincidence timestamp, but only the earliest is a true muon.

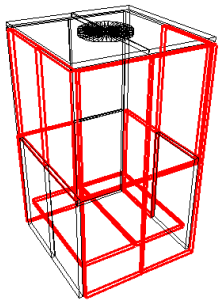

(b) The first of the cluster of veto signals preceding the detector signal shown on the left, a clear muon. The subsequent three veto events with $m = 1$ signals and small pulseheights < 1000 ch are not muons.

Figure 6.12

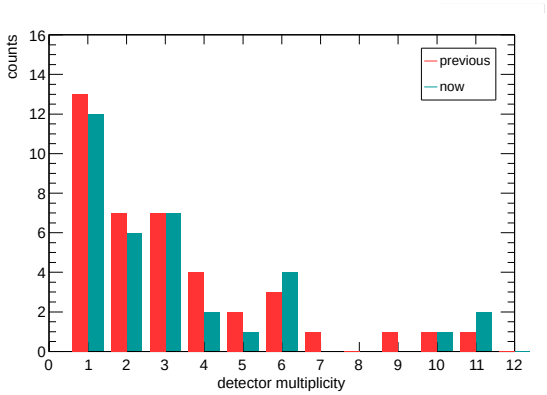

Figure 6.13: Updated detector multiplicity histogram of the muon coincident recoil signals in the acceptance region. The red histogram is the taken from [56], and the turquoise histogram is without the four events discussed in sec. 6.4.2 and one additional event due to double counting. The distribution is not changed qualitatively when removing the discussed events.

6.4.3 Background issue

The importance of a muon safe data cut was not a concern up to now for the CRESST experiment. In Run32, after considering all known sources of recoil signatures, a number of background events of unexplained origin remained in the nuclear recoil region of interest.

The result in the previous section indicate that the CRESST type 1/type 2 veto cuts are too veto safe for a real muon identification, and that up to four events have to be added to the excess background events. Assuming that this background is a contamination, which will not exist anymore in Run33 with 18 operating detector modules with a target mass of about 5 kg, it will therefore become more important to use a more muon safe cut and correctly identify muon coincident recoil events.

6.5 Muon fraction creating a coincident signal in the modules

Overall, the number of muons in Run32 is about $6.6 \cdot 10^4$ with the data selections developed in chapter 5, which is the equivalent of a muon flux of about six per hour. The fraction of muons, which in reality create a coincident signal in the detector modules, is much lower than that. Table 6.6 shows that higher multiplicity muons are more likely to induce a signal in the $CaWO_4$ modules. In the last column of the table one phonon detector is excluded, which has a large intrinsic activity, thus contributing excessively to the coincidence rate.

The numbers in the table show nicely that higher veto multiplicity muons are more likely to create a signal in the detector modules, as one would intuitively expect. For the more abundant muons with $m = 2$ and $m = 3$ about one in $30 - 40$ muons has a coincident signal in at least one detector module within a realistic time span of up to 4 ms. Higher veto multiplicity muons are much less abundant, but nevertheless the trend is clear that each 10th to 20th of these muons induces a signal in the detector modules.

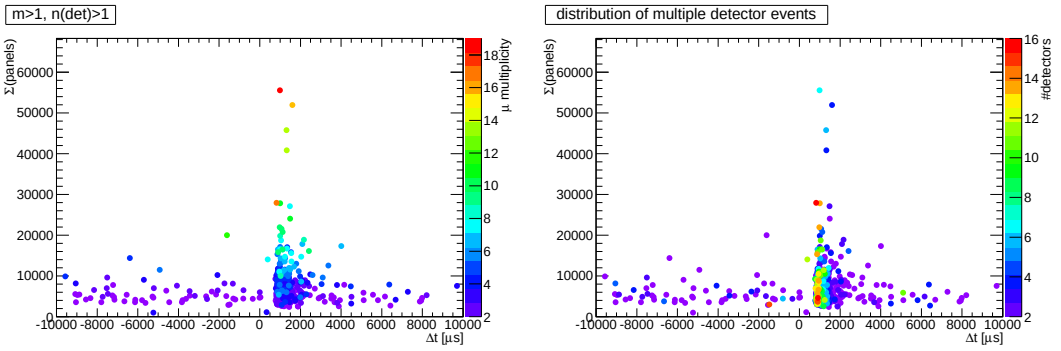

(a) Most high multiplicity muons with coincident detector signals are in the peak region. For a better illustration, only multiple detector events are shown. The color code represents the muon multiplicity, the y axis the sum of panel pulseheights.

(b) Most muons with more than one detector (color scale) containing a signal can be found in the coincidence peak region. The y axis indicates the sum of the panel pulseheights.

Figure 6.14

6.6 Summary μ coincident signals

Two different muon cut setups have been investigated with regard to coincident events between the muon veto and the detector modules: the first is the method developed in this work, a muon safe approach. The second uses a veto safe method and was used as such in the CRESST publication [56] for Run32.

An important statement is that no coincidence peak can be seen in either setup for the $m = 1$ muon candidates. On the other hand the time coincidence figures nicely show that muons are predominantly of the $m > 1$ kind, illustrated by the almost background-free signature in fig. 6.4. This is another demonstration that the proposed muon definition is properly identifying muons.

μ mult	number of μ	coincidences within $[0, 4]$ ms	fraction [%]
1	1462443	4775	0.3
2	41808	955	2.3
3	14819	458	3.1
4	6088	162	2.7
5	1630	73	4.5
6	698	45	6.5
7	320	20	6.3
8	163	14	8.6
9	95	7	7.4
10	61	6	9.8
> 10	110	12	10.9

Table 6.6: Muons with coincident detector signals, ordered by muon multiplicity. The $m = 1$ candidates are listed for completeness. For $m > 10$ the muons were grouped due to low statistics. On average for $m = 1$ only one in 300 muon candidates creates a coincident detector signal. This fraction increases rapidly for $m > 1$, and for higher multiplicities about each 10th muon induces signals in the modules.

Further confirmation comes from the m=0 signals, which as described contain mostly low energy signals. From these events no coincidence peak is expected, which is confirmed and shown in fig. 6.1. It was also shown that higher veto multiplicity muons are more likely to cause a coincident signals compared to muons with lower multiplicity, which is evident in fig. 6.14a. Likewise, most multiple detector signals in coincidence with a muon are centered around the coincidence peak as demonstrated in fig. 6.14b.

The two approaches lead to a difference in the number of muon coincident signals in the dark matter search region of 5-10%. In the case that an excess in the background data is found, this has to be kept in mind, because with the veto safe approach the majority of veto–cryo signals are false coincidences not caused by muons. However, it can also be stated that with the veto safe selection 90% of the muon coincident nuclear recoils were positively identified with muons.

Conclusions & Outlook

The primary focus of this work was on the muon veto data for the CRESST experiment. First, the operational stability was examined, and several issues in the background Runs 30, 31 and 32 were discovered and analyzed. This resulted in the suggestion of several parameters of the veto system suitable for data monitoring in the short and long term to quickly discover deviations from the norm.

After that, a realistic definition of muons for a *muon-safe* selection in the veto was presented and compared to other methods. This data selection can be done in a robust and automatic way, requiring only a relatively small statistical sample of about 1–3 months, which marks an improvement on previous work. The resulting muon rate of about 6 h^{-1} is in very good agreement with the expectation from the muon depth-intensity relation and results from other experiments, and is not influenced by the stability issues like the rate jumps in single panels. Also the muon count rates in the different types of panels, horizontal and vertical, reveal the expected characteristics, confirming the muon selection process.

Subsequently, muon coincident signals in the detector modules of CRESST were analyzed with for the resulting muon data sample and also for the data cut used in the CRESST experiment in Run32. No coincidence peak could be found for single panel hit muon candidates, which confirms that only very few muons can be expected in this category. Muons with a multiplicity > 1, on the other hand, show a clear coincidence signal with only a small contribution of random coincident background. In Run32, about 0.1 muon coincident events per hour were found.

Furthermore, the muon coincident signals in the CRESST results were discussed, and about 90 % of the signals could be confirmed as true muons. The selection method proved to be too veto safe, and ~10 % of the rejected coincident events in the acceptance region could not be identified as muons with the muon safe cut, which slightly increases the number of excess events in CRESST. A discussion is therefore in order, if a more veto safe or a more muon safe cut method should be used. While the veto safe cut can safely reject all possible muons, the deadtime is increased. A muon safe cut allows to analyze the influence of muons on the detector modules, which was useful for the excess events in Run32.

Possible improvements

Two types of improvements can be considered for the CRESST muon veto: the first is to modify the DAQ settings and readout procedure, which does not require major changes, while the second would involve hardware upgrades.

The issues of zero multiplicity events could be resolved as previously discussed in the text by triggering on each panel and removing the readout suppression. This would increase the amount of recorded data a lot, but simplifies monitoring. Near-threshold problems of $m = 0$ and $m = 1$ signals can then be avoided. In Run33 these items are already considered, and with modified settings the event rate is about five times higher than during Run32.

A second type of improvement would be a hardware upgrade to the current setup. In the current veto setup, it is not possible to reliably detect single hit muons due to the hole in the setup for the cryostat. These signals only amount to a few percent of the total flux, but the muons creating such signals can pass through the experiment very close to the target crystals. A solution can be installing a layer of scintillator panels either as close as possible above the cryostat or on top of the CRESST experiment building. Further upgrades would require major changes. For example it would be desirable to have at least two photomultipliers for

each scintillator panel or thin multi-layer scintillator panels instead of the single large-area panels currently installed, which could facilitate a faster muon identification or monitoring, and possibly also provide a directional information.

A

Veto references

A.1 General information

The data sheets and information about the scintillator material are shown in figs. A.1 and A.2.

A.2 Previous Run30 muon threshold values

The set of muon threshold values for Run30 quoted from [102] is listed in table A.1. The width is the σ parameter of the fit.

#	panel	threshold	mpv	width (σ)	#	panel	threshold	mpv	width (σ)
1	cl	1561	2154	237	3	fl	1555	2121	226
2	cr	2265	2970	282	4	fr	1299	1881	232
5	ftr	1106	2307	480	13	btl	1012	2615	641
6	ftl	1214	2756	616	14	btr	896	2479	633
7	fbr	656	2515	743	15	bbl	1029	2405	550
8	fbl	807	2677	747	16	bbr	904	1677	309
9	rtf	1088	2082	397	17	ltn	1024	1894	348
10	rtn	1124	2672	619	18	ltf	695	2052	542
11	rbf	1343	2034	276	19	lbn	1034	1931	358
12	rbn	1535	2347	324	20	lbf	158	1536	551
Values are in [ch]									

Table A.1: Threshold values for Run30 from [102].

BC-400,BC-404,BC-408,BC-412,BC-416
Premium Plastic Scintillators

The premium plastic scintillators described in this data sheet include those with the highest light output, as well as the most economical (BC-416). The chart below will direct you to the scintillator suitable for your energy application.

Radiation Detected	BC-400	BC-404	BC-408	BC-412	BC-416
<100keV X-rays			X		
100keV to 5MeV gamma rays				X	
>5MeV gamma rays	X				X
Fast neutrons				X	X
Alphas, betas		X	X		
Charged particles,cosmic rays, muons, protons, etc.			X	X	X
Principal Uses/Applications	general purpose	fast counting	TOF large area	large area	large area economy

Scintillation Properties –	BC-400	BC-404	BC-408	BC-412	BC-416
Light Output, %Anthracene	65	68	64	60	38
Rise Time, ns	0.9	0.7	0.9	1.0	–
Decay Time (ns)	2.4	1.8	2.1	3.3	4.0
Pulse Width, FWHM, ns	2.7	2.2	~2.5	4.2	5.3
Wavelength of Max. Emission, nm	423	408	425	434	434
Light Attenuation Length, cm*	160	140	210	210	210
Bulk Light Attenuation Length, cm	250	160	380	400	400
Atomic Composition –					
No. H Atoms per cc ($x10^{22}$)	5.23	5.21	5.23	5.23	5.25
No. C Atoms per cc ($x10^{22}$)	4.74	4.74	4.74	4.74	4.73
Ratio H:C Atoms	1.103	1.100	1.104	1.104	1.110
No. of Electrons per cc ($x10^{23}$)	3.37	3.37	3.37	3.37	3.37

*The typical 1/e attenuation length of a 1x20x200cm cast sheet with edges polished as measured with a bialkali photomultiplier tube coupled to one end.

General Technical Data –

Base ..... Polyvinyltoluene

Density (g/cc) ..... 1.032 g/cc

Refractive Index 1.58

Expansion Coefficient (per°C,<67°C): $7.8X10^{-5}$

Softening Point ..... 70°C

Vapor Pressure ..... May be used in vacuum

Solubility ..... Soluble in aromatic solvents, chlorinated solvents, acetone, etc. Unaffected by water, dilute acids, lower alcohols, alkalis and pure silicone fluids or grease.

Light Output ..... At +60°C = 95% of that at+20°C. Independent of temperature from -60°C to +20°C

SAINT-GOBAIN
CRYSTALS

Figure A.1: Saint Gobain / Bicron BC-408 plastic scintillator data sheet (1).

BC-400,BC-404,BC-408,BC-412,BC-416
Premium
Plastic Scintillators

Emission Spectra

BC-400

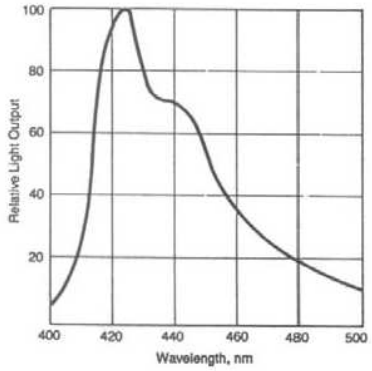

BC-408

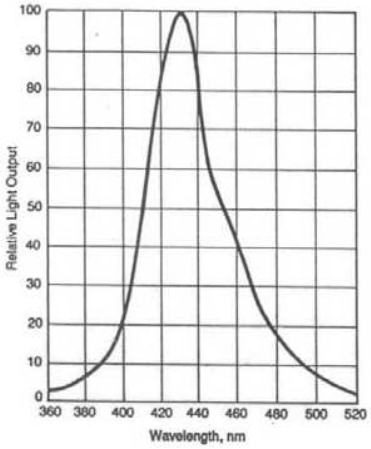

BC-404

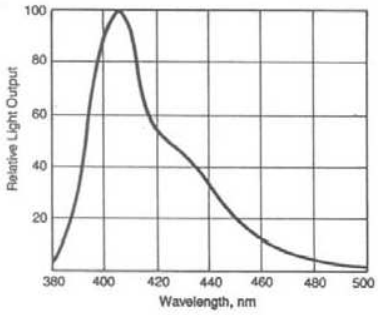

BC-412 & BC-416

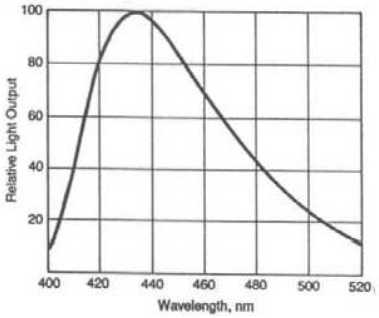

Premium Plastic Scintillators
Response to Atomic Particles

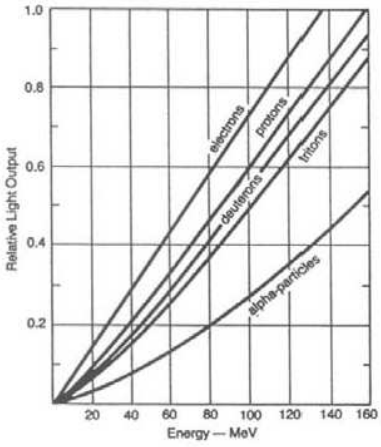

Range of Atomic Particles in
Premium Plastic Scintillators

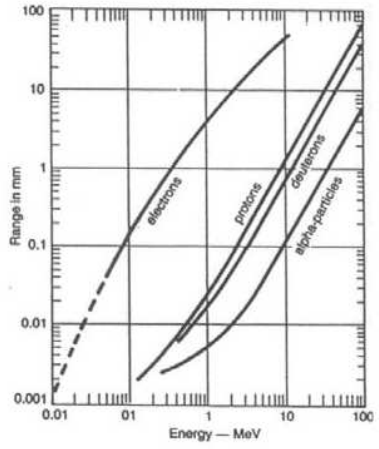

Manufacturer reserves the right to alter specifications.

(07-08)

Figure A.2: Saint Gobain / Bicron BC-408 plastic scintillator data sheet (2).

B

Panel rate pictures

For completeness the figures with the single panel signal rates are shown here in an overview. Each figure shows the rate per hour against the timestamp on the x axis.

Rate picture layout

figure 1			figure 2	
cl	cr		rbf	rbn
fl	fr		btl	btr
ftr	ftl		bbl	bbr
fbr	fbl		ltn	ltf
rtf	rtn		lbn	lbf

Table B.1: Panel order in figs. B.1–B.3. Abbreviations as listed in table 3.3.

Run32

The mean rates vary between ∼130 (#15-*back bottom left*) and ∼4500 (#3-*floor left*) h^{-1} with strongly varying patterns. The most notable issue is visible in the fourth figure in the left column of fig. B.1a, which is panel #7-*front bottom right*.

Run31

During the second quarter of the measurement period a rise of the rates shows up in almost all detectors. The top two rows in fig. B.2a include the ceiling and floor panels, all others are side panels. In fig. B.2b the last panel in the right column (#20-*left bottom far*) shows a significant drop in the event rate in the first quarter of the Run within one data file, but recovers after a few days to the original level.

Run30

Apart from minor differences all detectors have the same behavior, namely a strongly decreasing event rate during the measurement period. Pauses in the period often go along with a discontinuous rate level, but the overlying trend is a linear decrease by a similar factor until the end of the Run. There are huge variations in the trigger rates with a maximum of 15000 events/h in #3-*floor left*, while the #18-*left top far* (next figure) barely reaches 100/h.

The last panel in the right column (#20-*left bottom far*) of fig. B.3b shows a sharp drop in the event rate after the first quarter of the Run, but later recovers and readjusts to the original trend. This is noteworthy, since the same panel also has issues in other Runs. As in Runs 32 and 31, the #18-*left top far* panel has the lowest event rate.

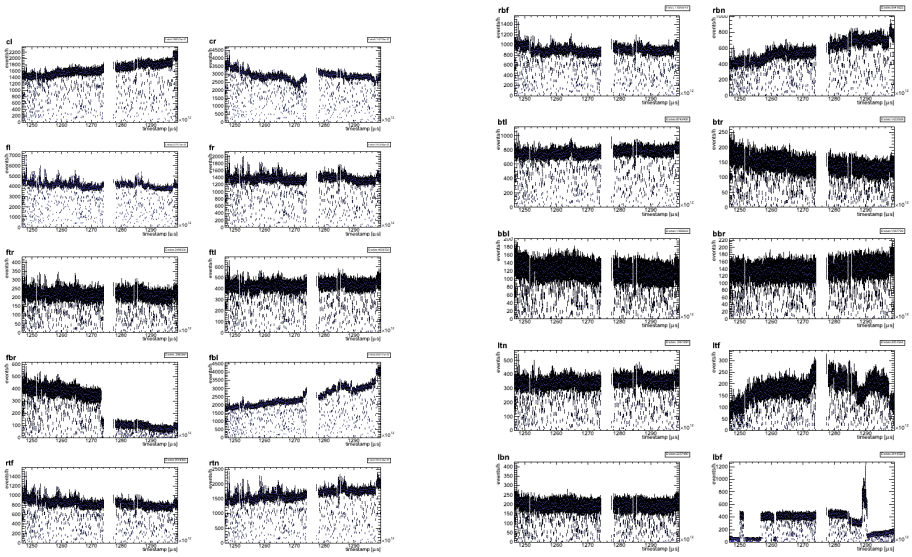

(a) Panels 1-10. **(b)** Panels 11-20.

Figure B.1: Run32: signal rate [h^{-1}] evolution.

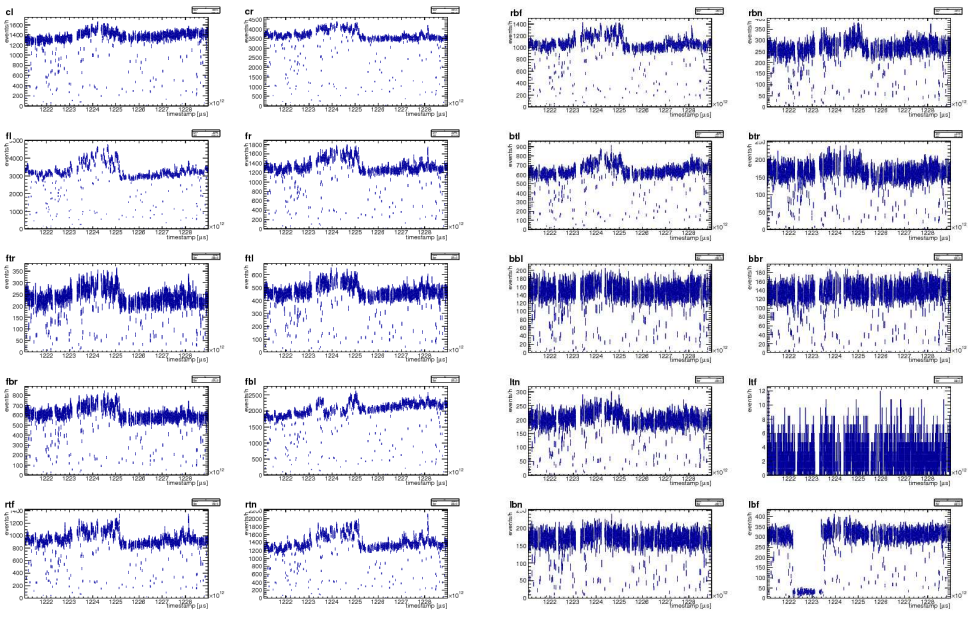

(a) Panels 1-10. **(b)** Panels 11-20.

Figure B.2: Run31: signal rate [h^{-1}] evolution. The mean rates vary in a similar range compared to fig.s B.1a and B.1b, except for #18-*left top far* and #20-*left bottom far*.

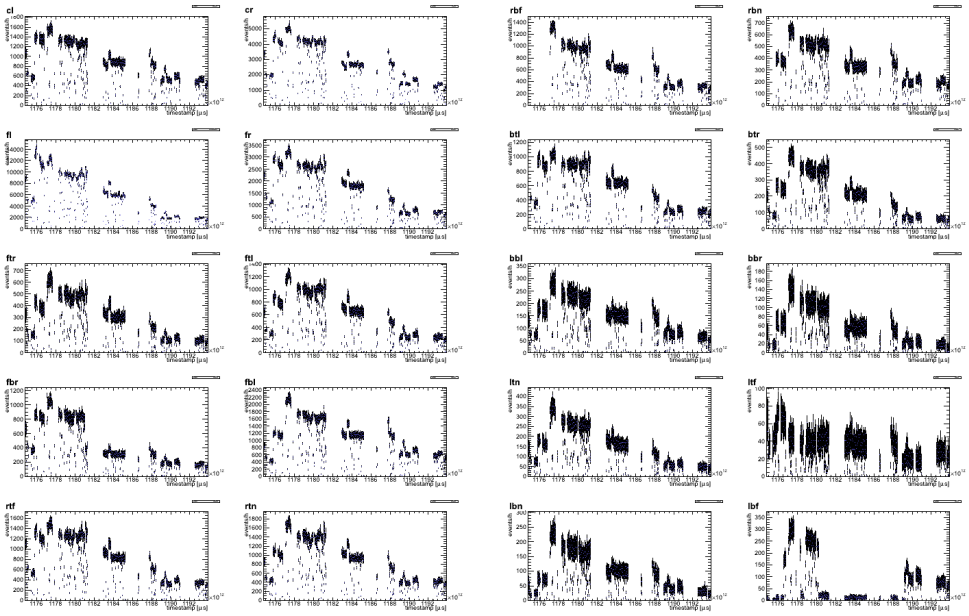

(a) Panels 1-10. **(b)** Panels 11-20.

Figure B.3: Run30: signal rate [h^{-1}] evolution.

C

Notes & Abbreviations

C.1 Note on timestamps

In oxRop the timestamps are registered in the software in the following way [113, 114]:
The CRESST DAQ produces a Unix 32 bit timestamp for the begin and the end of a data file, which is written into a text file together with other information. There the Unix time in seconds and microseconds is saved as two different numbers each for the start and stop of writing to disk. These values are fixed values also in oxRop. A difference arises in the handling of event times within the data files. The Unix time of a computer is not a very good measure to relate events with each other, but provides the general long-term time indexing (synchronisation). To achieve the short-term relation between events, the 10 MHz DAQ clock installed at the experiment gives a better measure. At each start of a new data file, the DAQ clock and the computer time are assumed to be synchronized. Since the DAQ clock can be off by up to a few seconds per day, a fit to the data from start to end of a file is performed.

Remark on timestamp handling for comparison

The analysis software packages used in CRESST use a slightly different handling of the events and their timestamps, which can result in a small time difference between the signals. This issue was resolved by a comparison script with a very generous overlap time of at least one second between the events in the data sample used in the publication and the timestamps in the oxRop software. In all randomly tested examples the timestamp difference of both methods was less than 1 ms. Nevertheless, to be conservative the data were checked for signals within one second around each event. It is therefore safe to assume that all possible coincident events are included in either data sample. The tested data sets also showed that almost all events were within this time window.

C.2 Muons from the CNGS beam

In the muon data of the GERDA experiment a discrepancy of $\mathcal{O}(1\%)$ between expected and measured muon flux was found in the annual modulation analysis [115]. The CNGS muon neutrino beam, which has been used by the OPERA experiment to search for τ neutrino appearance, was found as the reason for the discrepancy. Consequently muons resulting from the CNGS neutrino beam can also be expected in the CRESST muon veto. As the absolute time calibration in CRESST is not provided by a GPS clock, an offset in the timestamps can be expected, so the muons of Run32 were analyzed with a time window of several seconds around the beam bunches. The timestamp data for the beam bunches was kindly provided by [116].

A small fraction of the Run32 muons was found to be coincident with the CNGS data. Even with the limited angular resolution of the CRESST muon veto, a number of muons could be clearly identified as originating from the CNGS beam. To this end, only muons with exactly two panel hits were selected, in which the signals occurred in opposing side walls. Thus it is possible to select only muons crossing the veto setup. As the LNGS halls are aligned towards the CERN, the 'front/back' walls of the muon veto are in beam direction, while the 'left/right' walls are orthogonal. The figures show the Δt coincidence distribution[43] first for all muons in figure C.1 with a large time window showing the flat random background, and then for the two selections 'front/back' and 'left/right' in a time window of $\pm 1\,\mathrm{s}$ around a CRESST muon (fig. C.2a). Clearly there is a coincidence signal in the CNGS beam direction, while the distribution in orthogonal direction is flat. The sum of the panel pulseheight of the CNGS coincident muons is on average at towards lower pulseheights, because the muons arrive almost horizontally and have a shorter path in the scintillator.

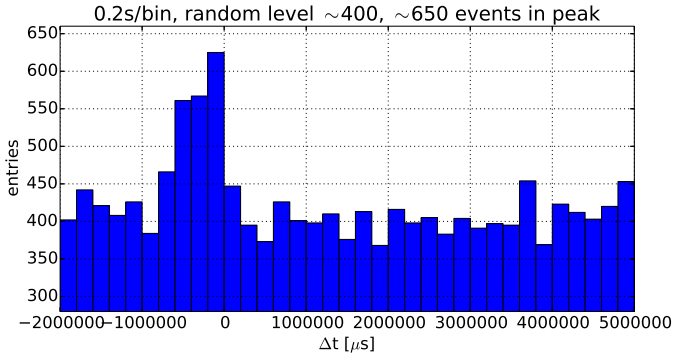

Figure C.1: Coincidences between the CNGS beam bunches and the CRESST muons with a time window of $[-2, 5]\,\mathrm{s}$.

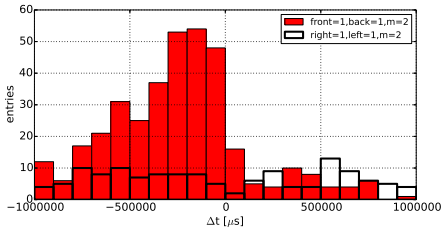

(a) CNGS coincident $m = 2$ muons in beam direction and perpendicular to beam.

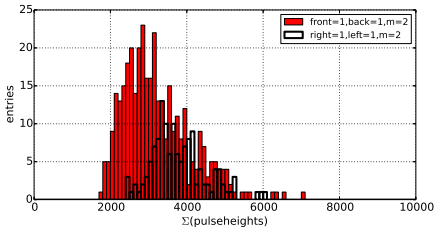

(b) Sum of panel pulseheights of $m = 2$ front/back and left/right muons.

Figure C.2

[43] Negative Δt indicates that the CNGS beam timestamp occured prior to the CRESST muon.

Abbreviations

ADC	Analog to Digital Converter
CDM	Cold Dark Matter
CERN	Conseil Européen pour la Recherche Nucléaire (European Council for Nuclear Research)
CMB	Cosmic Microwave Background
CR	Cosmic Rays
CRESST	Cryogenic Rare Event Search with Superconducting Thermometers
DAQ	Data Acquisition (system)
DE	Dark Energy
DM	Dark Matter
ΛCDM	Cosmological Standard Model
GZK	Greisen-Zatsepin-Kuzmin
LHC	Large Hadron Collider
LNGS	Laboratori Nazionali del Gran Sasso
(c)MSSM	(constrained) Minimal Supersymmetric Standard Model
m.w.e.	meters of water equivalent
PE	Polyethylen
PMT	Photomultiplier Tube
QDC	Charge to Digital Converter
SM	Standard Model of Particle Physics
SPT	Superconducting Phase Transition Thermometer
SUSY	Supersymmetry
TES	Transition Edge Sensor, see → **SPT**
UHECR	Ultra High Energy Cosmic Rays
WIMP	Weakly Interacting Massive Particle

Note: particle masses are given in energy units.

List of Figures

List of Tables

Bibliography

[1] Hesti R. T. Wulandari. *Study On Neutron-Induced Background in the Dark Matter Experiment CRESST*. PhD thesis, Technische Universität München, 2003.

[2] S. Scholl. *Neutron Background Simulation for the CRESST - II Experiment*. PhD thesis, Universität Tübingen, 2011.

[3] M. Bauer. *Study of Muon-Induced Background in Direct Dark Matter and Other Rare Event Searches*. PhD thesis, Universität Tübingen, 2012.

[4] E. Kolb and M. Turner. *The Early Universe*. Frontiers in physics. Westview Press, 1994.

[5] A. A. Penzias and R. W. Wilson. A Measurement of Excess Antenna Temperature at 4080 Mc/s. *Astrophys.J.*, 142:419–421, July 1965.

[6] J. Beringer et al. The Review of Particle Physics. *Phys. Rev.*, D86:010001, 2012.

[7] P.A.R. Ade et al. Planck 2013 results. XVI. Cosmological parameters. *Phys. Rev. Lett.*, 2013.

[8] S. Perlmutter et al. Measurements of Omega and Lambda from 42 high redshift supernovae. *Astrophys.J.*, 517:565–586, 1999.

[9] Adam G. Riess et al. Observational evidence from supernovae for an accelerating universe and a cosmological constant. *Astron.J.*, 116:1009–1038, 1998.

[10] J.H. Oort. The force exerted by the stellar system in the direction perpendicular to the galactic plane and some related problems. *Bull. Astron. Inst. Neth.*, 6:249–287, 1932.

[11] F. Zwicky. Spectral displacement of extra galactic nebulae. *Helv.Phys.Acta*, 6:110–127, 1933.

[12] F. Zwicky. On the Masses of Nebulae and of Clusters of Nebulae. *Astrophys. J.*, 86:217–246, October 1937.

[13] V. C. Rubin and W. K. Ford, Jr. Rotation of the Andromeda Nebula from a Spectroscopic Survey of Emission Regions. *Astrophys. J.*, 159:379, February 1970.

[14] V. C. Rubin et al. Rotation velocities of 16 SA galaxies and a comparison of Sa, Sb, and SC rotation properties. *Astrophys. J.*, 289:81–98, February 1985.

[15] M. Arik et al. Search for Sub-eV Mass Solar Axions by the CERN Axion Solar Telescope with ^{3}He Buffer Gas. *Phys. Rev. Lett.*, 107:261302, Dec 2011.

[16] T.S. van Albada, John N. Bahcall, K. Begeman, and R. Sancisi. The Distribution of Dark Matter in the Spiral Galaxy NGC-3198. *Astrophys.J.*, 295:305–313, 1985.

[17] J. F. Navarro, C. S. Frenk, and S. D. M. White. The Structure of Cold Dark Matter Halos. *Astrophys. J.*, 462:563, May 1996.

[18] D. Clowe, A. Gonzalez, and M. Markevitch. Weak lensing mass reconstruction of the interacting cluster 1E0657-558: Direct evidence for the existence of dark matter. *Astrophys. J.*, 604:596–603, 2004.

[19] M. Milgrom. A modification of the Newtonian dynamics as a possible alternative to the hidden mass hypothesis. *Astrophys. J.*, 270:365–370, July 1983.

[20] D. Clowe et al. A direct empirical proof of the existence of dark matter. *Astrophys. J.*, 648:L109–L113, 2006.

[21] Gerard Jungman, Marc Kamionkowski, and Kim Griest. Supersymmetric dark matter. *Phys.Rept.*, 267:195–373, 1996.

[22] Gianfranco Bertone, Dan Hooper, and Joseph Silk. Particle dark matter: Evidence, candidates and constraints. *Phys.Rept.*, 405:279–390, 2005.

[23] Richard J. Gaitskell. Direct detection of dark matter. *Annual Review of Nuclear and Particle Science*, 54(1):315–359, 2004.

[24] Dan Hooper and Edward A. Baltz. Strategies for determining the nature of dark matter. *Annual Review of Nuclear and Particle Science*, 58(1):293–314, 2008.

[25] Frank Daniel Steffen. Dark Matter Candidates - Axions, Neutralinos, Gravitinos, and Axinos. *Eur.Phys.J.*, C59:557–588, 2009.

[26] L. Bergström and A. Goobar. *Cosmology and Particle Astrophysics*. Springer Praxis Books / Astronomy and Planetary Sciences. Praxis Publ., 2006.

[27] Georg G. Raffelt. Astrophysical axion bounds. *Lect.Notes Phys.*, 741:51–71, 2008.

[28] J.D. Lewin and P.F. Smith. Review of mathematics, numerical factors, and corrections for dark matter experiments based on elastic nuclear recoil. *Astropart.Phys.*, 6:87–112, 1996.

[29] Richard H. Helm. Inelastic and elastic scattering of 187-mev electrons from selected even-even nuclei. *Phys. Rev.*, 104:1466–1475, Dec 1956.

[30] A. Drukier and L. Stodolsky. Principles and applications of a neutral-current detector for neutrino physics and astronomy. *Phys. Rev. D*, 30:2295–2309, Dec 1984.

[31] Mark W. Goodman and Edward Witten. Detectability of certain dark-matter candidates. *Phys. Rev. D*, 31:3059–3063, Jun 1985.

[32] S. Burgos et al. Measurement of the Range Component Directional Signature in a DRIFT-II Detector using Cf-252 Neutrons. *Nucl.Instrum.Meth.*, A600:417–423, 2009.

[33] S. J. Asztalos et al. SQUID-Based Microwave Cavity Search for Dark-Matter Axions. *Phys. Rev. Lett.*, 104:041301, Jan 2010.

[34] E. Zavattini et al. Experimental Observation of Optical Rotation Generated in Vacuum by a Magnetic Field. *Phys. Rev. Lett.*, 96:110406, Mar 2006.

[35] E. Zavattini et al. Editorial Note: Experimental Observation of Optical Rotation Generated in Vacuum by a Magnetic Field [Phys. Rev. Lett. 96, 110406 (2006)]. *Phys. Rev. Lett.*, 99:129901, Sep 2007.

[36] E. Zavattini et al. New PVLAS results and limits on magnetically induced optical rotation and ellipticity in vacuum. *Phys. Rev. D*, 77:032006, Feb 2008.

[37] Raúl Rabadán, Andreas Ringwald, and Kris Sigurdson. Photon Regeneration from Pseudoscalars at X-Ray Laser Facilities. *Phys. Rev. Lett.*, 96:110407, Mar 2006.

[38] C. Robilliard et al. No "Light Shining through a Wall": Results from a Photoregeneration Experiment. *Phys. Rev. Lett.*, 99:190403, Nov 2007.

[39] W. de Boer, C. Sander, V. Zhukov, A.V. Gladyshev, and D.I. Kazakov. Egret excess of diffuse galactic gamma rays as tracer of dark matter. *Astron.Astrophys.*, 444:51, 2005.

[40] Oscar Adriani et al. An anomalous positron abundance in cosmic rays with energies 1.5-100 GeV. *Nature*, 458:607–609, 2009.

[41] O. Adriani et al. PAMELA results on the cosmic-ray antiproton flux from 60 MeV to 180 GeV in kinetic energy. *Phys.Rev.Lett.*, 105:121101, 2010.

[42] Fermi-LAT Collaboration. Search for Gamma-ray Spectral Lines with the Fermi Large Area Telescope and Dark Matter Implications. *preprint*, 2013.

[43] Christoph Weniger. A Tentative Gamma-Ray Line from Dark Matter Annihilation at the Fermi Large Area Telescope. *JCAP*, 1208:007, 2012.

[44] M.G. Aartsen et al. Search for dark matter annihilations in the Sun with the 79-string IceCube detector. *Phys. Rev. Lett.*, 110:131302, Mar 2013.

[45] R. Bernabei, P. Belli, F. Montecchia, W. Di Nicolantonio, A. Incicchitti, et al. Searching for WIMPs by the annual modulation signature. *Phys.Lett.*, B424:195–201, 1998.

[46] R. Bernabei et al. On a further search for a yearly modulation of the rate in particle dark matter direct search. *Phys.Lett.*, B450:448–455, 1999.

[47] R. Bernabei et al. Search for WIMP annual modulation signature: Results from DAMA /NaI-3 and DAMA/NaI-4 and the global combined analysis. *Phys.Lett.*, B480:23–31, 2000.

[48] R. Bernabei et al. New results from DAMA/LIBRA. *Eur. Phys. J.*, C67:39–49, 2010.

[49] R Bernabei et al. Dama/libra results and perspectives. *Journal of Physics: Conference Series*, 375(1):012002, 2012.

[50] R. Bernabei et al. Final model independent result of DAMA/LIBRA-phase1. *The European Physical Journal C*, 73(12):1–11, 2013.

[51] C. E. Aalseth et al. Results from a search for light-mass dark matter with a p-type point contact germanium detector. *Phys. Rev. Lett.*, 106:131301, Mar 2011.

[52] C. E. Aalseth et al. Search for an annual modulation in a p-type point contact germanium dark matter detector. *Phys. Rev. Lett.*, 107:141301, Sep 2011.

[53] J. I. Collar, 2012. Talk at IDM2012.

[54] R. Agnese et al. Silicon Detector Results from the First Five-Tower Run of CDMS II. *Phys.Rev.*, D88:031104, 2013.

[55] R. Agnese et al. Silicon Detector Dark Matter Results from the Final Exposure of CDMS II. *Phys.Rev.Lett.*, 2013.

[56] G. Angloher et al. Results from 730 kg days of the CRESST-II Dark Matter search. *The European Physical Journal C*, 72(4):1–22, 2012.

[57] D.S. Akerib et al. First results from the LUX dark matter experiment at the Sanford Underground Research Facility. *arXiv preprint*, 2013. arXiv:1310.8214 [astro-ph.CO].

[58] Rick Gaitskell and Dan McKinsey. First Science Results from the LUX Dark Matter Experiment. Talk at Sanford Underground Research Facility, Oct. 30, 2013. available online at `http://luxdarkmatter.org/talks/20131030_LUX_First_Results.pdf`.

[59] Gaitskell, R. and Mandic, V. and Filippini, J and Speller, C. Dark matter limit plot generator, 2013. see `http://cedar.berkeley.edu/plotter`.

[60] T.K. Gaisser. *Cosmic Rays and Particle Physics*. Cambridge University Press, 1991.

[61] J. Abraham et al. Observation of the suppression of the flux of cosmic rays above 4×10^{19} eV. *Phys. Rev. Lett.*, 101:061101, Aug 2008.

[62] J. Abraham et al. Measurement of the energy spectrum of cosmic rays above 10^{18} eV using the Pierre Auger Observatory. *Phys.Lett.*, B685:239–246, 2010.

[63] R.U. Abbasi et al. First observation of the Greisen-Zatsepin-Kuzmin suppression. *Phys.Rev.Lett.*, 100:101101, 2008.

[64] P. Sokolsky. Final results from the High Solution Fly's Eye (HiRes) experiment. *Nucl.Phys.Proc.Suppl.*, 212-213:74–78, 2011.

[65] M Takeda et al. Energy determination in the Akeno Giant Air Shower Array experiment. *Astropart.Phys.*, 19:447–462, 2003.

[66] James W. Cronin, Thomas K. Gaisser, and Simon P. Swordy. Cosmic Rays at the Energy Frontier. *Scientific American*, January 1997.

[67] S. Longair. *High Energy Astrophysics: Volume 2, Stars, the Galaxy and the Interstellar Medium.* Cambridge University Press, 1994.

[68] M. Ambrosio et al. Vertical muon intensity measured with MACRO at the Gran Sasso laboratory. *Phys. Rev. D*, 52:3793–3802, Oct 1995.

[69] M. Ambrosio et al. High energy cosmic ray physics with underground muons in MACRO. I. Analysis methods and experimental results. *Phys. Rev. D*, 56:1407–1417, Aug 1997.

[70] M. Ambrosio et al. High energy cosmic ray physics with underground muons in macro. ii. primary spectra and composition. *Phys. Rev. D*, 56:1418–1436, Aug 1997.

[71] M. Aglietta et al. Muon "depth-intensity" relation measured by the LVD underground experiment and cosmic-ray muon spectrum at sea level. *Phys.Rev.D*, 58:092005, Oct 1998.

[72] National Science Foundation, 2007. see `http://www.deepscience.org/contents/underground_universe.shtml`.

[73] Bruno Rossi and Kenneth Greisen. Cosmic-ray theory. *Rev. Mod. Phys.*, 13:240–309, Oct 1941.

[74] Paul H. Barrett et al. Interpretation of cosmic-ray measurements far underground. *Rev. Mod. Phys.*, 24:133–178, Jul 1952.

[75] M. Ambrosio et al. Measurement of the residual energy of muons in the Gran Sasso underground laboratories. *Astropart.Phys.*, 19:313–328, 2003.

[76] I. L. Rozental'. Interaction of cosmic muons of high energy. *Physics-Uspekhi*, 11(1):49–65, 1968.

[77] MACRO Collaboration, M. Ambrosio, et al. The MACRO detector at Gran Sasso. *Nucl.Instrum.Meth.*, A486:663–707, July 2002.

[78] National Science Foundation, 2007. see `http://www.deepscience.org/contents/question_depth.shtml`.

[79] L. Pandola. Overview of the European Underground Facilities. *AIP Conf.Proc.*, 1338:12–19, 2011.

[80] G. Angloher et al. Limits on WIMP dark matter using sapphire cryogenic detectors. *Astropart. Phys.*, 18:43–55, 2002.

[81] G. Angloher et al. Commissioning run of the CRESST-II dark matter search. *Astroparticle Physics*, 31(4):270 – 276, 2009.

[82] F. Petricca. *Dark Matter Search with Cryogenic Phonon-Light Detectors*. PhD thesis, Ludwig-Maximilians-Universität München, 2005.

[83] R.F. Lang. *Search for Dark Matter with the CRESST Experiment*. PhD thesis, Technische Universität München, 2008.

[84] R. M^{c}Gowan. *Data Analysis and Results of the Upgraded CRESST Dark Matter Search*. PhD thesis, University of Oxford, 2008.

[85] E. Pantić. *Performance of Cryogenic Light Detectors in the CRESST-II Dark Matter Search*. PhD thesis, Universitätsbibliothek der TU München, 2008.

[86] P. Huff. *The Detector Parameters Determining the Sensitivity of the CRESST-II Experiment*. PhD thesis, Universitätsbibliothek der TU München, 2010.

[87] S. Pfister. *Suche nach Dunkler Materie mit dem CRESST-II-Experiment*. PhD thesis, Technische Universität München, 2010.

[88] J. Schmaler. *The CRESST Dark Matter Search – New Analysis Methods and Recent Results*. PhD thesis, Technische Universität München, 2010.

[89] W. Seidel, G. Forster, W. Christen, F. von Feilitzsch, H. Göbel, F. Pröbst, and R.L. Mösbauer. Phase transition thermometers with high temperature resolution for calorimetric particle detectors employing dielectric absorbers. *Physics Letters B*, 236(4):483 – 487, 1990.

[90] G. Angloher et al. Limits on WIMP dark matter using scintillating CaWO-4 cryogenic detectors with active background suppression. *Astropart. Phys.*, 23:325–339, 2005.

[91] C. Cozzini et al. Detection of the natural α decay of tungsten. *Phys. Rev. C*, 70:064606, Dec 2004.

[92] Pröbst, F. and others. Model for cryogenic particle detectors with superconducting phase transition thermometers. *Journal of Low Temperature Physics*, 100:69–104, 1995. 10.1007/BF00753837.

[93] Sabine Roth. Sputtered Tungsten Thin Films and Composite Detectors for the Application in the Dark Matter Experiments CRESST and EURECA. Diplomarbeit, Technische Universität München, 2007.

[94] S. A. Henry. *The 66-channel readout for the CRESST dark matter search*. PhD thesis, University of Oxford, 2003.

[95] P. Meunier et al. Discrimination between nuclear recoils and electron recoils by simultaneous detection of phonons and scintillation light. *Appl. Phys. Lett.*, 75(9):1335–1337, 1999.

[96] Saint-Gobain Crystals. BC-408 data sheet, 2008. available online at `http://www.crystals.saint-gobain.com/Plastic_Scintillators.aspx`; (2014).

[97] Electron Tubes, 2010. available online at `http://my.et-enterprises.com/pdf/9900B.pdf` (pdf); (2013).

[98] Y. Kotulski, T. Schön, and P. Huber. FdF collaboration, 2012.

[99] Daniele Nicolodi. Calibration system for the muon veto scintillators employed in the CRESST-II dark matter search experiment. Master's thesis, Universität Tübingen, 2006.

[100] R.D. Evans. *The atomic nucleus*. International series in pure and applied physics. McGraw-Hill, 1955.

[101] T. Enqvist et al. Measurements of muon flux in the Pyhäsalmi underground laboratory. *Nucl.Instrum.Meth.*, A554(1-3):286 – 290, 2005.

[102] M. Kimmerle. *Data analysis in the direct dark matter search experiment CRESST and calculation of the corresponding limit on the cross section of dark matter.* PhD thesis, Universität Tübingen, 2010.

[103] Franz Pröbst and Andreas Zöller, 2012. priv. communication.

[104] Ch. Berger et al. Experimental study of muon bundles observed in the fréjus detector. *Phys. Rev. D*, 40:2163–2171, Oct 1989.

[105] W.R. Leo. *Techniques for Nuclear and Particle Physics Experiments: A How-To Approach.* Springer-Verlag GmbH, 1994.

[106] G.F. Knoll. *Radiation detection and measurement.* Wiley, 2000.

[107] G. Bellini et al. Cosmic-muon flux and annual modulation in Borexino at 3800 m water-equivalent depth. *JCAP*, 1205:015, 2012.

[108] S.P. Ahlen et al. Muon astronomy with the MACRO detector. *Astrophys.J.*, 412:301–311, 1993.

[109] Luciano Pandola and Markus Knapp, 2009. priv. communication.

[110] Rene Brun, Anna Kreshuk, Eddy Offermann, and Fons Rademakers. TMath class, 2011. available online at `http://root.cern.ch/root/html/TMath.html#TMath:Landau`.

[111] Rene Brun and Fons Rademakers. ROOT – An object oriented data analysis framework. *Nucl.Instrum.Meth.*, A389(1-2):81–86, 1997.

[112] Franz Pröbst, 2011. priv. communication.

[113] Hans Kraus, 2011. internal note.

[114] Hans Kraus, 2011. priv. communication.

[115] K. Freund. PhD thesis, Universität Tübingen, 2014. in preparation.

[116] CNGS collaboration, 2014. priv. communication.

Acknowledgments

Naturally, a thesis within a collaboration is not solely the work of only one person, but based on previous work done by many others. Therefore, a few words of acknowledgment are in order. I'd like to thank

Prof. Josef Jochum for the opportunity to work in a very interesting field of physics and his enthusiasm for physics.

Prof. Peter Grabmayr for reading yet another thesis about a muon veto.

Prof. Hans Kraus, Barnaby, Richard and Andy for the OxRop development, fixing bugs and answering questions about it.
Dr. Franz Pröbst for always being available and always having an answer to any problem, even late at night.

All CRESST colleagues, which are not named here: although sometimes lacking manpower, we still have one of the world leading experiments and certainly one of the most interesting ones.

Arthur, Marcel and Roland for being a huge help with computer problems.

The PIT personnel, especially Günter Lang, Gaby and Sonja, as well as Frau Walz and Frau Eiskant, who help wherever they can.

All the colleagues - to name a few in random order: Fede, Johannes, Ludwig, Duncan, Diana, Hesti, Stephan, Michael, Markus, Markus, Lee, Daniel, Claudia, Katharina, Georg, Gerhard, Florian, Kai, Eduard, Igor, Dennis, Raphael, Christopher, Christof, Christian, Alex, Tobias, Anka, Martin, Büsra and all others I forgot here (sorry!) – it was great and interesting to have such widely varying topics not just during lunch and coffee discussions.

Whoever discovered the use of coffee and tea: thank you!

Michael Huber for some encouraging words.

Alex and Jörg for great times and battles on the court.

My friends, of course. Such friendships are truly precious.

Elvira, ti voglio dire che sei una persona magnifica. Grazie!

Meiner Familie, insbesondere meinen Eltern möchte ich ein herzliches Vergelt's Gott sagen.